



THE HONG KONG
POLYTECHNIC UNIVERSITY

香港理工大學

Pao Yue-kong Library

包玉剛圖書館

Copyright Undertaking

This thesis is protected by copyright, with all rights reserved.

By reading and using the thesis, the reader understands and agrees to the following terms:

1. The reader will abide by the rules and legal ordinances governing copyright regarding the use of the thesis.
2. The reader will use the thesis for the purpose of research or private study only and not for distribution or further reproduction or any other purpose.
3. The reader agrees to indemnify and hold the University harmless from and against any loss, damage, cost, liability or expenses arising from copyright infringement or unauthorized usage.

IMPORTANT

If you have reasons to believe that any materials in this thesis are deemed not suitable to be distributed in this form, or a copyright owner having difficulty with the material being included in our database, please contact lbsys@polyu.edu.hk providing details. The Library will look into your claim and consider taking remedial action upon receipt of the written requests.

AB INITIO CHEMICAL KINETICS AND
FLICKERING FLAME DYNAMICS OF
N-ALKANE FUEL COMBUSTION

CHI YICHENG

PhD

The Hong Kong Polytechnic University

2022

The Hong Kong Polytechnic University
Department of Mechanical Engineering

Ab Initio Chemical Kinetics and Flickering Flame Dynamics
of n-Alkane Fuel Combustion

Chi Yicheng

A thesis submitted in partial fulfillment of the requirements for
the degree of Doctor of Philosophy
May 2022

CERTIFICATE OF ORIGINALITY

I hereby declare that this thesis is my own work and that, to the best of my knowledge and belief, it reproduces no material previously published or written, nor material that has been accepted for the award of any other degree or diploma, except where due acknowledgment has been made in the text.

Signature: _____

Name of Student: Chi Yicheng

Abstract

The thesis consists of two parts. In Part 1, the ab initio chemical thermodynamics and chemical kinetics of typical combustion reactions of large straight-chain alkanes were investigated computationally. In Part 2, the dynamical behaviors of coupled flickering buoyant diffusion flames of alkane fuels were investigated experimentally. Four main studies and achievements are summarized as follows.

1. Accurate thermochemical data are of great importance in developing quantitatively predictive reaction mechanisms for transportation fuels, which are primarily composed of large hydrocarbon molecules, especially of long-chain alkanes containing more than 10 carbon atoms. The thesis presents an ONIOM[QCISD(T)/CBS:DFT]-based theoretical thermochemistry study on the hydrogen abstraction reactions of straight-chain alkanes, $n\text{-C}_n\text{H}_{2n+2} + \text{R}$ ($n = 1\text{-}16$, $\text{R} = \text{H}, \text{OH}, \text{HO}_2$). These reactions ($n \geq 10$) are computationally intractable for the prevalent high-level ab initio methods but are readily dealt with by the ONIOM-based method. The calculated results are in very good agreement with those obtained by using the widely accepted high-level QCISD(T)/CBS method, and their discrepancies are generally less than 0.10 kcal/mol. The present results demonstrate that the ONIOM-based method provides an accurate and efficient approach for the computational thermochemistry of large straight-chain hydrocarbon molecules in transportation fuels.
2. Besides the single-point energy, the partition function is another crucial factor in the calculation of thermochemistry and chemical kinetics of large straight-chain alkanes.

In the present thesis, we aimed to propose a systematic method to assess and explain the performance of variants of the MS-T (the multi-structural approximation with torsional anharmonicity) method which have widely used for large molecules. First, we proposed the simplest variant MS-2NN (two nearest neighborhood torsions are coupled) and systematically validated it for large alkanes $n\text{-C}_n\text{H}_{2n+2}$ ($n=6-10$) and their transition states of hydrogen abstraction reactions. Second, we proposed a metric-based method to explain the underlying reason for the good performance of MS-2NN — it includes the torsional conformers that have dominant contributions to the partition function calculations. These conformers are closer to the lowest-energy conformer in the space of dihedral and energy metrics. Third, the same observation and explanation apply to the other two variants, MS-2DT (any two torsions are coupled) and MS-3DT (any three torsional are coupled), which contain increasingly more torsional conformers than MS-2NN but are subsets of the complete set of torsional conformers considered by the MS-T method. Overall, the present method provides a mathematically rigorous and computationally effective diagnosis tool to assess various MS-T methods dealing with the torsional anharmonicity of large molecules in partition function calculation.

3. Torsional modes within a complex molecule containing various groups are often strongly coupled so that the harmonic approximation and one-dimensional torsional treatment are inaccurate to evaluate their partition functions. Although the MS-T method has been proposed to deal with the torsional anharmonicity, it approximates the exact “almost periodic” potential energy as a summation of local periodic functions

with symmetric barrier positions and heights. In the present thesis, we illustrated that the approximation is inaccurate when the torsional modes present non-uniformly distributed local minima. Therefore, we proposed an improved method (MS-ASB) to reconstruct the approximate potential to replace the periodic potential by using the information of the local minima and their Voronoi tessellation.

4. Regardless of the noteworthy progress in experimental progress in discovering dynamical behaviors of coupled multiple flickering diffusion flames, there are two major deficiencies in the existing experimental studies to be solved and the understanding of the multiple coupled flickering diffusion flames is still in the infant stage. Consequently, we established a well-controlled gaseous n -alkane diffusion flame experiment which well remedies the deficiencies of prevalent candle-flame experiments, and we developed a Wasserstein-space-based methodology for dynamical mode recognition, which is validated in the present triple-flame systems but can be readily generalized to the dynamical systems consisting of an arbitrary finite number of flames. By use of the present experiment and methodology, seven distinct stable dynamical modes were recognized, such as the in-phase mode, the flickering death mode, the partial flickering death mode, the partial in-phase mode, the rotation mode, the partial decoupled mode, and the decoupled mode. These modes unify the literature results for triple flickering flame system in the straight-line and equal-lateral triangle arrangements. Compared with the mode recognitions in physical space and phase space, the Wasserstein-space-based methodology avoids personal subjectivity and is more

applicable in high-dimensional systems, as it is based on the concept of distance between distribution functions of phase points. Consequently, the identification or discrimination of two dynamical modes can be quantified as the small or large Wasserstein distance, respectively.

Publications Arising from the Thesis

Journal Publications

1. **Y. Chi**, Q. Meng, L. Zhang and P. Zhang*, An ONIOM-based Thermochemistry study of Hydrogen Abstraction Reaction of $n\text{-C}_n\text{H}_{2n+2} + \text{R}$ ($n=1-16$, $\text{R}=\text{H}, \text{OH}, \text{HO}_2$), *Fuel* (under review) <http://dx.doi.org/10.2139/ssrn.4161704>.
2. **Y. Chi**, Q. Meng, C. He, and P. Zhang*, A Metric-based Multi-Structural Method for Calculating Conformational-Rovibrational Partition Functions of Large Molecules, *The Journal of Physical Chemistry A* (under review).
3. C. He, **Y. Chi**, and P. Zhang*, Approximate Reconstruction of Torsional Potential Energy Surface Based on Voronoi Tessellation, *Proceedings of the Combustion Institute*, 2021, 38(1), 757-766.
4. **Y. Chi**, T. Yang, and P. Zhang*, Dynamical Mode Recognition of Triple Flickering Buoyant Diffusion Flames in Wasserstein Space, *Combustion and Flame* (under review) arXiv:2201.01085.
5. **Y. Chi** and P. Zhang*, High-level Theoretical Thermochemistry Study Review on Large Gaseous Fuel Molecules, *Physics of Gases*, 2019, 4(5), 32-42.

Conference Publications

1. **Y. Chi**, T. Yang and P. Zhang*, Wasserstein-space-based Methodology for Dynamical Mode Recognition of Triple Flickering Buoyant Diffusion Flames, *China National Symposium on Combustion*, Shanghai, China, 22-25 September 2022.

2. C. He, **Y. Chi**, and P. Zhang*, Approximate Reconstruction of Torsional Potential Energy Surface based on Voronoi Tessellation, *38th International Symposium on Combustion*, Adelaide, Australia, 24-29 January 2021.
3. **Y. Chi**, Q. Meng, L. Zhang, and P Zhang*, High-level Thermochemistry Study of Hydrogen Abstraction Reactions of Large Straight-Chain Alkanes Molecules by Hydrogen, Hydroxyl and Hydroperoxyl Radicals, *12th Asia-Pacific Conference on Combustion*, Fukuoka, Japan, 1-5 July 2019.
4. **Y. Chi**, Q. Meng, L. Zhang, and P Zhang*, Towards High-level Theoretical Studies of Aviation Kerosene Molecules: An ONIOM[QCISD(T)/CBS:DFT] Study on Hydrogen Abstraction Reaction of Large Straight-chain Alkanes Molecules C_nH_{2n+2} + (H,OH,HO₂) Radicals, *The 8th East Asia Mechanical and Aerospace Engineering Workshop*, Hong Kong, China, 1-3 December 2018.
5. **Y. Chi**, Q. Meng, L. Zhang, and P Zhang*, High-level Theoretical Thermochemistry Study on Hydrogen Abstraction Reactions of Large Straight-chain Alkanes Molecules C_nH_{2n+2} + (H,OH,HO₂) Radicals, *China National Symposium on Combustion*, Harbin, China, 13-16 September 2018.
6. **Y. Chi**, Y. Zhu, Q. Meng, L. Zhang, and P. Zhang*, An ONIOM-method-based High-level Theoretical Study on Hydrogen Abstraction Reactions of Large Straight-chain Alkanes Molecules by Hydrogen Radical, *China National Symposium on Combustion*, Nanjing, China, 13-15 October 2017. (Best poster award)

Other Publications

1. T. Yang, **Y. Chi**, and P. Zhang*, Vortex Interaction in Triple Flickering Buoyant Diffusion Flames, *Proceedings of the Combustion Institute*, accepted, 2022.
2. L. Yang, Z. Li, T. Yang, **Y. Chi**, and P. Zhang*, An Experimental Study on Droplet Splash and Receding Breakup on a Smooth Surface at Atmospheric Pressure, *Langmuir*, 2021, 37, 10838-10848.
3. Q. Meng, L. Zhang, Q. Chen, **Y. Chi**, and P. Zhang*, Influence of Torsional Anharmonicity on the Reactions of Methyl Butanoate with Hydroperoxyl Radical, *The Journal of Physical Chemistry A*, 2020, 124(42), 8643-8652.
4. Q. Meng, **Y. Chi**, L. Zhang, P. Zhang*, and L. Sheng, Towards high-level theoretical studies of large biodiesel molecules: An ONIOM/RRKM/Master-equation approach to the isomerization and dissociation kinetics of methyl decanoate radicals, *Physical Chemistry Chemical Physics*, 2019, 21, 5232-5242.
5. L. Zhang, Q. Meng, **Y. Chi**, and P. Zhang*, Towards High-level Theoretical Studies of Large Biodiesel Molecules: An ONIOM [QCISD(T)/CBS:DFT] Study of the Reactions between Unsaturated Methyl Esters ($C_nH_{2n-1}COOCH_3$) and Hydrogen Radical, *The Journal of Physical Chemistry A*, 2018, 122(21), 4882-4893.
6. Q. Meng, **Y. Chi**, L. Zhang, P. Zhang*, and L. Sheng, A Theoretical Study on the Isomerization and Dissociation Kinetics of Methyl Decanoate Radicals, *12th Asia-Pacific Conference on Combustion*, Fukuoka, Japan, 1-5 July 2019.

Acknowledgements

First of all, I would like to sincerely express my gratitude to my supervisor, Prof. Peng Zhang, for his patient supervision, and constant encouragement during my entire Ph.D. study period. The reason why I can complete my Ph.D. study is that Prof. Zhang's insightful opinions, rigorous attitude, and strict requirements for the study help me reach the essence of the problems and lead me on the right track of research. I cherish the precious wealth that I obtained from my supervisor, and his enthusiastic research spirit will profoundly influence me in my future work and life.

Secondly, I would also like to thank my co-supervisor, Prof. Chih-Yung Wen for his unselfish help and valuable suggestions regarding my research. In the meantime, I would also like to thank the department staffs who create a good working environment for my Ph.D. study.

Besides, my special thanks should also be given to Prof. Lidong Zhang, Dr. Qinghui Meng, and Dr. Chengming He for their great help in the results analysis of quantum chemistry and chemical kinetics. I would also like to thank Mr. Tao Yang for our cooperation work on dynamical mode recognition of multiple flickering diffusion flames, and all other group members, Prof. Zhenyu Zhang, Prof. Xi Xia, Dr. Xuren Zhu, Dr. Dawei Zhang, Dr. Dehai Yu, and Dr. Kun Wu, who supported and encouraged me during my Ph.D. study period.

Finally, I am forever grateful to my wife Nian Wang for her unreserved support. I would like to sincerely thank my family for their love. I wish them all the best!

Table of Contents

Abstract.....	I
Publications Arising from the Thesis.....	V
Acknowledgements.....	VIII
List of Figures.....	XIV
List of Tables.....	XXI
Part 1 High-level Theoretical Chemical Thermodynamics of Large Straight-Chain Alkanes	1
Chapter 1. Background and Motivation.....	2
1.1 Large Straight-Chain Alkanes	2
1.2 Research Objectives	4
Chapter 2 Theoretical Methods.....	8
2.1 Quantum Chemistry Calculation.....	8
2.1.1 Ab Initio Method.....	8
2.1.2 Density Functional Theory	9
2.1.3 Basis Sets Selection	10
2.1.4 Zero-point Energy Correction.....	11
Chapter 3 An ONIOM-based Thermochemistry Study of Hydrogen Abstraction Reactions of $n\text{-C}_n\text{H}_{2n+2} + \text{R}$ ($n = 1\text{-}16$, $\text{R} = \text{H}, \text{OH}, \text{HO}_2$).....	13
3.1 Introduction.....	13
3.2 Computational methods	16

3.2.1 Potential Energy Surfaces	16
3.2.2 QCISD(T)/CBS Single-Point Energies.....	17
2.2.3 ONIOM[QCISD(T)/CBS] Single-Point Energies	18
3.3 Results and Discussion.....	21
3.3.1 Hydrogen Abstraction Reaction of $n\text{-C}_n\text{H}_{2n+2} + \text{H}$ ($n = 1\text{-}16$)	21
3.3.2 Hydrogen Abstraction Reaction of $n\text{-C}_n\text{H}_{2n+2} + \text{OH}$ ($n = 1\text{-}16$)	24
3.3.3 Hydrogen Abstraction Reaction of $n\text{-C}_n\text{H}_{2n+2} + \text{HO}_2$ ($n = 1\text{-}16$)	28
3.3.4 Comparison of Computational Expense between QCISD(T)/CBS and ONIOM methods	32
3.4 Comparison with Literature Data.....	34
3.4.1 Comparison with Data from Kinetic Modelling.....	34
3.4.2 Comparison with Data from Ab Initio Calculations.....	36
3.4.3 Comparison with Saturated and Unsaturated Methyl Ester.....	39
3.5 Concluding Remarks	42
3.6 Appendix	44
Chapter 4 A Metric-based Multi-Structural Method for Calculating Conformational- Rovibrational Partition Functions of Large Molecules.....	53
4.1 Introduction	53
4.2 Theoretical Methods.....	58
4.2.1 Multi-structural (MS) Method	58
4.2.2 Metric-based Method.....	60

4.2.3 Nearest Neighborhood Method.....	63
4.2.4 Electronic Structure Method.....	65
4.3 Results and Discussion.....	65
4.3.1 Structures Generation by MS-2NN and MS-T.....	65
4.3.2 Qualitative Verification of MS-2NN Method based on Voronoi Tessellation	67
4.3.3 Partition Function and Standard State Entropy	69
4.3.4 Distribution of Energy and Dihedral Metrics	71
4.3.5 Comparison of MS-2DT and MS-3DT with MS-T	75
4.4 Concluding Remarks.....	77
4.5 Appendix	80
Chapter 5 Approximation of Torsional Potential Energy Surface Reconstructed by Voronoi Tessellation.....	91
5.1 Introduction	91
5.2 Theoretical methods	92
5.3 Results and Discussion.....	94
5.3.1 Uncertainty Analysis of MS-AS Method.....	94
5.3.2 Improved Reconstruction of Torsional PES	96
5.3.3 Validation Testing Cases by MS-ASB	101
5.4 Concluding Remarks.....	104
Part 2 Experimental Study of Coupled Flickering Buoyant Diffusion Flames.....	105

Chapter 6 Background and Motivation.....	106
6.1 Flickering Diffusion Flames.....	106
6.2 Coupled Dual Flickering Diffusion Flames	111
6.3 Coupled Multiple Flickering Diffusion Flames	113
6.4 Research Objectives	114
Chapter 7 Dynamical Mode Recognition of Coupled Multiple Flickering Buoyant Diffusion Flames.....	116
7.1 Introduction	116
7.2 Experimental Methodology.....	117
7.3 Dynamical Mode Recognition for Stable Modes in Physical Space.....	119
7.3.1 Dynamical Modes of Dual Flickering Buoyant Diffusion Flames	119
7.3.2 Dynamical Modes of Triple Flickering Buoyant Diffusion Flames ...	122
7.4 Dynamical Mode Recognition for Stable Modes in Phase Space.....	125
7.4.1 Characteristic Quantities of Flickering Flames	126
7.4.2 Phase Portraits for Dynamical Modes of Dual Flickering Flames	129
7.4.3 Phase Portraits for Dynamical Modes of Triple Flickering Flames ...	131
7.5 Dynamical Mode Recognition based on Wasserstein Distance	134
7.5.1 Motivations for Wasserstein-distance-based Mode Recognition.....	134
7.5.2 Calculation of Wasserstein Distance.....	137
7.5.3 Dynamical Mode Recognition in Wasserstein Space	140
7.7 Concluding Remarks	142

Chapter 8 Future Work.....	145
Reference	146

List of Figures

- Figure 3.1 Illustration of the ONIOM[QCISD(T)/CBS:DFT]/CAP(2,2) method for the hydrogen abstraction reaction by H, OH, and HO₂ radicals, C₁₆H₃₄ + (H, OH, and HO₂) → CH₃(CH₂)₄CH(CH₂)₅CH₃ + (H₂, H₂O, and H₂O₂). The indices from 1-16 denote the CH₃ (or CH₂) groups. CAP (2,2) (in the circle) represents the chemically active portion consisting of the No.6 and No.7 CH₂ groups on the one side of the No. 8 CH₂ group under hydrogen attack, and No. 9 and No. 10 CH₂ groups on the other side of No. 8 CH₂ group in reactant and products. For the transition state, H, OH, and HO₂ radicals are also needed to be added to the CAP. 18
- Figure 3.2 The difference between the calculated energy barriers (EB) and heat of reactions (HR), for the reactions of *n*-C_nH_{2n+2} + H (n=1-9); The notation *m* (=1-5) denotes the group under hydrogen attack.....22
- Figure 3.3 (a) The predicted EBs and (b) the predicted HRs for the hydrogen abstraction reactions of *n*-C_nH_{2n+2} + H (n=10-16).23
- Figure 3.4 The difference between the calculated energy barriers (EB) and heat of reactions (HR), for the reactions of *n*-C_nH_{2n+2} + OH (n=1-8); The notation *m* (=1-4) denotes the group under hydroxyl (OH) attack.26
- Figure 3.5 (a) The predicted EBs and (b) the predicted HRs for the hydrogen abstraction reactions of *n*-C_nH_{2n+2} + OH (n=9-16).27
- Figure 3.6 The difference between the calculated energy barriers (EB) and heat of reactions (HR), for the reactions of *n*-C_nH_{2n+2} + HO₂ (n=1-7); The notation *m* (=1-4)

denotes the group under hydroperoxyl (HO ₂) attack.	30
Figure 3.7 (a) The predicted EBs and (b) the predicted HRs for the hydrogen abstraction reactions of $n\text{-C}_n\text{H}_{2n+2} + \text{HO}_2$ ($n=8\text{-}16$).	31
Figure 3.8 The EBs for the hydrogen abstraction reactions of $\text{C}_{15}\text{H}_{31}\text{COOCH}_3 + \text{H}$ and $n\text{-C}_{16}\text{H}_{34} + \text{H}$	39
Figure 3.9 The EBs for the hydrogen abstraction reactions of $\text{C}_{17}\text{H}_{33}\text{COOCH}_3 + \text{H}$ and $n\text{-C}_{18}\text{H}_{38} + \text{H}$	41
Figure 4.1 Schematic of the simplest variant MS-2NN (two nearest neighborhood torsions are coupled) method to generate initial-guess structures.	64
Figure 4.2 (a) weighted Voronoi tessellation and (b) reconstructed potential energy surface based on the method [121].	68
Figure 4.3 The partition function ratio (PFR), $Q^{\text{MS-T}}/Q^{\text{MS-2NN}}$, using MS-T and MS-2NN methods for (a) n -hexane and n -hexane-TS1 to TS3, and (b) n -heptane and n -heptane-TS1 to TS4.	70
Figure 4.4 Distributions of distinguishable structures of n -heptane in the space of \bar{d}_D and \bar{d}_E using MS-T and MS-2NN methods for different coordinates (a) $(\bar{d}_E(s_j, s_k), \bar{d}_D(s_j, s_k))$ and (b) $(\bar{d}_E(s_1, s_j), \bar{d}_D(s_1, s_j))$	72
Figure 4.5 Distribution of distinguishable structures (with respect to the lowest energy conformer) in the space of \bar{d}_D and \bar{d}_E using MS-T and MS-2NN methods for n -heptane-TS1 to TS4.	73
Figure 4.6 Distribution of distinguishable structures (with respect to the lowest	

energy conformer) in the space of \bar{d}_D and \bar{d}_E using MS-T and MS-2NN methods for <i>n</i> -hexane and <i>n</i> -hexane-TS1 to TS3.	74
Figure 4.7 The partition function ratio (PFR) of $Q^{\text{MS-T}}/Q^{\text{MS-nDT}}$ using MS-T and MS-nDT methods for (a) <i>n</i> -heptane and (b) <i>n</i> -heptane-TS1.....	75
Figure 4.8 Distribution of distinguishable structures (with respect to the lowest energy conformer) in the space of \bar{d}_D and \bar{d}_E using MS-T and MS-nDT methods for <i>n</i> -heptane and <i>n</i> -heptane-TS1.....	76
Figure 5.1 Schematic (a) 2D and (b) 3D Voronoi tessellation generated from the presently calculated 78 conformational structures of transition state in the hydrogen abstraction of MB (methyl butanoate) by HO ₂ radical.	92
Figure 5.2 Potentials of a periodic function V_1 , an almost periodic function V_2 (corresponding to H ₂ O ₂), and piecewise periodic functions V_3 that constructed in the MS-AS method.....	94
Figure 5.3 Closeup of Voronoi subspace and constructed MS-AS subspace in Figure 5.1.....	95
Figure 5.4 A closeup of upper left corner of Figure 5.1(a) which shows the improvements of the MS-AS method with corrected (a) barrier heights based on original Voronoi diagram and (b) barrier positions based on multiplicatively weighted Voronoi diagram.	97
Figure 5.5 Comparison of (a) the potential curve and (b) partition function ratio (PFR) of the 1D torsional mode of H ₂ O ₂ [38].	100

Figure 5.6 Test of the 2D torsional mode of 1-pentyl radical [38]. (a) comparison of partition function (PFR). Schematic of the (b) original Voronoi diagram by MS-AS method and (c) weighted Voronoi diagram by MS-ASB method. 102

Figure 5.7 Test of a 3D torsional mode of 1-butanol radical. (a) comparison of partition function ratio and (b) schematic of weighted Voronoi diagram. 103

Figure 6.1 (a) Experimental photographs of flickering of diffusion flame, (b) the time series of the flame height [134], and (c) the progressive necking process of flickering diffusion flame [135]. 106

Figure 6.2 Experimental photographs of (a) wave structure of hydrogen jet diffusion flame [138] and (b) toroidal vortices of methane jet diffusion flame [139]. 107

Figure 6.3 The summary of flickering frequencies of diffusion flame as a function of burner diameter: (a) Hamins et al. [146] and (b) Cetegen and Ahmed [147]. .. 109

Figure 6.4 Experimental photographs of coupled dual candle flames: (a) in-phase (above) mode and anti-phase mode (below) by Kitahata et al. [149]; (b) in-phase mode by Forrester [150]; (c) from left to right are in-phase mode, death mode, anti-phase mode, and desynchronization mode by Manoj et al. [151]; and (d) from left to right are in-phase mode, death mode, anti-phase mode, and desynchronization mode by Dange et al. [152]. 110

Figure 6.5 Experimental photographs and time series of each flame brightness [158] of four distinct dynamical modes: (a) the in-phase mode, (b) the partial in-phase mode, (c) the rotation mode, and (d) the death mode. 112

Figure 6.6 Experimental photograph [150] of (a) four coupled candle flames in an initial-arch-bow-initial “worship” oscillation mode and (b) five coupled candle flames in a ring-shape arrangement showing an outer ring of four candle flames enslave a central flame, collectively enhancing (left) and suppressing (right) the height of the central flame..... 113

Figure 7.1 Schematic of the established experimental apparatus consisting of burners, fuel flow controls, and visualization systems. 119

Figure 7.2 Experimental photographs of flickering buoyant diffusion flames for (a) single flame system and dual flame system in (b) the decoupled mode, (c) the weakly coupled mode, (d) the anti-phase mode, (e) the flickering death mode, (f) the in-phase mode, and (g) the merged case, at the distance of 8.0, 6.0, 4.0, 3.0, 2.0, and 1.5 cm, respectively. All the flames have the fuel flow rate $Q = 0.55$ slpm..... 120

Figure 7.3 Single flickering buoyant diffusion flames. The flow rates (a-e) are fixed at $Q = 0.45, 0.50, 0.55, 0.60$ and 0.65 slpm, respectively..... 121

Figure 7.4 Merged triple flickering buoyant diffusion flames at $Q = 0.45$ slpm. 121

Figure 7.5 Experimental photographs of seven distinct stable dynamical modes of triple flickering buoyant diffusion flames. I-VII are in-phase, flickering death, partial flickering death, partial in-phase, rotation, partial decoupled, decoupled respectively. See details of flame setup in Table 7.1..... 123

Figure 7.6 The schematic of establishing phase portraits in a three-dimensional phase

space. Each grayscale image is processed and extracted for four time-varying quantities (height, width, size, and brightness) of each flickering flame. The flame brightness is taken an example here. The 22s duration of triple flickering flames yields 11000 phase points in phase space. 126

Figure 7.7 Time-varying graphs of scalar quantities (height, width, size, and brightness) for each flickering flame. The time corresponds to 10-12s in Figure 7.6 The height and width are normalized by the nozzle diameter, the size by the nozzle area, and the brightness by the product of 255 and the nozzle area. 128

Figure 7.8 Two-dimensional phase portraits for dual flickering buoyant diffusion flames, corresponding to the cases in Figure 7.2(b)-(f). There are five synchronized flickering modes with the distance decreasing. All phase spaces, plotted by the flame brightness, have the same ranges of values in all dimensions. 130

Figure 7.9 Three-dimensional phase portraits, their two-dimensional projections, and flame setup parameters (unit of B and L : cm; unit of Q : slpm) for seven stable dynamical modes, corresponding to the cases of Mode I-Mode VII in Figure 7.5 respectively. All phase spaces, plotted by the flame brightness, have the same ranges of coordinates in all dimensions. 132

Figure 7.10 Three-dimensional phase portraits, their two-dimensional projections, and the flame setup parameters (unit of B and L : cm; unit of Q : slpm) for untypical dynamical modes. All phase spaces, plotted by the flame brightness, have the same ranges of coordinates in all dimensions. 135

Figure 7.11 The time-varying topological structures of phase portraits. The 2D phase portraits for $\mathcal{B}_1 - \mathcal{B}_2$, $\mathcal{B}_1 - \mathcal{B}_3$ and $\mathcal{B}_2 - \mathcal{B}_3$ are unstable during the 22s and not recognized readily. All phase spaces, plotted by the flame brightness, have the same ranges of coordinates in all dimensions. 136

Figure 7.12 Phase portraits of in-phase, in-phase and anti-phase modes of two adjacent flames (a)-(c), the corresponding phase point distributions in 10×10 cells (d)-(f) and the corresponding discrete probability distributions of the number of phase points in each cell (g)-(i). The Wasserstein distance between the two probability distributions of (a) and (b), denoted by W^{ab} , is 11. W^{bc} of (b) and (c) is 48, and W^{ca} of (c) and (a) is 42. 138

Figure 7.13 Three-dimensional phase portraits, three two-dimensional projections, flame setup parameters (unit of B and L : cm; unit of Q : slpm), and Wasserstein distances of seven experimental cases, C1–C7, which respectively correspond to Mode I – Mode VII but are different from those cases in Figure 7.9. All phase spaces, plotted by the flame brightness, have the same ranges of values in all dimensions. The Wasserstein distance (i.e., the radial distance) is the root mean square of W^{12} , W^{13} and W^{23} 140

List of Tables

Table 3.1 The comparison of calculated results (EB and HR) for the hydrogen abstraction reactions of $n\text{-C}_n\text{H}_{2n+2} + \text{H}$ ($n = 1\text{-}5$) using the [QCISD(T)/CBS] ₁ and [QCISD(T)/CBS] ₂ (unit: kcal/mol).....	21
Table 3.2 The comparison of calculated results (EB and HR) for the hydrogen abstraction reactions of $n\text{-C}_n\text{H}_{2n+2} + \text{OH}$ ($n = 1\text{-}4$) using the [QCISD(T)/CBS] ₁ and [QCISD(T)/CBS] ₂ (unit: kcal/mol).....	25
Table 3.3 The comparison of calculated results (EB and HR) for the hydrogen abstraction reactions of $n\text{-C}_n\text{H}_{2n+2} + \text{HO}_2$ ($n = 1\text{-}3$) using the [QCISD(T)/CBS] ₁ and [QCISD(T)/CBS] ₂ (unit: kcal/mol).....	29
Table 3.4 The comparison of computation times with the [QCISD(T)/CBS] ₂ and ONIOM methods. (unit: minutes).....	33
Table 3.5 The comparison of EB from kinetic modelling and obtained by the ONIOM method for the hydrogen abstraction reactions of $n\text{-C}_n\text{H}_{2n+2} + \text{H}$, OH, and HO ₂ ($n = 3\text{-}16$) (unit: kcal/mol).	34
Table 3.6 The calculated EB for the hydrogen abstraction reactions of $n\text{-C}_n\text{H}_{2n+2} + \text{H}$ ($n = 1\text{-}4$ and 18) (unit: kcal/mol).....	36
Table 3.7 The calculated EB for the hydrogen abstraction reactions of $n\text{-C}_n\text{H}_{2n+2} + \text{OH}$ ($n = 5$) (unit: kcal/mol).....	37
Table 3.8 The calculated EB for the hydrogen abstraction reactions of $n\text{-C}_n\text{H}_{2n+2} + \text{HO}_2$ ($n = 5$) (unit: kcal/mol).....	38

Table 4.1 The number of distinguishable structures for reactants and transition states (excluding mirror-image structures).	65
Table 4.2 Structural information (in the ascending order of energy metric) for <i>n</i> -hexane using the MS-T and MS-2NN (in bold red) methods (units in kcal/mol for energy and degree for dihedral angles).....	67
Table 4.3 Standard state entropy (in cal/mol/K) of <i>n</i> -alkanes (from C ₆ to C ₁₀) at 298.15 – 2000 K calculated using the MS-T and MS-2NN methods and compared with the reference data [122].	71
Table 7.1 The flames setup parameters in an isosceles triangle for Mode I – Mode VII and stable cases C1 – C7 (unit of <i>B</i> and <i>L</i> : cm; unit of <i>Q</i> : slpm).	125
Table 7.2 The calculated triplets (W^{12}, W^{13}, W^{23}) and their root mean square (shown in parentheses) of 1-Wasserstein distance between Mode I – Mode VII and the stable cases C1-C7.	139

Part 1

**High-level Theoretical Chemical Thermodynamics of Large Straight-
Chain Alkanes**

Chapter 1. Background and Motivation

1.1 Large Straight-Chain Alkanes

The intensified problem of energy and environment spawned continuous studies on the development of engine combustion performance, such as vehicle engines and aircraft engines [1]. Whatever gasoline, diesel fuel, and jet fuel, these practical fuels have a significant effect on combustion processes. The aim of investigating chemical reaction mechanisms on combustion is to understand and analyze the combustion processes for enhancing combustion efficiency, controlling flame stability, and reducing emissions [2]. To satisfy the higher combustion requirements of engines, it is necessary to carry out comprehensive and systematic research on petroleum-based fuels, such as gasoline, diesel, and aviation kerosene, for making rational use of them.

However, it is quite difficult to study thermochemistry and chemical kinetics for gasoline [3, 4], diesel [5], and jet fuel [6, 7] on account of their complicated components. The fuels generally consist of hundreds of different hydrocarbon molecules, and the main components are alkanes (*n*-alkanes, *iso*-alkanes, branched alkanes, and cycloalkanes), alkenes (olefins), and aromatics by structural classes of hydrocarbon compounds from small molecules to large molecules, the carbon numbers of the components range from approximately C4-C10 for gasoline [3, 8], C10-C22 for diesel fuel [9], and C10-C14 for jet fuel [7], and straight-chain alkanes (*n*-alkanes) are primary components in these practical fuels [3, 5, 7, 10-12].

The common treatment is that using surrogate fuels which consist of several typical

components represent these practical fuels and many of them have been studied and validated. For gasoline fuels, Mehl et al. [13] developed linear and branched saturated hydrocarbons (*iso*-octane and *n*-heptane), olefins (1-hexene), and aromatics (toluene) as the gasoline surrogates for kinetic modelling. Jerzembeck et al. [14] and Sileghem et al. [15] showed that the laminar burning velocities of two-component (*n*-heptane and *iso*-octane) and three-component gasoline surrogate (*iso*-octane, *n*-heptane, and toluene) were in good agreement with those of the commercial gasoline, respectively.

For diesel fuels, Lemaire et al. [16] adopted two diesel surrogates (70% *n*-decane and 30% α -methyl-naphthalene; 80% *n*-decane and 20% α -methyl-naphthalene in moles) to make a comparison of soot formation in turbulent flames with commercial diesel. Mati et al. [17] adopted a five-component surrogate (36.1% *n*-hexadecane, 23.1% *n*-propylcyclohexane, 18.7% *n*-propylbenzene, 14.7% *iso*-octane, and 7.4% 1-methyl-naphthalene by weight) to represent a diesel fuel.

For jet fuels, Honnet et al. [18] developed the Aachen surrogate, which consists of 80% *n*-decane and 20% 1,2,4-trimethylbenzene by weight, to represent JP-8. Dagaut et al. [19] used a 1- to 3-component surrogate model fuels, which contains 100% *n*-decane, *n*-decane-*n*-propylbenzene (74%-26% by mole) *n*-decane-*n*-propylcyclohexane (74%-26% by mole), and *n*-decane-*n*-propylbenzene-*n*-propylcyclohexane (74%-15%-11% by mole), to represent Jet-A1. Strelkova et al. [20] adopted a Jet-A surrogate mixture of 72.7% *n*-decane, 9.1% *n*-hexane, and 18.2% benzene by weight. Mawid et al. [21] proposed the three multi-component surrogates for JP-8, mainly containing large

straight-chain alkanes (*n*-decane, *n*-dodecane, *n*-tetradecane, and *n*-hexadecane). Dahm et al. [22] also conducted an experimental and modelling study of the pyrolysis of *n*-dodecane, for it is an important component of some jet fuels. Numerous studies have shown that normally large hydrocarbon molecules containing more than 10 carbon atoms are the primary components in these surrogate fuels. It is very important to develop a high-level chemical reaction mechanism for large hydrocarbon molecules.

1.2 Research Objectives

Establishing detailed and comprehensive chemical reaction mechanisms of large hydrocarbon molecules, such as *n*-decane, *n*-dodecane, *n*-tetradecane, and *n*-hexadecane, normally need to specify thermochemical data for hundreds, even thousands, elementary reactions and reaction rate constants for hundreds of chemical species. For empirical and semi-empirical approaches, they cannot provide relatively accurate results and experimental and theoretical corrections are indispensable. Ab initio chemical kinetics has enjoyed notable advances in the past years and become a quantitative and reliable research approach [23]. However, it is noteworthy that doing calculations for the rate constants of each reaction is unpractical. Therefore, Ab initio chemical kinetics mainly aims at the key reactions. For example, unimolecular reactions of large fuel molecules, the reactions between large fuel molecules and small radicals (H, OH, CH₃), and the decomposition reactions of large fuel molecules under high temperature (> 1000 K); the reactions between large fuel molecules and small radicals (O₂ and HO₂) are also needed to consider under low temperature. High-level Ab Initio

chemical kinetics has been adopted to study small fuel molecules [24-30], but there are several main difficulties in the study of large fuel molecules.

First, using the high-level computational approach for quantum chemistry calculation of large fuel molecules, developing a computationally accurate and affordable approach for quantum chemistry calculation is necessary, for the majority of the studies mainly revolved around relatively small hydrocarbon molecules [25-30] due to computationally challenging for the prevalent high-level electronic structure theory-based methods for the large hydrocarbon molecules. For example, the coupled-cluster theory with single and double excitations and a quasi-perturbative treatment of connected triplet excitations [CCSD(T)], with an extrapolation to the complete basis set (CBS), yields the predictions of thermochemical results (energy barrier and heat of reaction) with uncertainties less than 1.1 kcal/mol [31]. The quadratic configuration interaction with singles, doubles, and perturbative inclusion of triples, and with an extrapolation to complete basis set [QCISD(T)/CBS] is usually accurate at around 1.0 kcal/mol [32] and can be accurately predicted to 0.6 kcal/mol with the inclusion of a bond additivity correction [33]. Although these methods can provide relatively accurate results, they are not applicable for a reaction system with more than 10 non-hydrogen atoms [34]. For solving this problem, we adopted and developed ONIOM[QCISD(T)/CBS:DFT] [35] method for the hydrogen abstraction reactions of straight-chain alkanes, $n\text{-C}_n\text{H}_{2n+2} + \text{R}$ ($n = 1-16$, $\text{R} = \text{H}, \text{OH}, \text{HO}_2$), and it will be detailed in Chapter 3.

Second, high-level computational approach for chemical kinetics calculation of large fuel molecules, especially for the partition function calculation of anharmonic hindered rotors, the calculation of rate constants needs partition functions of transition state and reactant, based on the transition state theory. Under the approximation of Hamiltonian with separability, the total partition function can be represented as the product of each molecule's (radical's) partition function of the internal degrees of freedom. The implicit physical assumption is that the coupling strength of each internal molecular degree of freedom is relatively weak, so it could not provide a significant contribution to the total Hamiltonian. However, there is a kind of torsional internal rotor in reactive molecules (reactants, and transition states). For example, the two methyl radicals rotate around the C-C bond between them in the ethane molecules. For the small molecular systems, there are fewer torsional degrees of freedom in the systems, so the coupling effect is not strong. In general, Pitzer and Gwinn [36] proposed a pioneering one-dimensional hindered rotor method, and it has been widely validated and used [34, 37]. There is a defect in the method for dealing with the torsional degrees of freedom which often have relatively strong coupling in large molecular systems, for in these systems it is not easy to identify the torsional degrees of freedom with a specific normal mode. To address the problem, Zheng et al. [38] proposed a new class of multi-structural methods. Although the methods have been fully verified, it also has a defect in large amounts of computation for dealing with large molecules [39, 40]. For solving this problem, we adopted and developed the multi-structural method and it will be

detailed in Chapters 4 and 5.

Based on the above discussion for the development of chemical kinetics of combustion reactions, it is clear that there also remains some thorny problems in the thermodynamics and kinetics of large straight-chain alkanes, although some advanced and available approaches for relatively small or medium-size systems. Therefore, the present research focus is on developing a computationally accurate and affordable approach for the computational thermochemistry and chemical kinetics of large straight-chain alkanes molecules in practical fuels.

Chapter 2 Theoretical Methods

2.1 Quantum Chemistry Calculation

Quantum chemistry, also known as molecular quantum mechanics, is an important branch of chemistry [41]. It is focused on the application of quantum mechanics to chemical systems. In short, the wave functions can be obtained by solving the time-independent Schrödinger equation, and then the information on electronic structures and energies can be obtained. It is difficult to exactly solve the Schrödinger equation of molecular systems, so the approximate method is used to simplify the process in the practical calculation. Therefore, the methods of quantum chemistry calculation generally consist of the ab initio method, semi-empirical method, and density functional theory method.

2.1.1 Ab Initio Method

Ab initio method is to solve the time-independent Schrödinger equation directly based on the principles of quantum mechanics. The general form of the equation is given by:

$$\hat{H}\Psi = E\Psi \quad (2.1)$$

where \hat{H} is Hamiltonian operator, and Ψ and E are the wave function and the electronic energy of the system, respectively. In general, if the specific form of \hat{H} is determined, the wave function and the electronic energy of the system can be obtained by the solution of the Eq. (2.1).

In practice, however, it is hard to exactly solve the Schrödinger equation. Generally,

three approximations are introduced to ab initio method to reduce the computational difficulty: (1) the non-relativistic approximation (ignoring the relativistic effect) [42], (2) Born-Oppenheimer approximation [43], and (3) orbital approximation [44]. The Hartree-Fock (HF) method which is a method of approximation for the determination of the wave function and the energy of a quantum many-body system was developed through these approximations. After that, the post-Hartree-Fock methods were proposed to improve on the HF method by adding the electron correlation.

The post-HF methods mainly consist of configuration interaction (CI), coupled cluster (CC), Møller–Plesset perturbation theory (MP2, MP3, etc.), and quadratic configuration interaction (QCI), etc. QCISD(T) method was applied in the present study.

2.1.2 Density Functional Theory

Density functional theory (DFT) [45] is a computational quantum mechanical modeling method used in physics, chemistry, and materials science to investigate the electronic structure (principally the ground state) of many-body systems, in particular atoms, molecules, and the condensed phases. Not only is it much cheaper than other self-consistent field theories [46], such as the Hartree-Fock theory, but it also is sufficiently accurate for predicting a great many molecular properties, such as geometric structures and vibrational frequencies, for DFT treats the electron density as the central variable rather than the many-body wavefunction. DFT method calculated electron correlation through the general functioning of the electron density, and the functional partitioned the electronic energy into several components that were

calculated individually, including the kinetic energy, the electron-nuclear interaction, the Coulomb repulsion, and an exchange-correlation term accounting for the remainder of the electron-electron interaction.

Hybrid functional is a class of approximations. The physics description is that exchange-correlation energy functional in DFT that includes a portion of exact exchange from Hartree-Fock theory with the rest of exchange-correlation energy from empirical or other sources. The common methods are the B3LYP (Becke, three-parameter, Lee Yang-Parr) [47, 48] and the M06 suite of functionals [49, 50] which are applied in the present study.

2.1.3 Basis Sets Selection

A basis set in theoretical and computational chemistry is a set of functions that be also called basis functions. In quantum chemistry, the basis set often refers to any set of one-particle functions used to build molecular orbitals.

Gaussian-type orbitals (GTOs) and Slater-type orbitals (STOs) are the atomic orbitals [51] and they were used in linear combination to form molecular orbitals. While for the Slater orbitals the radial part is by

$$R_l(r) = A(l, \alpha)r^l e^{-\alpha r} \quad (2.2)$$

$A(l, \alpha)$ being a normalization constant, for the radial part of Gaussian orbitals is by

$$R_l(r) = B(l, \alpha)r^l e^{-\alpha r^2} \quad (2.3)$$

where $B(l, \alpha)$ is the normalization constant corresponding to the Gaussian; r is the distance of the electron from the atomic nucleus; α is a constant related to the effective

charge of the nucleus.

The main difference between these two functions representing the atomic orbitals is the power of r , the distance of the electron from the atomic nucleus. For GTOs, e^{-ar^2} do not capture the cusp of the wavefunction nor the exponential decay in STOs (e^{-r}), so more GTOs are needed to form a suitable basis set to equal STOs, for STOs (e^{-r}) can capture more cusp and the exponential decay, excepting for relatively expensive calculation cost. The computational efficiency more than compensates for the additional number of functions needed, so GTOs are more commonly used in calculations. In the present study, split-valence Gaussian basis sets (6-311++G(d,p)) were used and split the STOs to interpret the atomic orbitals. The basis sets are also augmented with diffuse functions, denoted by ++. Moreover, for improving the angular distribution, the additional set of GTOs of higher angular momentum is also needed to add to the basis set, denoted by (d,p). The meaning of (d,p) is that adds a set of d-type GTOs for each carbon atom and a set of p-type GTOs for the hydrogen atom.

2.1.4 Zero-point Energy Correction

Zero-point energy (ZPE) is the difference between the lowest possible energy that a quantum mechanical system may have and the classical minimum energy of the system. Compared with classical mechanics, because of the Heisenberg uncertainty principle [52], there is constant fluctuation in the lowest energy state in the quantum systems. For comparison with thermochemical data obtained from the experiment, zero-point vibrational energies (ZPVEs) need to convert the total electronic energies

obtained from ab initio quantum mechanical studies into 0 K enthalpy (heat of formation) ΔH_f^0 [53]. In the present study for quantum chemistry calculation, zero-point energy (ZPE) corrections were calculated at the DFT/6-311++G(d,p) method to be consistent with the geometry optimization method.

Chapter 3 An ONIOM-based Thermochemistry Study of Hydrogen

Abstraction Reactions of $n\text{-C}_n\text{H}_{2n+2} + \text{R}$ ($n = 1\text{-}16$, $\text{R} = \text{H}, \text{OH}, \text{HO}_2$)

3.1 Introduction

The contemporary concern for energy safety and environment protection impelled the studies on developing advanced combustion energy conversion devices. The aim of investigating fuel combustion chemistry is to understand and analyze the combustion processes for enhancing combustion efficiency, controlling combustion stability, and reducing combustion emissions [2]. The increasingly higher demand for carbon neutralization necessitates comprehensive and systematic research on petroleum-based fuels for making rational use of them.

There is a well-recognized difficulty to study the combustion chemistry (including thermochemistry and chemical kinetics) of practical fuels, such as gasoline [3], diesel [5], and jet fuel [7] on account of their complicated components. These fuels generally consist of hundreds of different hydrocarbon molecules, and n -alkanes are the primary components of these fuels [3, 5, 7-9, 54]. The widely accepted strategy for mitigating the difficulty is to use surrogate fuels which consist of several typical components to represent these practical fuels. Many previous studies have shown that normally large hydrocarbon molecules containing more than 10 carbon atoms are the primary components in the surrogate fuels [8, 9, 54].

In consideration of the main components of the surrogate fuels representing various practical fuels being large straight-chain alkanes, and that the presences of large

straight-chain alkanes have a great influence on the ignition delay, laminar flame speed, heat release, soot formation, etc., extensive studies have been conducted on the development of chemical kinetics modelling of the surrogate fuels [54-57]. Since a typically detailed reaction mechanism for a large straight-chain alkane involves hundreds of species and thousands of elementary reactions, it is a formidable task to specify thermochemical and kinetic data for such a large number of species and elementary reactions. Due to insufficient theoretical and experimental studies for large hydrocarbon species, the existing detailed mechanisms for large hydrocarbon species [58-60] adopted the thermodynamic data obtained by the THERM program [61, 62] using the group additivity rules of Benson [63].

Recent advances in electronic structure theory have enabled us to obtain thermochemical data for relatively small molecules comparable to those of well-conducted experiments. For example, CCSD(T)/CBS (the coupled cluster theory with single and double excitations and a quasi-perturbative treatment of connected triple excitations, with an extrapolation to complete basis set) usually has uncertainties less than 1.1 kcal/mol [31] for the predictions of barrier height and reaction energy. For QCISD(T)/CBS (the quadratic configuration interaction with singles, doubles, and perturbative inclusion of triples, and with an extrapolation to complete basis sets) yields the predictions with uncertainties around 1.0 kcal/mol [32], and can further be improved the accuracy to 0.6 kcal/mol [33] with the inclusion of a bond additivity correction. However, these high-level methods cannot be applied in a system with more than 10

non-hydrogen atoms in the common capacity of supercomputers. Due to computational infeasibility, most reaction systems were studied at lower levels, such as CBS-QB3 [64] and B3LYP/6-31G(d,p) [65].

Zhang and Zhang [35] proposed a two-layer ONIOM (our own N-layered integrated molecular orbital and molecular mechanics) method [66], in which the QCISD(T)/CBS method is used for the high layer and the B3LYP-favor density functional theory (DFT) method for the low layer. The ONIOM [QCISD(T)/CBS:DFT] method was systematically validated in the studies of hydrogen abstraction reaction systems of saturated and unsaturated alkyl esters by hydrogen radical [35, 67]. The calculated energies were in very good agreement with those obtained using the QCISD(T)/CBS method, as verified by the discrepancies being generally less than 0.15 kcal/mol in almost all the test cases.

Among the key combustion-relevant reactions being considered are the hydrogen abstraction reactions of these straight-chain alkanes by the hydrogen (H), hydroxyl (OH), and hydroperoxyl (HO₂) radicals [29, 68, 69]. In consideration of hydrocarbon molecules using high-level ab initio chemical kinetics, the majority of the previous studies mainly revolved around relatively small hydrocarbon molecules [25, 26, 28, 29], because the prevalent high-level electronic structure theory-based methods are computationally demanding for the large hydrocarbon molecules.

Based on the above consideration and to the knowledge of the authors, little thermochemical or kinetics data for the large straight-chain alkanes have been obtained

by using high-level theoretical methods. Therefore, in the present work, we aim to systematically study the hydrogen abstraction reactions of large straight-chain alkanes, $n\text{-C}_n\text{H}_{2n+2}$ ($n = 1\text{-}16$), by H, OH, and HO₂ radicals using a demonstrated high-level ONIOM[QCISD(T)/CBS:DFT] method [35]. In the three different types of hydrogen abstraction reactions, all hydrogen abstraction sites have been studied for each reaction system, rendering 72 reactions (denoted by H-R1 to H-R72) for $n\text{-C}_n\text{H}_{2n+2} + \text{H}$, 72 reactions (denoted by OH-R1 to OH-R72) for $n\text{-C}_n\text{H}_{2n+2} + \text{OH}$, and 72 reactions (denoted by HO₂-R1 to HO₂-R72) for $n\text{-C}_n\text{H}_{2n+2} + \text{HO}_2$.

Up to now, there are few direct experimental measurements for these reactions ($n > 4$) [25]. Furthermore, the majority of the previous high-level ab initio studies were mainly focused on relatively small hydrocarbon molecules [25, 26, 70], partially because the prevalent high-level electronic structure theories are computationally demanding for the large hydrocarbon molecules. Consequently, the present work will not only demonstrate the applicability of the ONIOM method in large straight-chain hydrocarbons but also provide useful benchmark data for their thermochemistry.

3.2 Computational methods

3.2.1 Potential Energy Surfaces

The geometries optimization and vibrational frequencies for all stationary points on the potential energy surfaces of these hydrogen abstraction reactions were calculated at the calculated at the B3LYP/6-311++G(d,p) level [71] for both $n\text{-C}_n\text{H}_{2n+2} + \text{H}$ and $n\text{-C}_n\text{H}_{2n+2} + \text{HO}_2$ ($n = 1\text{-}16$), and at the M06-2X/6-311++G(d,p) level [72] for $n\text{-C}_n\text{H}_{2n+2}$

+ OH ($n = 1-16$). The identified transition states in the reactions are confirmed by IRC to examine the connections of each saddle point to its local minima. Zero-point energy (ZPE) corrections were obtained at a consistent level with the reactions.

3.2.2 QCISD(T)/CBS Single-Point Energies

In the present study, the number of non-hydrogen atoms (carbon and oxygen atoms) in the hydrogen abstraction reaction systems of n -C_nH_{2n+2} + H, OH, and HO₂ ($n=1-16$), determines the computational load. For relatively small molecules, there are two high-level methods (QCISD(T)/CBS) which are computationally affordable, and these two methods were used to produce benchmark data to validate the ONIOM method. For [QCISD(T)/CBS]₁, it is based on the direct extrapolation of the energies with correlation-consistent, polarized valence, cc-pVTZ, and cc-pVQZ basis sets of Dunning [73, 74] to the complete basis set (CBS) limit [75] by

$$\begin{aligned} E[\text{QCISD(T)/CBS}]_1 &= E[\text{QCISD(T)/CBS}]_{\text{TZ} \rightarrow \text{QZ}} \\ &= E[\text{QCISD(T)/QZ}] + \{E[\text{QCISD(T)/QZ}] \\ &\quad - E[\text{QCISD(T)/TZ}]\} \times 0.6938 \end{aligned} \quad (3.1)$$

However, when the number of non-hydrogen atoms in reactions is more than 5, the computation cost of Eq. (3.1) increases significantly. Therefore, we adopted an alternative [QCISD(T)/CBS]₂ method [76] given by

$$\begin{aligned} E[\text{QCISD(T)/CBS}]_2 &= E[\text{QCISD(T)/CBS}]_{\text{DZ} \rightarrow \text{TZ}} + \{E[\text{MP2/CBS}]_{\text{TZ} \rightarrow \text{QZ}} \\ &\quad - E[\text{MP2/CBS}]_{\text{DZ} \rightarrow \text{TZ}}\} \end{aligned} \quad (3.2)$$

where,

$$E[\text{QCISD(T)/CBS}]_{\text{DZ} \rightarrow \text{TZ}} = E[\text{QCISD(T)/TZ}] + \{E[\text{QCISD(T)/TZ}] - E[\text{QCISD(T)/DZ}]\} \times 0.4629 \quad (3.3)$$

$$E[\text{MP2/CBS}]_{\text{TZ} \rightarrow \text{QZ}} = E[\text{MP2/QZ}] + \{E[\text{MP2/QZ}] - E[\text{MP2/TZ}]\} \times 0.6938 \quad (3.4)$$

$$E[\text{MP2/CBS}]_{\text{DZ} \rightarrow \text{TZ}} = E[\text{MP2/TZ}] + \{E[\text{MP2/TZ}] - E[\text{MP2/DZ}]\} \times 0.4629 \quad (3.5)$$

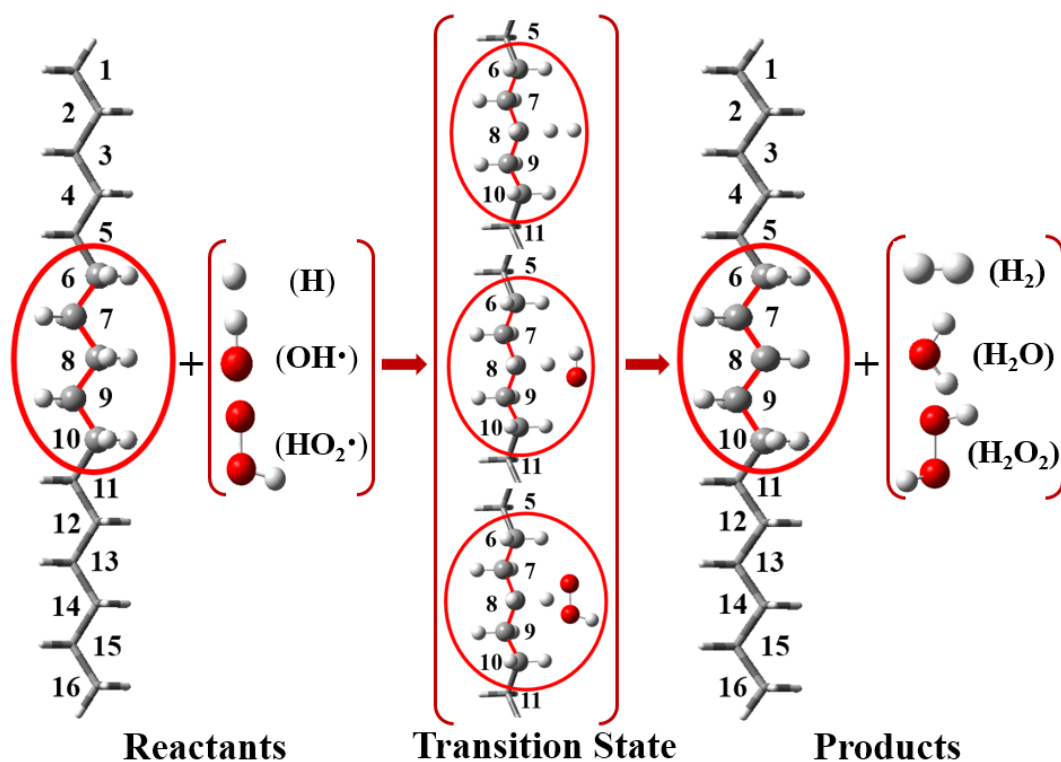


Figure 3.1 Illustration of the ONIOM[QCISD(T)/CBS:DFT]/CAP(2,2) method for the hydrogen abstraction reaction by H, OH, and HO₂ radicals, C₁₆H₃₄ + (H, OH, and HO₂) → CH₃(CH₂)₄CH(CH₂)₅CH₃ + (H₂, H₂O, and H₂O₂). The indices from 1-16 denote the CH₃ (or CH₂) groups. CAP (2,2) (in the circle) represents the chemically active portion consisting of the No.6 and No.7 CH₂ groups on the one side of the No. 8 CH₂ group under hydrogen attack, and No. 9 and No. 10 CH₂ groups on the other side of No. 8 CH₂ group in reactant and products. For the transition state, H, OH, and HO₂ radicals are also needed to be added to the CAP.

2.2.3 ONIOM[QCISD(T)/CBS] Single-Point Energies

The present ONIOM[QCISD(T)/CBS] method was proposed by Zhang and Zhang [35] and has been studied and validated in large biodiesel molecules including saturated

and unsaturated systems for its accuracy and efficiency [35, 67, 77]. It constructs a reaction system by defining two layers, which are treated at two different theoretical levels. The high-level layer called the chemically active portion (denoted by CAP) is treated at the QCISD(T)/CBS level, while the low-level layer is treated at the DFT/6-311++G(d,p) level. An important part of the ONIOM method is to define the CAP appropriately, for it directly influences the calculation accuracy and computational efficiency. The CAP comprises the CH₂ (or CH₃) under attack, the attacking radicals (H, OH, and HO₂ in the present study), and the neighboring groups. The accuracy and efficiency of the choice of link atoms have been substantiated [35, 67]. CAP (2,2) is minimally required for the present study, and it comprises the CH₂ (or CH₃) under attack and two neighboring groups (if exist) on both sides. Figure 3.1 shows the representative schematic for the hydrogen abstraction reactions of *n*-C₁₆H₃₄ + (H, OH, and HO₂) using the ONIOM method with CAP(2,2).

The ONIOM method predicts the energy of the whole system by using the low-level energy of the system with the available correction for the difference of the CAP between the high-level and the low-level:

$$E^{\text{ONIOM}}[\text{High: Low}] = E^{\text{Low}}(\text{R}) + E^{\text{High}}(\text{CAP}) - E^{\text{Low}}(\text{CAP}) \quad (3.6)$$

Using the DFT/6-311++G(d,p) method for the low-level and the [QCISD(T)/CBS]₂ method for the high-level, the ONIOM energies are given by:

$$E^{\text{ONIOM}}[\text{QCISD(T)CBS: DFT}] = E^{\text{ONIOM}}[\text{QCISD(T)/CBS: DFT}]_{\text{DZ} \rightarrow \text{TZ}} \\ + \{E^{\text{ONIOM}}[\text{MP2/CBS: DFT}]_{\text{TZ} \rightarrow \text{QZ}}\}$$

$$- E^{\text{ONIOM}}[\text{MP2/CBS: DFT}]_{\text{DZ} \rightarrow \text{TZ}} \quad (3.7)$$

where,

$$\begin{aligned} E^{\text{ONIOM}}[\text{QCISD(T)/CBS: DFT}]_{\text{DZ} \rightarrow \text{TZ}} &= E^{\text{ONIOM}}[\text{QCISD(T)/TZ: DFT}] \\ &+ \{E^{\text{ONIOM}}[\text{QCISD(T)/TZ: DFT}] \\ &- E^{\text{ONIOM}}[\text{QCISD(T)/DZ: DFT}]\} \times 0.4629 \quad (3.8) \end{aligned}$$

$$\begin{aligned} E^{\text{ONIOM}}[\text{MP2/CBS: DFT}]_{\text{TZ} \rightarrow \text{QZ}} &= E^{\text{ONIOM}}[\text{MP2/QZ: DFT}] \\ &+ \{E^{\text{ONIOM}}[\text{MP2/QZ: DFT}] \\ &- E^{\text{ONIOM}}[\text{MP2/TZ: DFT}]\} \times 0.6938 \quad (3.9) \end{aligned}$$

$$\begin{aligned} E^{\text{ONIOM}}[\text{MP2/CBS: DFT}]_{\text{DZ} \rightarrow \text{TZ}} &= E^{\text{ONIOM}}[\text{MP2/TZ: DFT}] \\ &+ \{E^{\text{ONIOM}}[\text{MP2/TZ: DFT}] \\ &- E^{\text{ONIOM}}[\text{MP2/DZ: DFT}]\} \times 0.4629 \quad (3.10) \end{aligned}$$

The energy barrier (denoted as EB hereinafter) and the heat of reaction (denoted as HR hereinafter) with ZPE corrections are calculated by the difference between the energy ($E^{\text{ONIOM}}[\text{QCISD(T)/TZ: DFT}] + \text{ZPE}$) of the reactants and the transition states for EB, and of the reactants and the products for HR:

$$\begin{aligned} \text{EB} &= (E^{\text{ONIOM}}[\text{QCISD(T)/CBS: DFT}] + \text{ZPE})_{\text{TS}} \\ &- (E^{\text{ONIOM}}[\text{QCISD(T)/CBS: DFT}] + \text{ZPE})_{\text{reactants}} \quad (3.11) \end{aligned}$$

$$\begin{aligned} \text{HR} &= (E^{\text{ONIOM}}[\text{QCISD(T)/CBS: DFT}] + \text{ZPE})_{\text{products}} \\ &- (E^{\text{ONIOM}}[\text{QCISD(T)/CBS: DFT}] + \text{ZPE})_{\text{reactants}} \quad (3.12) \end{aligned}$$

All the calculations in the present study were performed by the Gaussian 09 program package [78].

3.3 Results and Discussion

3.3.1 Hydrogen Abstraction Reaction of $n\text{-C}_n\text{H}_{2n+2} + \text{H}$ ($n = 1\text{-}16$)

3.3.1.1 Validation and Comparison of Two [QCISD(T)/CBS] Methods

For the relatively small molecules, the two high-level methods are computationally affordable and used to establish the benchmark data to validate the present ONIOM method. For $n\text{-C}_n\text{H}_{2n+2} + \text{H}$, the reactions can be validated up to $n = 5$ by using [QCISD(T)/CBS]₁ and up to $n = 9$ by [QCISD(T)/CBS]₂. It is seen that [QCISD(T)/CBS]₂ always predicts slightly lower energies (EB and HR) than does [QCISD(T)/CBS]₁. The computational differences (absolute values) of these two [QCISD(T)/CBS] methods are generally less than 0.10 kcal/mol, as shown in Table 3.1. The only exceptional case is the reaction H-R1, for which the differences between the two methods are -0.11 kcal/mol for EB and -0.15 kcal/mol for HR.

Table 3.1 The comparison of calculated results (EB and HR) for the hydrogen abstraction reactions of $n\text{-C}_n\text{H}_{2n+2} + \text{H}$ ($n = 1\text{-}5$) using the [QCISD(T)/CBS]₁ and [QCISD(T)/CBS]₂ (unit: kcal/mol).

Reactions	EB			HR		
	[QCISD(T)/CBS] ₁	[QCISD(T)/CBS] ₂	Difference	[QCISD(T)/CBS] ₁	[QCISD(T)/CBS] ₂	Difference
H-R1: $\text{H} + \text{CH}_4 \rightarrow \text{H}_2 + \text{CH}_3$	13.45	13.34	0.11	-0.15	-0.30	0.15
H-R2: $\text{H} + \text{CH}_3\text{CH}_3 \rightarrow \text{H}_2 + \text{CH}_2\text{CH}_3$	10.27	10.17	0.10	-3.96	-4.05	0.09
H-R3: $\text{H} + \text{CH}_3\text{CH}_2\text{CH}_3 \rightarrow \text{H}_2 + \text{CH}_2\text{CH}_2\text{CH}_3$	10.21	10.11	0.10	-3.58	-3.66	0.08
H-R4: $\text{H} + \text{CH}_3\text{CH}_2\text{CH}_3 \rightarrow \text{H}_2 + \text{CH}_3\text{CHCH}_3$	7.58	7.49	0.09	-6.72	-6.74	0.02
H-R5: $\text{H} + \text{CH}_3(\text{CH}_2)_2\text{CH}_3 \rightarrow \text{H}_2 + \text{CH}_2(\text{CH}_2)_2\text{CH}_3$	10.11	10.01	0.10	-3.64	-3.73	0.09
H-R6: $\text{H} + \text{CH}_3(\text{CH}_2)_2\text{CH}_3 \rightarrow \text{H}_2 + \text{CH}_3\text{CHCH}_2\text{CH}_3$	7.47	7.39	0.08	-6.43	-6.45	0.02
H-R7: $\text{H} + \text{CH}_3(\text{CH}_2)_3\text{CH}_3 \rightarrow \text{H}_2 + \text{CH}_2(\text{CH}_2)_3\text{CH}_3$	10.04	9.95	0.09	-3.61	-3.69	0.08
H-R8: $\text{H} + \text{CH}_3(\text{CH}_2)_3\text{CH}_3 \rightarrow \text{H}_2 + \text{CH}_3\text{CH}(\text{CH}_2)_2\text{CH}_3$	7.46	7.38	0.08	-6.43	-6.45	0.02
H-R9: $\text{H} + \text{CH}_3(\text{CH}_2)_3\text{CH}_3 \rightarrow \text{H}_2 + \text{CH}_3\text{CH}_2\text{CHCH}_2\text{CH}_3$	7.46	7.38	0.08	-6.11	-6.13	0.02

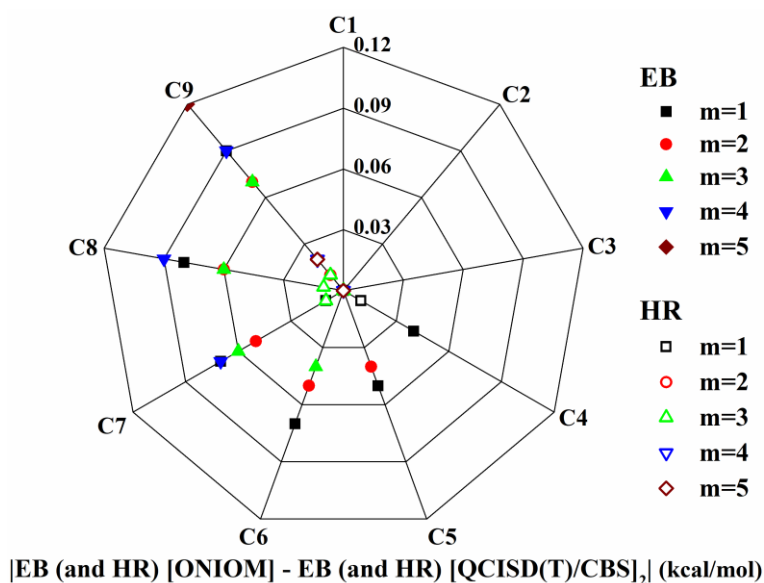


Figure 3.2 The difference between the calculated energy barriers (EB) and heat of reactions (HR), for the reactions of $n\text{-C}_n\text{H}_{2n+2} + \text{H}$ ($n = 1\text{-}9$); The notation m ($= 1\text{-}5$) denotes the group under hydrogen attack.

3.3.1.2 Validation of ONIOM Energies of $n\text{-C}_n\text{H}_{2n+2} + \text{H}$ ($n = 1\text{-}9$)

Through the above comparison between the two [QCISD(T)/CBS] methods, the [QCISD(T)/CBS]₂ method can be considered as a high-level method to validate the ONIOM method for the systems with more than 5 non-hydrogen atoms, which are computationally expensive for the [QCISD(T)/CBS]₁ method. Therefore, we made a comparison of the calculated results (EB and HR) for $n\text{-C}_n\text{H}_{2n+2} + \text{H}$ ($n = 1\text{-}9$) by using the ONIOM[QCISD(T)/CBS:DFT] and [QCISD(T)/CBS]₂ methods for the totally 25 reactions (refer to H-R1 to H-R25 as shown in Table S3.1 in Appendix of section 3.6). It is seen that the ONIOM method always predicts slightly higher energies than the [QCISD(T)/CBS]₂ method. The computational differences between these two methods are generally less than 0.10 kcal/mol, as shown in Figure 3.2 and Table S3.1 in Appendix of section 3.6., except for the reaction H-R25, which yields a difference of

0.12 kcal/mol. A slightly augmented CAP(3,3) should be able to reduce the relative error for the case of H-R25.

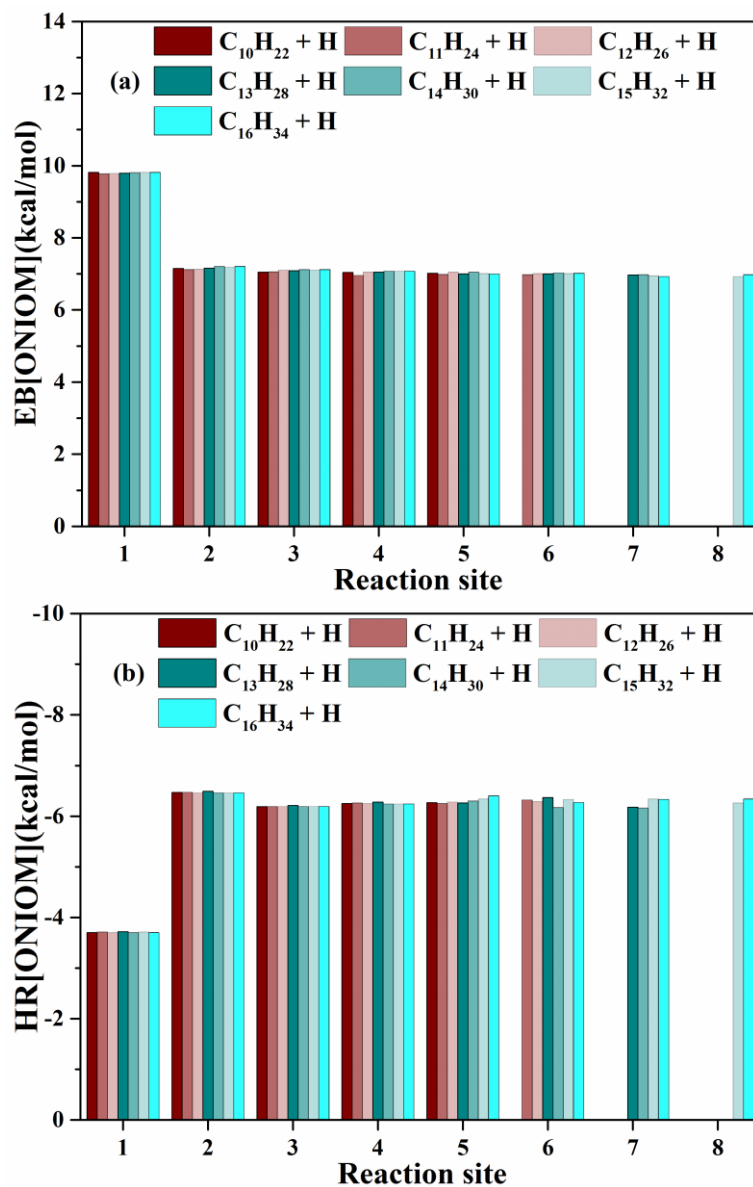


Figure 3.3 (a) The predicted EBs and (b) the predicted HRs for the hydrogen abstraction reactions of n -C_nH_{2n+2} + H ($n = 10-16$).

3.3.1.3 ONIOM Energies of n -C_nH_{2n+2} + H ($n = 10-16$)

After validating the accuracy of the ONIOM method, we used it to study the larger reaction systems of n -C_nH_{2n+2} + H ($n = 10-16$) at various (all) hydrogen abstraction sites, with a total of 47 reactions (refer to H-R26 to H-R72 as shown in Table S3.2 in

Appendix of section 3.6). These reactions have not been previously studied by using high-level methods. The calculated energies, EB and HR, are shown in Figure 3.3 and Table S3.2 in Appendix of section 3.6. Several observations can be made from these results:

The hydrogen abstraction reactions occurring at CH₃ groups (denoted by 1 in the reaction site) have the highest EBs of around 9.80 kcal/mol, with the range from 9.78 to 9.82 kcal/mol, and the highest (negative) HRs of around -3.71 kcal/mol, with the range from -3.72 to -3.70 kcal/mol.

The hydrogen abstraction reactions occurring at CH₂ groups (denoted by 2~8 in the reaction site) have almost the same EBs of around 7.05 kcal/mol, with the range from 6.93 to 7.21 kcal/mol, and HRs of around -6.30 kcal/mol with the range from -6.49 to -6.16 kcal/mol.

The energies (EBs and HRs) variation for n -C_nH_{2n+2} + H ($n = 10-16$) are negligible for the hydrogen abstraction reactions occurring at CH₃ and CH₂ groups, because the coefficients of variation ($C_v = \left| \frac{\sigma}{\mu} \right|$, σ is standard deviation and μ is arithmetic mean) are 0.2% (EB) and 0.2% (HR) for CH₃ groups and 1.0% (EB) and 1.5% (HR) for CH₂ groups.

3.3.2 Hydrogen Abstraction Reaction of n -C_nH_{2n+2} + OH ($n = 1-16$)

We used the M06-2X/6-311++G(d,p) method to study the reaction systems of n -C_nH_{2n+2} + OH because we found the imaginary frequencies of n -C_nH_{2n+2} + OH at B3LYP/6-311++G(d,p) level are relatively smaller than those of n -C_nH_{2n+2} + H and n -

$C_nH_{2n+2} + HO_2$ at the same level of theory. Taking C_3H_8 as an example, the imaginary frequencies of the transition states for the reactions occurring at the methyl group, are $207.77i\text{ cm}^{-1}$ for OH-R3, $1160.15i\text{ cm}^{-1}$ for H-R3, and $1649.88i\text{ cm}^{-1}$ for HO_2 -R3. When the reactions occur at other reaction sites, the imaginary frequencies of the transition states for $n-C_nH_{2n+2} + OH$ dramatically decrease, e.g. $44.96i\text{ cm}^{-1}$ for OH-R4 compared with $1123.81i\text{ cm}^{-1}$ for H-R4, and $1663.22i\text{ cm}^{-1}$ for HO_2 -R4. Due to the relatively small imaginary frequencies for $n-C_nH_{2n+2} + OH$, it is difficult to use intrinsic reaction coordinate (IRC) to confirm the transition state. Therefore, we adopted the M06-2X method with the same basis set of 6-311++G(d,p) to deal with all the reactions of $n-C_nH_{2n+2} + OH$ ($n = 1-16$). Taking C_3H_8 as an example again, the imaginary frequencies of the transition states of OH-R3 and OH-R4 are $788.88i\text{ cm}^{-1}$ and $535.31i\text{ cm}^{-1}$.

Table 3.2 The comparison of calculated results (EB and HR) for the hydrogen abstraction reactions of $n-C_nH_{2n+2} + OH$ ($n = 1-4$) using the [QCISD(T)/CBS]₁ and [QCISD(T)/CBS]₂ (unit: kcal/mol).

Reactions	EB			HR		
	[QCISD(T)/CBS] ₁	[QCISD(T)/CBS] ₂	Difference	[QCISD(T)/CBS] ₁	[QCISD(T)/CBS] ₂	Difference
OH-R1: $OH + CH_4 \rightarrow H_2O + CH_3$	4.83	5.02	0.19	-14.84	-14.97	0.13
OH-R2: $OH + CH_3CH_3 \rightarrow H_2O + CH_2CH_3$	2.43	2.63	0.20	-18.42	-18.48	0.06
OH-R3: $OH + CH_3CH_2CH_3 \rightarrow H_2O + CH_2CH_2CH_3$	1.63	1.81	0.18	-18.40	-18.46	0.06
OH-R4: $OH + CH_3CH_2CH_3 \rightarrow H_2O + CH_3CHCH_3$	0.29	0.49	0.20	-21.47	-21.47	0.02
OH-R5: $OH + CH_3(CH_2)_2CH_3 \rightarrow H_2O + CH_2(CH_2)_2CH_3$	2.72	2.88	0.16	-17.29	-17.36	0.07
OH-R6: $OH + CH_3(CH_2)_2CH_3 \rightarrow H_2O + CH_3CHCH_2CH_3$	0.81	0.99	0.18	-20.27	-20.27	0.00

3.3.2.1 Validation and Comparison of Two QCISD(T)/CBS Methods

For $n-C_nH_{2n+2} + OH$, the reactions can be validated up to $n = 4$ by using the [QCISD(T)/CBS]₁ method and up to $n=8$ by the [QCISD(T)/CBS]₂ method. Unlike the

systems of $n\text{-C}_n\text{H}_{2n+2} + \text{H}$ ($n=1-5$), the $[\text{QCISD(T)/CBS}]_2$ method always predicts higher EB and lower HR than the $[\text{QCISD(T)/CBS}]_1$ method for $n\text{-C}_n\text{H}_{2n+2} + \text{OH}$ ($n=1-4$). The computational differences (absolute values) of these two $[\text{QCISD(T)/CBS}]$ methods are generally less than 0.20 kcal/mol for EB and 0.10 kcal/mol for HR, as shown in Table 3.2.

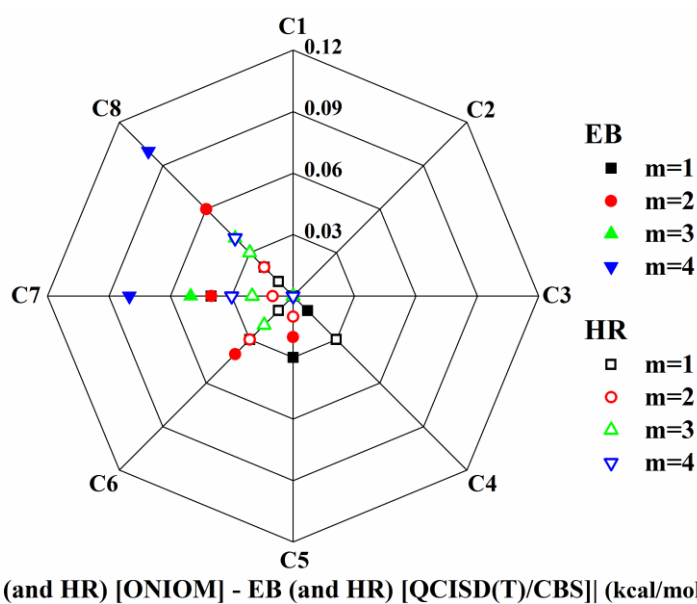


Figure 3.4 The difference between the calculated energy barriers (EB) and heat of reactions (HR), for the reactions of $n\text{-C}_n\text{H}_{2n+2} + \text{OH}$ ($n=1-8$); The notation m ($=1-4$) denotes the group under hydroxyl (OH) attack.

3.3.2.2 Validation of ONIOM Energies of $n\text{-C}_n\text{H}_{2n+2} + \text{OH}$ ($n = 1-8$)

We adopted the $[\text{QCISD(T)/CBS}]_2$ method to validate the ONIOM method for $n\text{-C}_n\text{H}_{2n+2} + \text{OH}$ ($n=1-8$). A total of 20 reactions (refer to OH-R1 to OH-R20 as shown in Table S3.3 in Appendix of section 3.6) have been compared. As with the systems of $n\text{-C}_n\text{H}_{2n+2} + \text{H}$ ($n=1-9$), the ONIOM method always predicts slightly higher EBs than the $[\text{QCISD(T)/CBS}]_2$ method, but it predicts almost negligibly smaller HR than the latter. The computational differences (absolute values) between these two methods are less

than 0.10 kcal/mol for EB and 0.04 kcal/mol for HR, as shown in Figure 3.4 and Table S3.3 in Appendix of section 3.6.

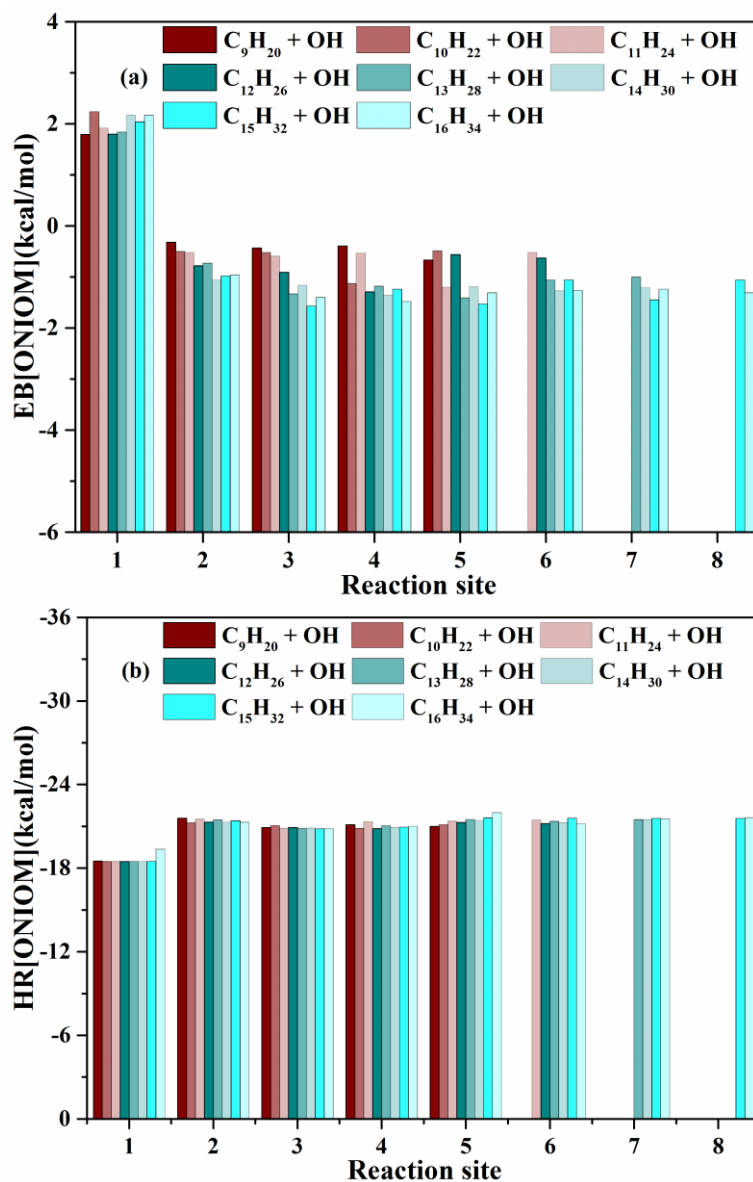


Figure 3.5 (a) The predicted EBs and (b) the predicted HRs for the hydrogen abstraction reactions of n - $C_nH_{2n+2} + OH$ ($n = 9-16$).

3.3.2.3 ONIOM Energies of n - $C_nH_{2n+2} + OH$ ($n = 9-16$)

We used the ONIOM method to study the larger reaction systems of n - $C_nH_{2n+2} + OH$ ($n = 9-16$) at various (all) hydrogen abstraction sites, with a total of 52 reactions (refer to OH-R21 to OH-R72 as shown in Table S3.4 in Appendix of section 3.6). These

reactions have not been previously studied by using high-level methods. The calculated energies, EB and HR, are shown in Figure 3.5 and Table S3.4 in Appendix of section 3.6. Several observations can be made from these results:

The hydrogen abstraction reactions occurring at CH₃ groups (denoted by 1 in the reaction site) have the highest EBs of around 2.00 kcal/mol, with the range from 1.79 to 2.24 kcal/mol, and the highest (negative) HRs of around -18.59 kcal/mol, with the range from -19.35 to -18.46 kcal/mol.

The hydrogen abstraction reactions occurring at CH₂ groups (denoted by 2~8 in the reaction site) have the fluctuating EBs from -1.57 to -0.32 kcal/mol with around -1.00 kcal/mol, and almost the same HRs of around -21.25 kcal/mol, with the range from -21.98 to -20.82 kcal/mol.

For $n\text{-C}_n\text{H}_{2n+2} + \text{OH}$ ($n = 9\text{-}16$), there are obvious variations in the EBs for the hydrogen abstraction reactions occurring at CH₃ groups with the coefficients of variation $C_v = 8.5\%$ and at CH₂ groups with $C_v = 36.1\%$. This result suggests that approximating the EBs for hydrogen abstraction from the CH₂ group by OH as a constant would cause significant errors in chemical kinetics calculations. Furthermore, the variation of HRs is negligible as C_v is 1.5% for CH₃ groups and 1.3% for CH₂ groups.

3.3.3 Hydrogen Abstraction Reaction of $n\text{-C}_n\text{H}_{2n+2} + \text{HO}_2$ ($n = 1\text{-}16$)

3.3.3.1 Validation of Comparison of Two QCISD(T)/CBS Methods

For $n\text{-C}_n\text{H}_{2n+2} + \text{HO}_2$, the reactions can be validated up to $n = 3$ by using the

[QCISD(T)/CBS]₁ method and up to 7 by using the [QCISD(T)/CBS]₂ method. Similar to the systems of $n\text{-C}_n\text{H}_{2n+2} + \text{H}$ ($n=1-5$), the [QCISD(T)/CBS]₂ method always predicts lower energies (both EBs and HRs) than ([QCISD(T)/CBS]₁ for $n\text{-C}_n\text{H}_{2n+2} + \text{HO}_2$ ($n=1-3$). The computational differences (absolute values) of these two [QCISD(T)/CBS] methods are generally less than 0.11 kcal/mol, as shown in Table 3.3. The only exceptional case is the reaction HO₂-R1, for which the differences between the two methods are -0.18 kcal/mol for EB and -0.17 kcal/mol for HR.

Table 3.3 The comparison of calculated results (EB and HR) for the hydrogen abstraction reactions of $n\text{-C}_n\text{H}_{2n+2} + \text{HO}_2$ ($n = 1-3$) using the [QCISD(T)/CBS]₁ and [QCISD(T)/CBS]₂ (unit: kcal/mol).

Reactions	EB			HR		
	[QCISD(T)/	[QCISD(T)/	Difference	[QCISD(T)/	[QCISD(T)/	Difference
	CBS] ₁	CBS] ₂		CBS] ₁	CBS] ₂	
HO ₂ -R1: HO ₂ + CH ₄ → H ₂ O ₂ + CH ₃	24.29	24.11	0.18	17.21	17.04	0.17
HO ₂ -R2: HO ₂ + CH ₃ CH ₃ → H ₂ O ₂ + CH ₂ CH ₃	20.01	19.90	0.11	13.40	13.29	0.11
HO ₂ -R3: HO ₂ + CH ₃ CH ₂ CH ₃ → H ₂ O ₂ + CH ₂ CH ₂ CH ₃	19.51	19.40	0.09	13.78	13.68	0.10
HO ₂ -R4: HO ₂ + CH ₃ CH ₂ CH ₃ → H ₂ O ₂ + CH ₃ CHCH ₃	16.92	16.86	0.06	10.64	10.60	0.04

3.3.3.2 Validation of ONIOM Energies of $n\text{-C}_n\text{H}_{2n+2} + \text{HO}_2$ ($n = 1-7$)

We used the same method as above to treat the reaction systems of $n\text{-C}_n\text{H}_{2n+2} + \text{HO}_2$ ($n=1-7$), a total of 16 reactions (refer to HO₂-R1 to HO₂-R16 as shown in Table S3.5 in Appendix of section 3.6). As expected, the ONIOM method predicts slightly larger energies (both EB and HR) than the [QCISD(T)/CBS]₂ method. The computational differences between these two methods are generally less than 0.07 kcal/mol for EB and 0.01 kcal/mol for HR, as shown in Figure 3.6 and Table S3.5 in Appendix of section 3.6. The slightly large discrepancy of 0.11 kcal/mol for HO₂-R16 is probably because

CAP(2,2) includes almost CH₂ groups except for the two terminal methyl groups.

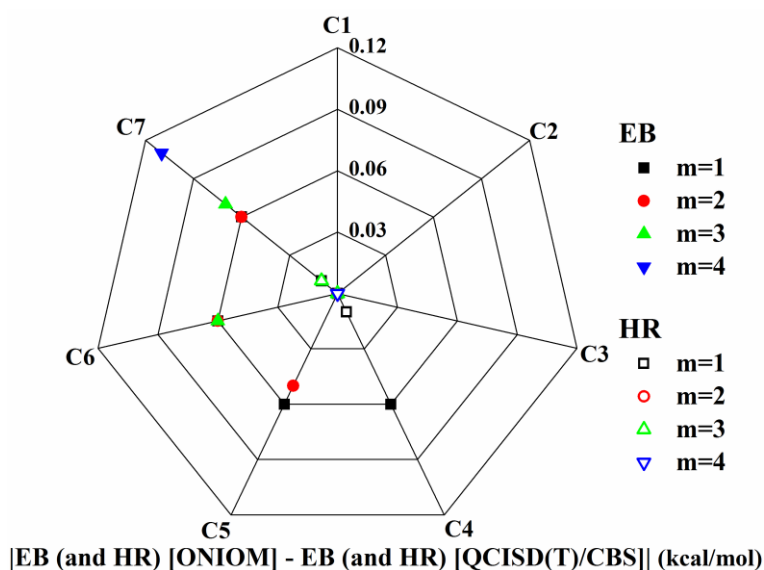


Figure 3.6 The difference between the calculated energy barriers (EB) and heat of reactions (HR), for the reactions of $n\text{-C}_n\text{H}_{2n+2} + \text{HO}_2$ ($n = 1\text{-}7$); The notation m ($= 1\text{-}4$) denotes the group under hydroperoxyl (HO_2) attack.

3.3.3.3 ONIOM Energies of $n\text{-C}_n\text{H}_{2n+2} + \text{HO}_2$ ($n = 8\text{-}16$)

We used the ONIOM method to study the larger reaction systems of $n\text{-C}_n\text{H}_{2n+2} + \text{HO}_2$ ($n = 8\text{-}16$) at various (all) hydrogen abstraction sites, with a total of 56 reactions (refer to R17 to R72 as shown in Table S3.6 in Appendix of section 3.6). These reactions have not been previously studied by using high-level methods. The calculated energies, EB and HR, are shown in Figure 3.7 and Table S3.6 in Appendix of section 3.6. Several observations can be made from these results:

The hydrogen abstraction reactions occurring at CH₃ groups (denoted by 1 in the reaction site) have the highest EBs of around 19.45 kcal/mol, with the range from 19.00 to 19.69 kcal/mol, and the highest HRs of around 13.63 kcal/mol, with the range from 13.62 to 13.64 kcal/mol.

The hydrogen abstraction reactions occurring at CH₂ groups (denoted by 2~8 in the reaction site) have slightly fluctuation for EBs of around 15.99 kcal/mol, with the range from 15.45 to 16.58 kcal/mol, and have almost the same HRs of around 11.05 kcal/mol with the range from 10.85 to 11.18 kcal/mol.

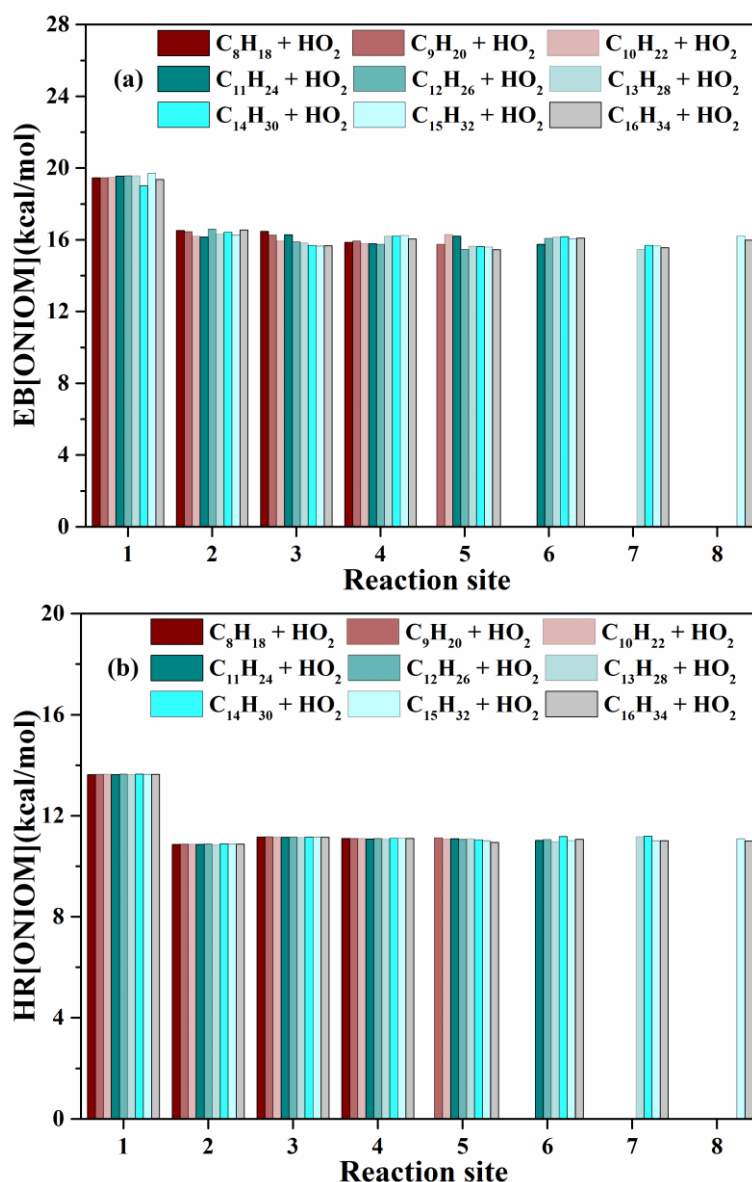


Figure 3.7 (a) The predicted EBs and (b) the predicted HRs for the hydrogen abstraction reactions of $n\text{-C}_n\text{H}_{2n+2} + \text{HO}_2$ ($n = 8-16$).

The energies (EB and HR) variation for $n\text{-C}_n\text{H}_{2n+2} + \text{HO}_2$ ($n = 8-16$) are negligible for the hydrogen abstraction reactions occurring at CH₃ and CH₂ groups, because the

coefficients of variation C_v are 0.9% (EB) and 0.04% (HR) for CH₃ groups and 2.0% (EB) and 0.9% (HR) for CH₂ groups.

3.3.4 Comparison of Computational Expense between QCISD(T)/CBS and ONIOM methods

For the reactions of $n\text{-C}_n\text{H}_{2n+2} + \text{H}$, OH, and HO₂, the comparison of computational expense between QCISD(T) and ONIOM methods was also summarized and analyzed. The results are shown in Table 3.4. The notation in Table 3.4 denotes different methods with basis sets. 1: QCISD(T)/cc-pVTZ; 2: QCISD(T)/cc-pVDZ; 3: MP2/cc-pVQZ; 4: MP2/cc-pVTZ; 5: MP2/cc-pVDZ. As an expression of the calculation cost of these two methods, the reactions which contain more non-hydrogen atoms are selected.

For the reactions of $n\text{-C}_n\text{H}_{2n+2} + \text{H}$, H-R21 (9 non-hydrogen atoms for QCISD(T)/CBS, and 3 non-hydrogen atoms for ONIOM) and H-R25 (9 non-hydrogen atoms for QCISD(T)/CBS, and 5 non-hydrogen atoms for ONIOM) are as representative reactions.

For the reactions of $n\text{-C}_n\text{H}_{2n+2} + \text{OH}$, OH-R17 (9 non-hydrogen atoms for QCISD(T)/CBS, and 4 non-hydrogen atoms for ONIOM) and OH-R20 (9 non-hydrogen atoms for QCISD(T)/CBS, and 6 non-hydrogen atoms for ONIOM) are as representative reactions.

For the reactions of $n\text{-C}_n\text{H}_{2n+2} + \text{HO}_2$, HO₂-R13 (9 non-hydrogen atoms for QCISD(T)/CBS, and 5 non-hydrogen atoms for ONIOM) and HO₂-R16 (9 non-hydrogen atoms for QCISD(T)/CBS, and 7 non-hydrogen atoms for ONIOM) are as

representative reactions.

Table 3.4 The comparison of computation times with the QCISD(T)/CBS and ONIOM methods. (unit: minutes)

Reactions	Species	1	2	3	4	5
H-R21 (QCISD(T)/CBS)	CH ₃ (CH ₂) ₇ CH ₃	40898	1133	1929	115	12
	CH ₂ (CH ₂) ₇ CH ₃	96492	3139	6160	187	26
	Transition State	216472	3577	10422	334	21
H-R21 (ONIOM)	CH ₃ (CH ₂) ₇ CH ₃	102	21	93	23	20
	CH ₂ (CH ₂) ₇ CH ₃	170	41	107	45	33
	Transition State	288	54	199	51	41
H-R25 (QCISD(T)/CBS)	CH ₃ (CH ₂) ₇ CH ₃	40898	1133	1929	115	12
	CH ₃ (CH ₂) ₃ CH(CH ₂) ₃ CH ₃	99543	2665	4040	202	24
	Transition State	230464	3314	7155	324	18
H-R25 (ONIOM)	CH ₃ (CH ₂) ₇ CH ₃	1341	47	253	33	17
	CH ₃ (CH ₂) ₃ CH(CH ₂) ₃ CH ₃	1732	71	307	40	24
	Transition State	4208	191	671	99	48
OH-R17 (QCISD(T)/CBS)	CH ₃ (CH ₂) ₆ CH ₃	24272	823	1185	86	5
	CH ₂ (CH ₂) ₆ CH ₃	48072	1662	2838	213	13
	Transition State	164350	5627	7604	254	22
OH-R17 (ONIOM)	CH ₃ (CH ₂) ₆ CH ₃	97	23	84	22	18
	CH ₂ (CH ₂) ₆ CH ₃	147	38	133	40	33
	Transition State	1516	110	371	78	67
OH-R20 (QCISD(T)/CBS)	CH ₃ (CH ₂) ₆ CH ₃	24272	823	1185	86	5
	CH ₃ (CH ₂) ₂ CH(CH ₂) ₃ CH ₃	47498	1688	2624	158	13
	Transition State	150061	5449	7877	289	22
OH-R20 (ONIOM)	CH ₃ (CH ₂) ₆ CH ₃	1213	61	297	46	28
	CH ₃ (CH ₂) ₂ CH(CH ₂) ₃ CH ₃	2497	135	601	80	54
	Transition State	11539	547	1523	190	101
HO ₂ -R13 (QCISD(T)/CBS)	CH ₃ (CH ₂) ₅ CH ₃	6719	228	821	43	5
	CH ₂ (CH ₂) ₅ CH ₃	25149	461	2010	77	11
	Transition State	89282	3405	5013	158	8
HO ₂ -R13 (ONIOM)	CH ₃ (CH ₂) ₅ CH ₃	89	13	65	18	8
	CH ₂ (CH ₂) ₅ CH ₃	122	23	95	26	19
	Transition State	3620	109	255	48	29
HO ₂ -R16 (QCISD(T)/CBS)	CH ₃ (CH ₂) ₅ CH ₃	6719	228	821	43	5
	CH ₃ (CH ₂) ₂ CH(CH ₂) ₂ CH ₃	15954	230	889	37	11
	Transition State	178951	3050	5893	180	9
HO ₂ -R16 (ONIOM)	CH ₃ (CH ₂) ₅ CH ₃	1122	47	264	32	13
	CH ₃ (CH ₂) ₂ CH(CH ₂) ₂ CH ₃	1579	68	184	26	73
	Transition State	20244	670	1523	112	52

Compared with [QCISD(T)/CBS]₂, we can clearly see that the computation cost is much reduced by using the ONIOM method, as shown in Table 3.4. All the calculations

are under the same setup (same amount of computation cores and memories). Different computing fabrics could influence the computation efficiency, so the compared results can be used as qualitative references.

Table 3.5 The comparison of EB from kinetic modelling and obtained by the ONIOM method for the hydrogen abstraction reactions of $n\text{-C}_n\text{H}_{2n+2} + \text{H}$, OH , and HO_2 ($n = 3\text{-}16$) (unit: kcal/mol).

Involved radical	Reaction sites	ONIOM	Reference
H	Primary sites (CH ₃ group)	9.78 to 10.11	7.70 ^a , 7.70 ^b , 8.61 ^c
	Other sites (CH ₂ group)	6.93 to 7.49	5.00 ^a , 5.00 ^b , 5.93 ^c
OH	Primary sites (CH ₃ group)	1.68 to 2.89	0.45 ^a , 1.81 ^b , 2.41 ^c
	Other sites (CH ₂ group)	-1.57 to 0.99	-0.76 ^a , 0.70 ^b , 1.19 ^c
HO ₂	Primary sites (CH ₃ group)	19.00 to 19.69	17.00 ^a , 19.41 ^b
	Other sites (CH ₂ group)	15.45 to 16.86	15.49 ^a , 17.02 ^b

^aEB from Battin-Leclerc et al. [79].

^bEB from Nehse et al. [80].

^cCalculated from Eq. (3.13).

3.4 Comparison with Literature Data

3.4.1 Comparison with Data from Kinetic Modelling

The practical kinetic modelling for large straight-chain alkanes molecules relies mainly on empirical and semi-empirical approaches to establish the thermochemical data in reaction mechanisms [79-82]. In these modellings, the hydrogen abstraction reactions of straight-chain alkanes by H, OH, and HO₂ were mainly classified into two types, the reactions occurring at primary sites (CH₃ groups) and other sites (CH₂ groups), and the EBs were considered as the constants for these two types. Owing to the different behaviors of CH₄ compared with other n -alkanes, it is the lack of C-C bond which exists in larger hydrocarbons, so it was considered separately. Compared with calculated data obtained by the ONIOM method, the EBs in these kinetic modellings

are generally underestimated for the reactions of $n\text{-C}_n\text{H}_{2n+2} + \text{H}$ and HO_2 , and for the reactions of $n\text{-C}_n\text{H}_{2n+2} + \text{OH}$, the EBs are within the range of the data by using the ONIOM method, as shown in Table 3.5.

Cohen [68, 69, 83] used the Evans-Polanyi principle [84] to calculate the activation energies by:

$$E_{act} = \alpha(BDE_{C-H} - \beta) \quad (3.13)$$

where BDE is bond dissociation energy. The BDEs were derived from experimental data using the principle of group additivity and the values of BDE are different for the hydrogen abstraction reaction occurring at different reaction sites. It was found that the BDEs vary for different molecules, for example $BDE(\text{CH}_4) = 105.1$ kcal/mol, $BDE(\text{C}_2\text{H}_6) = 100.6$ kcal/mol. For the molecule larger than C_2H_6 , $BDE(\text{CH}_3 \text{ groups}) = 100.5$ kcal/mol, and $BDE(\text{CH}_2 \text{ groups}) = 97.1$ kcal/mol [68].

In the study of $\text{H} + \text{alkane}$ reactions [68], the values of α and β are 0.79 and 89.6 kcal/mol, respectively. The calculated energies $n\text{-C}_n\text{H}_{2n+2} + \text{H}$ using Eq. (3.13) and the ONIOM energies have been compared in Table 3.5. We can see that the EBs calculated by Eq. (3.13) are constants for the reactions occurring at primary sites (CH_3 groups), $\text{EB} = 8.61$ kcal/mol, and other reaction sites (CH_2 groups), $\text{EB} = 5.93$ kcal/mol with the molecules larger than C_2H_6 . For the CH_4 and C_2H_6 , the EBs are 12.25 kcal/mol and 8.69 kcal/mol, respectively. In general, these EBs calculated by Eq. (3.13) are lower than the EBs calculated by using the ONIOM method.

In the study of $\text{OH} + \text{alkane}$ reactions [69], the values of α and β are 0.36 and

93.8 kcal/mol, respectively. The calculated energies of $n\text{-C}_n\text{H}_{2n+2} + \text{OH}$ using Eq. (3.13) and the ONOIM energies have been compared in Table 3.5. We can see that the EBs calculated by Eq. (3.13) are constants for the reactions occurring at primary sites (CH_3 groups), $\text{EB} = 2.41$ kcal/mol, and other reaction sites (CH_2 groups), $\text{EB} = 1.19$ kcal/mol with the molecules larger than C_2H_6 . For the CH_4 and C_2H_6 , the EBs are 4.07 kcal/mol and 2.45 kcal/mol, respectively. In general, these EBs calculated by Eq. (3.13) are lower than the EBs of $n\text{-C}_n\text{H}_{2n+2} + \text{OH}$ ($n = 1-2$) and higher than those of $n\text{-C}_n\text{H}_{2n+2} + \text{OH}$ ($n > 2$) calculated by using the ONIOM method.

Table 3.6 The calculated EB for the hydrogen abstraction reactions of $n\text{-C}_n\text{H}_{2n+2} + \text{H}$ ($n = 1-4$ and 18) (unit: kcal/mol).

Reactions	ONIOM	Reference
H-R1: $\text{H} + \text{CH}_4 \rightarrow \text{H}_2 + \text{CH}_3$	13.34	13.3 ^a
H-R2: $\text{H} + \text{CH}_3\text{CH}_3 \rightarrow \text{H}_2 + \text{CH}_2\text{CH}_3$	10.17	10.30 ^b
H-R3: $\text{H} + \text{CH}_3\text{CH}_2\text{CH}_3 \rightarrow \text{H}_2 + \text{CH}_2\text{CH}_2\text{CH}_3$	10.11	10.27 ^b
H-R4: $\text{H} + \text{CH}_3\text{CH}_2\text{CH}_3 \rightarrow \text{H}_2 + \text{CH}_3\text{CHCH}_3$	7.49	7.68 ^b
H-R5: $\text{H} + \text{CH}_3(\text{CH}_2)_2\text{CH}_3 \rightarrow \text{H}_2 + \text{CH}_2(\text{CH}_2)_2\text{CH}_3$	10.01	10.07 ^c
H-R6: $\text{H} + \text{CH}_3(\text{CH}_2)_2\text{CH}_3 \rightarrow \text{H}_2 + \text{CH}_3\text{CHCH}_2\text{CH}_3$	7.39	7.21 ^c
H-R82: $\text{H} + \text{CH}_3(\text{CH}_2)_{16}\text{CH}_3 \rightarrow \text{H}_2 + \text{CH}_2(\text{CH}_2)_{16}\text{CH}_3$	9.84	10.85 ^d
H-R83: $\text{H} + \text{CH}_3(\text{CH}_2)_{16}\text{CH}_3 \rightarrow \text{H}_2 + \text{CH}_3\text{CH}(\text{CH}_2)_{15}\text{CH}_3$	7.21	7.82 ^d
H-R84 ~ H-R90	6.91~7.10	7.7~7.8 ^d

^aEspinosa-Garcia [70] at the CCSD(T)/cc-pVTZ//MP2(full)/6-31G(d,p) level.

^bSivaramakrishnan et al. [26] at the CCSD(T)/aug-cc-pV ∞ Z//MP2/6-311++G(d,p) level.

^cPeukert et al. [25] at the CCSD(T)/cc-pV ∞ Z//M06-2X/cc-pVTZ level.

^dChi and You [85] at the M06-2X/6-311++G(d,p) level.

3.4.2 Comparison with Data from Ab Initio Calculations

There are a few studies for the reactions of $n\text{-C}_n\text{H}_{2n+2}$ molecules by H, OH, and HO₂ radicals by using high-level methods, mainly focused on the smaller molecules.

For the reactions of $n\text{-C}_n\text{H}_{2n+2} + \text{H}$, Espinosa-Garcia [70] calculated the reaction of CH_4 with H radical at the CCSD(T)/cc-pVTZ//MP2(full)/6-31G(d,p) level with scaling

all the correlation energy (SAC) method [86]. Sivaramakrishnan et al. [26] calculated the reaction systems of C_2H_6 and C_3H_8 with H radical at the CCSD(T)/aug-cc-pV ∞ Z//MP2/6-311++G(d,p) level. Peukert et al. [25] calculated the reaction system of $n-C_4H_{10} + H$ at the CCSD(T)/cc-pV ∞ Z//M06-2X/cc-pVTZ level. It is seen that the present calculated results obtained by using the ONIOM method are in good agreement with the results calculated by these high-level theoretical calculations, the differences generally less than 0.2 kcal/mol, as shown in Table 3.6.

For the larger $n-C_nH_{2n+2} + H$ reaction systems, Chi and You [85] investigated the reactions of $n-C_{18}H_{38} + H$ using M06-2X/6-311++G(d,p) and obtained a qualitative conclusion that the reaction occurring at CH_3 group (H-82 as shown in Table 3.6) has the highest EB is 10.85 kcal/mol and the EB of the reactions occurring at the other positions range from 7.7 to 7.8 kcal/mol, and the comparison of calculated results with ONIOM method is as also shown in Table 3.6. Their results for EBs are higher than the ONIOM results by 0.6 to 0.8 kcal/mol, except for the reaction occurring at the reaction site of No. 1, where the difference is 1.01 kcal/mol higher, as also shown in Table 3.6.

Table 3.7 The calculated EB for the hydrogen abstraction reactions of $n-C_nH_{2n+2} + OH$ ($n = 5$) (unit: kcal/mol).

Reactions	ONIOM	Reference
OH-R7: $OH + CH_3(CH_2)_3CH_3 \rightarrow H_2O + CH_2(CH_2)_3CH_3$	1.98	1.987 ^a
OH-R8: $OH + CH_3(CH_2)_3CH_3 \rightarrow H_2O + CH_3CH(CH_2)_2CH_3$	-0.27	0.84 ^a
OH-R9: $OH + CH_3(CH_2)_3CH_3 \rightarrow H_2O + CH_3CH_2CHCH_2CH_3$	-0.13	0.40 ^a

^aSivaramakrishnan and Michael [28] at the at G3//B3LYP level.

For the reaction systems of $n-C_nH_{2n+2} + OH$, Sivaramakrishnan and Michael [28] studied the reactions of $n-C_5H_{12}$ at the G3//B3LYP level. It is seen that the ONIOM and

G3//B3LYP methods predict identical EB for the hydrogen abstraction reaction from the CH₃ group, and their predictions of EBs for the hydrogen abstraction reactions from the CH₂ groups are significantly higher than our results, as shown in Table 3.7. This is probably because the G3//B3LYP method tends to predict a tighter transition state structure and leads to a higher energy barrier. From Seal et al.'s study [39] for the hydrogen abstraction reactions of 1-butanol, labeled as H₃C⁽¹⁾-H₂C⁽²⁾-H₂C⁽³⁾-H₂C⁽⁴⁾-OH, by OH radical at the CCSD(T)/F12a/jun-cc-pVTZ//M08-HX/MG3S level, the EBs are 0.39 (1.98 for OH-R7), -0.82 (-0.27 for OH-R8), -0.50 (-0.13 for OH-R9) and -0.27 kcal/mol, respectively, for the reactions occurring from C1 to C4. The comparison results show that the values of EBs using the ONIOM method are reliable and that the differences are influenced by the different geometry optimization methods.

Table 3.8 The calculated EB for the hydrogen abstraction reactions of n -C_nH_{2n+2} + HO₂ ($n = 5$) (unit: kcal/mol).

Reactions	ONIOM	Reference
HO ₂ -R1: HO ₂ + CH ₄ → H ₂ O ₂ + CH ₃	24.11	24.00 ^a
HO ₂ -R2: HO ₂ + CH ₃ CH ₃ → H ₂ O ₂ + CH ₂ CH ₃	19.90	19.50 ^a
HO ₂ -R3: HO ₂ + CH ₃ CH ₂ CH ₃ → H ₂ O ₂ + CH ₂ CH ₂ CH ₃	19.40	19.60 ^a
HO ₂ -R4: HO ₂ + CH ₃ CH ₂ CH ₃ → H ₂ O ₂ + CH ₃ CHCH ₃	16.86	16.09 ^a
HO ₂ -R5: HO ₂ + CH ₃ (CH ₂) ₂ CH ₃ → H ₂ O ₂ + CH ₂ (CH ₂) ₂ CH ₃	19.31	19.46 ^a
HO ₂ -R6: HO ₂ + CH ₃ (CH ₂) ₂ CH ₃ → H ₂ O ₂ + CH ₃ CHCH ₂ CH ₃	16.37	15.39 ^a

^aEB from Aquilera et al. [29] at the at CCSD(T)/cc-pVTZ//B3LYP/def2-TZVP level with optimization by scaling factor of 1.053

For the reaction systems of n -C_nH_{2n+2} + HO₂, a few studies investigated the reaction system using high-level methods. Aquilera et al. [29] established an accurate benchmark for the hydrogen abstraction reaction reactions of n -C_nH_{2n+2} + HO₂ ($n = 2$ -4) at CCSD(T)/cc-pVTZ//B3LYP/def2-TZVP level. and we compared their data with the present ONIOM results in Table 3.8. It is seen that the differences of EBs for the

hydrogen abstraction reactions occurring at CH₃ groups are less than 0.4 kcal/mol. The exceptional cases are the reaction occurring at CH₂ group of C₃H₈ and C₄H₁₀, where the differences of EBs are 0.77 kcal/mol and 0.98 kcal/mol, respectively.

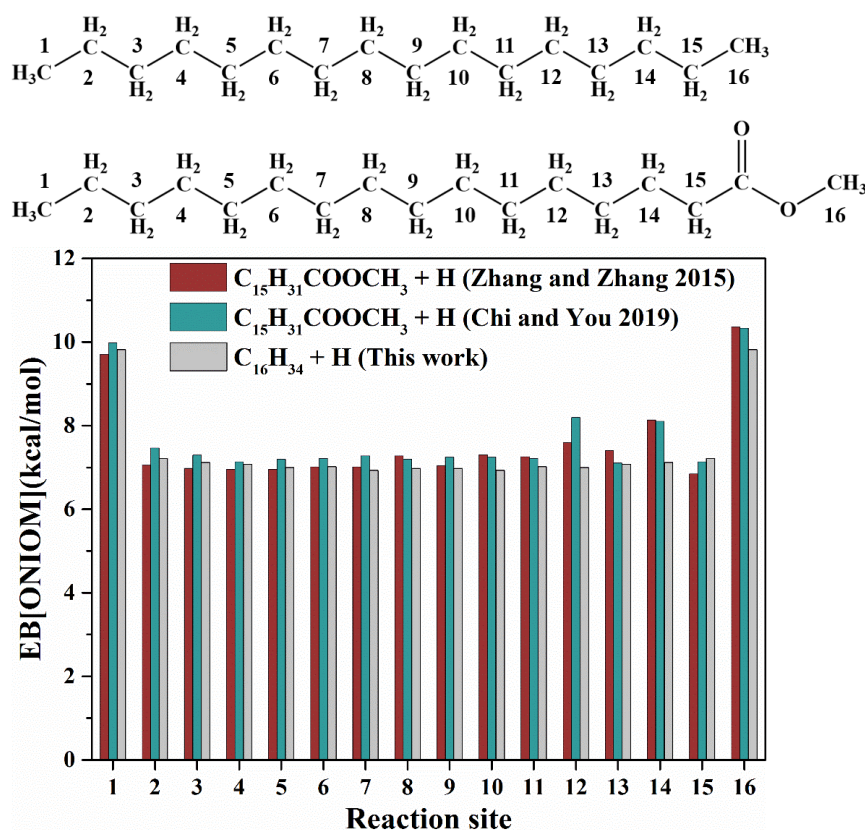


Figure 3.8 The EBs for the hydrogen abstraction reactions of C₁₅H₃₁COOCH₃ + H and *n*-C₁₆H₃₄ + H.

3.4.3 Comparison with Saturated and Unsaturated Methyl Ester

For saturated methyl esters, Zhang and Zhang [35] and Chi and You [85] studied the reactions of C₁₅H₃₁COOCH₃ + H by using ONIOM[QCISD(T)/CBS:DFT] and GEBF[CCSD(T)-F12a/cc-pVTZ] methods, respectively. It is seen in Figure 3.8 that the predicted EBs for C₁₅H₃₁COOCH₃ + H are quite close in all reaction sites except at No. 12, where the differences are 0.59 kcal/mol compared with Zhang and Zhang [35], and 1.19 kcal/mol compared with Chi and You [85]. In the present work, we compared the

similar reactions of $C_{15}H_{31}COOCH_3 + H$ and $n-C_{16}H_{34} + H$, because both molecules have similar structures, as shown in Figure 3.8.

As expected, a good agreement of the EBs at the reaction sites being sufficiently away from the ester group (namely, No.1-11 as shown in Figure 3.8) can be seen with differences generally being less than 0.3 kcal/mol. This can be understood by the fact that the influence of the ester group on the reaction decreases with moving away from its CAP and becomes non-negligible at the site of No. 12. The biggest difference between the two reactions occurs at the reaction occurring at the reaction site of No.14, up to 1.0 kcal/mol. This indicates that the hydrogen abstraction from No. 14 site is strongly affected by the different functional groups.

For unsaturated methyl esters, Zhang et al. [67] used the ONIOM[QCISD(T)/CBS:DFT] method to study the hydrogen abstraction reactions between unsaturated methyl esters and H radical. We compared the hydrogen abstraction reactions of $C_{17}H_{33}COOCH_3$ and $n-C_{18}H_{38}$, whose structures are shown in Figure 3.9. It is seen that the EB for $C_{17}H_{33}COOCH_3 + H$ and $n-C_{18}H_{38} + H$ at the reaction sites of No.1-6 is generally no more than 0.4 kcal/mol. The differences significantly increase with the reactions occurring at the reaction sites (No.8-11) around the C=C double bond with the largest difference of 4.6 kcal/mol at the reaction site of No.9 and No.10; the differences of EBs reduce to 2.12 kcal/mol at the site of No. 8 and 2.24 kcal/mol at the site of No. 11; the differences of EBs are 0.51 kcal/mol and 0.78 kcal/mol at the reaction sites of No.7 and No.12. When the reaction occurs at the site

which is away from the C=C double bond for more than 3 CH₂ groups, the differences of EBs will be reduced to less than 0.4 kcal/mol.

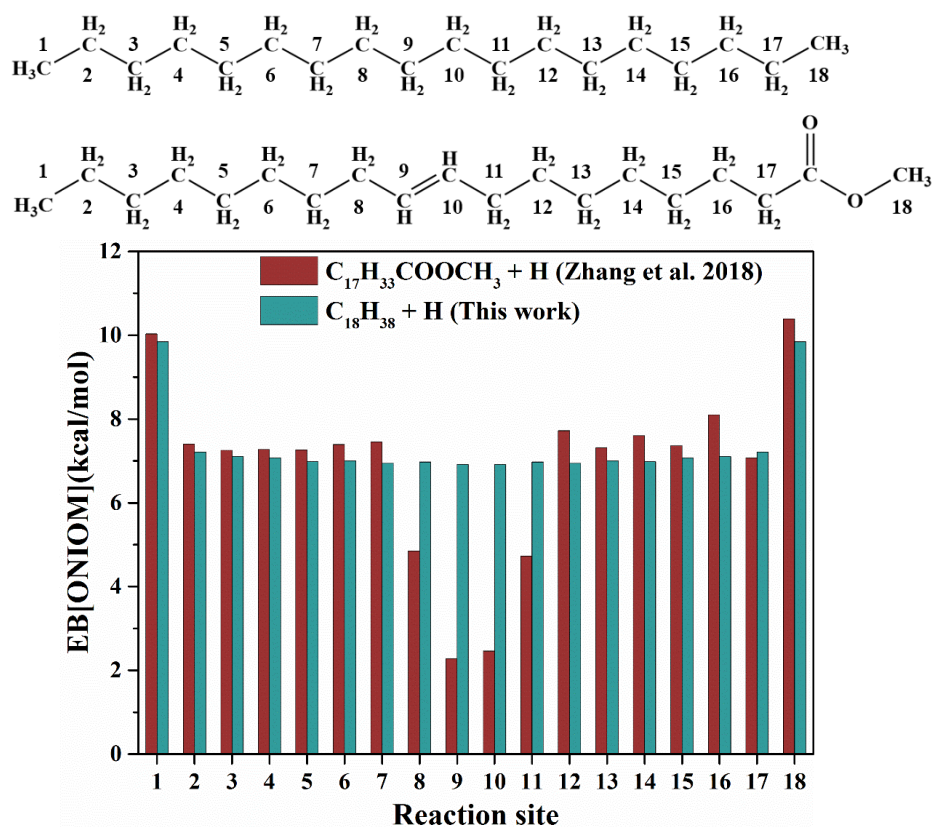


Figure 3.9 The EBs for the hydrogen abstraction reactions of $C_{17}H_{33}COOCH_3 + H$ and $n-C_{18}H_{38} + H$.

The agreement in EBs at the reaction sites away from the ester group with more than two carbon atoms is generally satisfactory and less than 0.6 kcal/mol, with the maximum difference of 1.0 kcal/mol for the reaction occurring at the reaction site of No.16. Therefore, it can be concluded that the ester group has a similar effect in saturated and unsaturated esters. In addition, the ester group has a weaker influence than the C=C double bond on the hydrogen abstraction reactions of larger molecules by hydrogen radical.

3.5 Concluding Remarks

An ONIOM[QCISD(T)/CBS:DFT] method was proposed and systematically validated in the present study for the hydrogen abstraction of straight-chain alkanes, n - C_nH_{2n+2} ($n= 1-16$), by H, OH, and HO_2 radicals. Two QCISD(T)/CBS methods were used to validate the ONIOM method. The comparison with the previous studies of large biodiesel molecules further substantiated the computational accuracy of the ONIOM method. Some important conclusions can be drawn from the work.

First, the computational uncertainty between two QCISD(T)/CBS methods is usually less than 0.20 kcal/mol. It again proved that the [QCISD(T)/CBS]₂ method through extrapolation from cc-pVDZ, cc-pVTZ to CBS with a second-order Møller–Plesset perturbation theory correction (MP2) is as accurate as the [QCISD(T)/CBS]₁ method.

Second, the chemically active portion CAP (2,2) is minimally and reasonably required for the present reaction system because it can predict the EB and HR for the studied reactions with satisfactory accuracy, with the difference compared with [QCISD(T)/CBS]₂ method being generally less than 0.10 kcal/mol.

Third, by comparison with the thermochemical data (EB) from kinetic modelling, we can find the EBs in the kinetic modelling usually are considered as constants, because the hydrogen abstraction reactions of n -alkanes can be classified into two types, namely the reactions occurring at primary sites (CH_3 groups) and other sites (CH_2 groups). The present results show that the classification is reasonable for the reactions

of $n\text{-C}_n\text{H}_{2n+2} + \text{H}$ (or HO_2). However, for the reactions of $n\text{-C}_n\text{H}_{2n+2} + \text{OH}$, the variation of EBs is obvious because the EBs are generally small (around 2.00 kcal/mol) for the reactions occurring at CH_3 groups, and smaller for the reaction occurring at CH_2 groups. Besides, compared with energy results obtained by the ONIOM method with kinetic modellings, the EBs in kinetic modellings are underestimated for the reactions of $n\text{-C}_n\text{H}_{2n+2} + \text{H}$ and HO_2 .

Finally, by comparing large straight-chain alkanes, $n\text{-C}_{16}\text{H}_{34}$, and $n\text{-C}_{18}\text{H}_{38}$ with large methyl ester molecules, $\text{C}_{15}\text{H}_{31}\text{COOCH}_3$ and $\text{C}_{17}\text{H}_{33}\text{COOCH}_3$, we found that the influence of the function group (ester group and $\text{C}=\text{C}$ double bond) becomes negligible at the reaction site away from the function group for more than two non-hydrogen atoms, where the thermochemistry of the methyl ester molecules is similar to that of straight-chain alkanes. In addition, the $\text{C}=\text{C}$ double bond has a greater influence on the neighbor atoms than the ester group for the hydrogen abstraction reactions by hydrogen radical.

Overall, the present study provides a practically useful theoretical methodology and thermochemical data for high-level chemical kinetics calculation of the large straight-chain hydrocarbon molecules.

3.6 Appendix

Table S3.1 The comparison of calculated results (EB and HR) for the hydrogen abstraction reactions of $n\text{-C}_n\text{H}_{2n+2} + \text{H}$ ($n = 1\text{-}9$) using the [QCISD(T)/CBS]₂ and ONIOM methods (unit: kcal/mol)

Reactions	EB			HR		
	[QCISD(T)/CBS] ₂	ONIOM	Difference	[QCISD(T)/CBS] ₂	ONIOM	Difference
H-R1: $\text{H} + \text{CH}_4 \rightarrow \text{H}_2 + \text{CH}_3$	13.34	13.34	0.00	-0.30	-0.30	0.00
H-R2: $\text{H} + \text{CH}_3\text{CH}_3 \rightarrow \text{H}_2 + \text{CH}_2\text{CH}_3$	10.17	10.17	0.00	-4.05	-4.05	0.00
H-R3: $\text{H} + \text{CH}_3\text{CH}_2\text{CH}_3 \rightarrow \text{H}_2 + \text{CH}_2\text{CH}_2\text{CH}_3$	10.11	10.11	0.00	-3.66	-3.66	0.00
H-R4: $\text{H} + \text{CH}_3\text{CH}_2\text{CH}_3 \rightarrow \text{H}_2 + \text{CH}_3\text{CHCH}_3$	7.49	7.49	0.00	-6.74	-6.74	0.00
H-R5: $\text{H} + \text{CH}_3(\text{CH}_2)_2\text{CH}_3 \rightarrow \text{H}_2 + \text{CH}_2(\text{CH}_2)_2\text{CH}_3$	10.01	10.05	0.04	-3.73	-3.72	0.01
H-R6: $\text{H} + \text{CH}_3(\text{CH}_2)_2\text{CH}_3 \rightarrow \text{H}_2 + \text{CH}_3\text{CHCH}_2\text{CH}_3$	7.39	7.39	0.00	-6.45	-6.45	0.00
H-R7: $\text{H} + \text{CH}_3(\text{CH}_2)_3\text{CH}_3 \rightarrow \text{H}_2 + \text{CH}_2(\text{CH}_2)_3\text{CH}_3$	9.95	10.00	0.05	-3.69	-3.69	0.00
H-R8: $\text{H} + \text{CH}_3(\text{CH}_2)_3\text{CH}_3 \rightarrow \text{H}_2 + \text{CH}_3\text{CH}(\text{CH}_2)_2\text{CH}_3$	7.38	7.42	0.04	-6.45	-6.45	0.00
H-R9: $\text{H} + \text{CH}_3(\text{CH}_2)_3\text{CH}_3 \rightarrow \text{H}_2 + \text{CH}_3\text{CH}_2\text{CHCH}_2\text{CH}_3$	7.38	7.38	0.00	-6.13	-6.13	0.00
H-R10: $\text{H} + \text{CH}_3(\text{CH}_2)_4\text{CH}_3 \rightarrow \text{H}_2 + \text{CH}_2(\text{CH}_2)_4\text{CH}_3$	9.91	9.98	0.07	-3.72	-3.72	0.00
H-R11: $\text{H} + \text{CH}_3(\text{CH}_2)_4\text{CH}_3 \rightarrow \text{H}_2 + \text{CH}_3\text{CH}(\text{CH}_2)_3\text{CH}_3$	7.39	7.44	0.05	-6.49	-6.49	0.00
H-R12: $\text{H} + \text{CH}_3(\text{CH}_2)_4\text{CH}_3 \rightarrow \text{H}_2 + \text{CH}_3\text{CH}_2\text{CH}(\text{CH}_2)_2\text{CH}_3$	7.28	7.32	0.04	-6.19	-6.19	0.00
H-R13: $\text{H} + \text{CH}_3(\text{CH}_2)_5\text{CH}_3 \rightarrow \text{H}_2 + \text{CH}_2(\text{CH}_2)_5\text{CH}_3$	9.92	9.99	0.07	-3.71	-3.70	0.01
H-R14: $\text{H} + \text{CH}_3(\text{CH}_2)_5\text{CH}_3 \rightarrow \text{H}_2 + \text{CH}_3\text{CH}(\text{CH}_2)_4\text{CH}_3$	7.33	7.38	0.05	-6.47	-6.47	0.00
H-R15: $\text{H} + \text{CH}_3(\text{CH}_2)_5\text{CH}_3 \rightarrow \text{H}_2 + \text{CH}_3\text{CH}_2\text{CH}(\text{CH}_2)_3\text{CH}_3$	7.22	7.28	0.06	-6.17	-6.18	0.01
H-R16: $\text{H} + \text{CH}_3(\text{CH}_2)_5\text{CH}_3 \rightarrow \text{H}_2 + \text{CH}_3(\text{CH}_2)_2\text{CH}(\text{CH}_2)_2\text{CH}_3$	7.23	7.30	0.07	-6.21	-6.21	0.00
H-R17: $\text{H} + \text{CH}_3(\text{CH}_2)_6\text{CH}_3 \rightarrow \text{H}_2 + \text{CH}_2(\text{CH}_2)_6\text{CH}_3$	9.86	9.94	0.08	-3.71	-3.71	0.00
H-R18: $\text{H} + \text{CH}_3(\text{CH}_2)_6\text{CH}_3 \rightarrow \text{H}_2 + \text{CH}_3\text{CH}(\text{CH}_2)_5\text{CH}_3$	7.28	7.34	0.06	-6.48	-6.48	0.00
H-R19: $\text{H} + \text{CH}_3(\text{CH}_2)_6\text{CH}_3 \rightarrow \text{H}_2 + \text{CH}_3\text{CH}_2\text{CH}(\text{CH}_2)_4\text{CH}_3$	7.15	7.21	0.06	-6.17	-6.18	0.01
H-R20: $\text{H} + \text{CH}_3(\text{CH}_2)_6\text{CH}_3 \rightarrow \text{H}_2 + \text{CH}_3(\text{CH}_2)_2\text{CH}(\text{CH}_2)_3\text{CH}_3$	7.13	7.22	0.09	-6.24	-6.24	0.00
H-R21: $\text{H} + \text{CH}_3(\text{CH}_2)_7\text{CH}_3 \rightarrow \text{H}_2 + \text{CH}_2(\text{CH}_2)_7\text{CH}_3$	9.77	9.86	0.09	-3.70	-3.70	0.00
H-R22: $\text{H} + \text{CH}_3(\text{CH}_2)_7\text{CH}_3 \rightarrow \text{H}_2 + \text{CH}_3\text{CH}(\text{CH}_2)_6\text{CH}_3$	7.13	7.20	0.07	-6.46	-6.47	0.01
H-R23: $\text{H} + \text{CH}_3(\text{CH}_2)_7\text{CH}_3 \rightarrow \text{H}_2 + \text{CH}_3\text{CH}_2\text{CH}(\text{CH}_2)_5\text{CH}_3$	7.02	7.09	0.07	-6.17	-6.18	0.01
H-R24: $\text{H} + \text{CH}_3(\text{CH}_2)_7\text{CH}_3 \rightarrow \text{H}_2 + \text{CH}_3(\text{CH}_2)_2\text{CH}(\text{CH}_2)_4\text{CH}_3$	7.01	7.10	0.09	-6.23	-6.25	0.02
H-R25: $\text{H} + \text{CH}_3(\text{CH}_2)_7\text{CH}_3 \rightarrow \text{H}_2 + \text{CH}_3(\text{CH}_2)_3\text{CH}(\text{CH}_2)_3\text{CH}_3$	6.92	7.04	0.12	-6.20	-6.22	0.02

Table S3.2 The calculated results (EB and HR) for the hydrogen abstraction reactions of n -C_nH_{2n+2} + H (n = 10-16) using ONIOM method (unit: kcal/mol).

Reactions	EB	HR
H-R26: H + CH ₃ (CH ₂) ₈ CH ₃ → H ₂ + CH ₂ (CH ₂) ₈ CH ₃	9.82	-3.70
H-R27: H + CH ₃ (CH ₂) ₈ CH ₃ → H ₂ + CH ₃ CH(CH ₂) ₇ CH ₃	7.15	-6.47
H-R28: H + CH ₃ (CH ₂) ₈ CH ₃ → H ₂ + CH ₃ CH ₂ CH(CH ₂) ₆ CH ₃	7.05	-6.19
H-R29: H + CH ₃ (CH ₂) ₈ CH ₃ → H ₂ + CH ₃ (CH ₂) ₂ CH(CH ₂) ₅ CH ₃	7.04	-6.25
H-R30: H + CH ₃ (CH ₂) ₈ CH ₃ → H ₂ + CH ₃ (CH ₂) ₃ CH(CH ₂) ₄ CH ₃	7.02	-6.27
H-R31: H + CH ₃ (CH ₂) ₉ CH ₃ → H ₂ + CH ₂ (CH ₂) ₉ CH ₃	9.78	-3.71
H-R32: H + CH ₃ (CH ₂) ₉ CH ₃ → H ₂ + CH ₃ CH(CH ₂) ₈ CH ₃	7.12	-6.47
H-R33: H + CH ₃ (CH ₂) ₉ CH ₃ → H ₂ + CH ₃ CH ₂ CH(CH ₂) ₇ CH ₃	7.06	-6.19
H-R34: H + CH ₃ (CH ₂) ₉ CH ₃ → H ₂ + CH ₃ (CH ₂) ₂ CH(CH ₂) ₆ CH ₃	6.96	-6.26
H-R35: H + CH ₃ (CH ₂) ₉ CH ₃ → H ₂ + CH ₃ (CH ₂) ₃ CH(CH ₂) ₅ CH ₃	6.99	-6.25
H-R36: H + CH ₃ (CH ₂) ₉ CH ₃ → H ₂ + CH ₃ (CH ₂) ₄ CH(CH ₂) ₄ CH ₃	6.98	-6.32
H-R37: H + CH ₃ (CH ₂) ₁₀ CH ₃ → H ₂ + CH ₂ (CH ₂) ₁₀ CH ₃	9.79	-3.70
H-R38: H + CH ₃ (CH ₂) ₁₀ CH ₃ → H ₂ + CH ₃ CH(CH ₂) ₉ CH ₃	7.13	-6.46
H-R39: H + CH ₃ (CH ₂) ₁₀ CH ₃ → H ₂ + CH ₃ CH ₂ CH(CH ₂) ₈ CH ₃	7.11	-6.19
H-R40: H + CH ₃ (CH ₂) ₁₀ CH ₃ → H ₂ + CH ₃ (CH ₂) ₂ CH(CH ₂) ₇ CH ₃	7.05	-6.25
H-R41: H + CH ₃ (CH ₂) ₁₀ CH ₃ → H ₂ + CH ₃ (CH ₂) ₃ CH(CH ₂) ₆ CH ₃	7.05	-6.28
H-R42: H + CH ₃ (CH ₂) ₁₀ CH ₃ → H ₂ + CH ₃ (CH ₂) ₄ CH(CH ₂) ₅ CH ₃	7.01	-6.29
H-R43: H + CH ₃ (CH ₂) ₁₁ CH ₃ → H ₂ + CH ₂ (CH ₂) ₁₁ CH ₃	9.79	-3.72
H-R44: H + CH ₃ (CH ₂) ₁₁ CH ₃ → H ₂ + CH ₃ CH(CH ₂) ₁₀ CH ₃	7.16	-6.49
H-R45: H + CH ₃ (CH ₂) ₁₁ CH ₃ → H ₂ + CH ₃ CH ₂ CH(CH ₂) ₉ CH ₃	7.09	-6.21
H-R46: H + CH ₃ (CH ₂) ₁₁ CH ₃ → H ₂ + CH ₃ (CH ₂) ₂ CH(CH ₂) ₈ CH ₃	7.05	-6.28
H-R47: H + CH ₃ (CH ₂) ₁₁ CH ₃ → H ₂ + CH ₃ (CH ₂) ₃ CH(CH ₂) ₇ CH ₃	7.00	-6.26
H-R48: H + CH ₃ (CH ₂) ₁₁ CH ₃ → H ₂ + CH ₃ (CH ₂) ₄ CH(CH ₂) ₆ CH ₃	7.00	-6.37
H-R49: H + CH ₃ (CH ₂) ₁₁ CH ₃ → H ₂ + CH ₃ (CH ₂) ₅ CH(CH ₂) ₅ CH ₃	6.97	-6.18
H-R50: H + CH ₃ (CH ₂) ₁₂ CH ₃ → H ₂ + CH ₂ (CH ₂) ₁₂ CH ₃	9.81	-3.70
H-R51: H + CH ₃ (CH ₂) ₁₂ CH ₃ → H ₂ + CH ₃ CH(CH ₂) ₁₁ CH ₃	7.21	-6.46
H-R52: H + CH ₃ (CH ₂) ₁₂ CH ₃ → H ₂ + CH ₃ CH ₂ CH(CH ₂) ₁₀ CH ₃	7.12	-6.19
H-R53: H + CH ₃ (CH ₂) ₁₂ CH ₃ → H ₂ + CH ₃ (CH ₂) ₂ CH(CH ₂) ₉ CH ₃	7.08	-6.24
H-R54: H + CH ₃ (CH ₂) ₁₂ CH ₃ → H ₂ + CH ₃ (CH ₂) ₃ CH(CH ₂) ₈ CH ₃	7.05	-6.30
H-R55: H + CH ₃ (CH ₂) ₁₂ CH ₃ → H ₂ + CH ₃ (CH ₂) ₄ CH(CH ₂) ₇ CH ₃	7.03	-6.17
H-R56: H + CH ₃ (CH ₂) ₁₂ CH ₃ → H ₂ + CH ₃ (CH ₂) ₅ CH(CH ₂) ₆ CH ₃	6.98	-6.16
H-R57: H + CH ₃ (CH ₂) ₁₃ CH ₃ → H ₂ + CH ₂ (CH ₂) ₁₃ CH ₃	9.82	-3.71
H-R58: H + CH ₃ (CH ₂) ₁₃ CH ₃ → H ₂ + CH ₃ CH(CH ₂) ₁₂ CH ₃	7.19	-6.46
H-R59: H + CH ₃ (CH ₂) ₁₃ CH ₃ → H ₂ + CH ₃ CH ₂ CH(CH ₂) ₁₁ CH ₃	7.11	-6.19
H-R60: H + CH ₃ (CH ₂) ₁₃ CH ₃ → H ₂ + CH ₃ (CH ₂) ₂ CH(CH ₂) ₁₀ CH ₃	7.08	-6.24
H-R61: H + CH ₃ (CH ₂) ₁₃ CH ₃ → H ₂ + CH ₃ (CH ₂) ₃ CH(CH ₂) ₉ CH ₃	7.01	-6.34
H-R62: H + CH ₃ (CH ₂) ₁₃ CH ₃ → H ₂ + CH ₃ (CH ₂) ₄ CH(CH ₂) ₈ CH ₃	7.01	-6.33
H-R63: H + CH ₃ (CH ₂) ₁₃ CH ₃ → H ₂ + CH ₃ (CH ₂) ₅ CH(CH ₂) ₇ CH ₃	6.95	-6.34
H-R64: H + CH ₃ (CH ₂) ₁₃ CH ₃ → H ₂ + CH ₃ (CH ₂) ₆ CH(CH ₂) ₆ CH ₃	6.93	-6.26

H-R65: $\text{H} + \text{CH}_3(\text{CH}_2)_{14}\text{CH}_3 \rightarrow \text{H}_2 + \text{CH}_2(\text{CH}_2)_{14}\text{CH}_3$	9.82	-3.70
H-R66: $\text{H} + \text{CH}_3(\text{CH}_2)_{14}\text{CH}_3 \rightarrow \text{H}_2 + \text{CH}_3\text{CH}(\text{CH}_2)_{13}\text{CH}_3$	7.21	-6.46
H-R67: $\text{H} + \text{CH}_3(\text{CH}_2)_{14}\text{CH}_3 \rightarrow \text{H}_2 + \text{CH}_3\text{CH}_2\text{CH}(\text{CH}_2)_{12}\text{CH}_3$	7.12	-6.19
H-R68: $\text{H} + \text{CH}_3(\text{CH}_2)_{14}\text{CH}_3 \rightarrow \text{H}_2 + \text{CH}_3(\text{CH}_2)_2\text{CH}(\text{CH}_2)_{11}\text{CH}_3$	7.08	-6.24
H-R69: $\text{H} + \text{CH}_3(\text{CH}_2)_{14}\text{CH}_3 \rightarrow \text{H}_2 + \text{CH}_3(\text{CH}_2)_3\text{CH}(\text{CH}_2)_{10}\text{CH}_3$	7.00	-6.40
H-R70: $\text{H} + \text{CH}_3(\text{CH}_2)_{14}\text{CH}_3 \rightarrow \text{H}_2 + \text{CH}_3(\text{CH}_2)_4\text{CH}(\text{CH}_2)_9\text{CH}_3$	7.02	-6.27
H-R71: $\text{H} + \text{CH}_3(\text{CH}_2)_{14}\text{CH}_3 \rightarrow \text{H}_2 + \text{CH}_3(\text{CH}_2)_5\text{CH}(\text{CH}_2)_8\text{CH}_3$	6.93	-6.33
H-R72: $\text{H} + \text{CH}_3(\text{CH}_2)_{14}\text{CH}_3 \rightarrow \text{H}_2 + \text{CH}_3(\text{CH}_2)_6\text{CH}(\text{CH}_2)_7\text{CH}_3$	6.98	-6.34

Table S3.3 The comparison of calculated results (EB and HR) for the hydrogen abstraction reactions of $n\text{-C}_n\text{H}_{2n+2} + \text{OH}$ ($n = 1\text{-}8$) using the [QCISD(T)/CBS]₂ and ONIOM (unit: kcal/mol).

Reactions	EB			HR		
	[QCISD(T)/CBS] ₂	ONIOM	Difference	[QCISD(T)/CBS] ₂	ONIOM	Difference
OH-R1: OH + CH ₄ → H ₂ O + CH ₃	5.02	5.02	0.00	-14.97	-14.97	0.00
OH-R2: OH + CH ₃ CH ₃ → H ₂ O + CH ₂ CH ₃	2.63	2.63	0.00	-18.48	-18.48	0.00
OH-R3: OH + CH ₃ CH ₂ CH ₃ → H ₂ O + CH ₂ CH ₂ CH ₃	1.81	1.81	0.00	-18.46	-18.46	0.00
OH-R4: OH + CH ₃ CH ₂ CH ₃ → H ₂ O + CH ₃ CHCH ₃	0.49	0.49	0.00	-21.47	-21.47	0.00
OH-R5: OH + CH ₃ (CH ₂) ₂ CH ₃ → H ₂ O + CH ₂ (CH ₂) ₂ CH ₃	2.88	2.89	0.01	-17.36	-17.39	0.03
OH-R6: OH + CH ₃ (CH ₂) ₂ CH ₃ → H ₂ O + CH ₃ CHCH ₂ CH ₃	0.99	0.99	0.00	-20.27	-20.27	0.00
OH-R7: OH + CH ₃ (CH ₂) ₃ CH ₃ → H ₂ O + CH ₂ (CH ₂) ₃ CH ₃	1.95	1.98	0.03	-18.59	-18.59	0.00
OH-R8: OH + CH ₃ (CH ₂) ₃ CH ₃ → H ₂ O + CH ₃ CH(CH ₂) ₂ CH ₃	-0.29	-0.27	0.02	-21.29	-21.30	0.01
OH-R9: OH + CH ₃ (CH ₂) ₃ CH ₃ → H ₂ O + CH ₃ CH ₂ CHCH ₂ CH ₃	-0.13	-0.13	0.00	-20.93	-20.93	0.00
OH-R10: OH + CH ₃ (CH ₂) ₄ CH ₃ → H ₂ O + CH ₂ (CH ₂) ₄ CH ₃	1.92	1.95	0.03	-18.12	-18.13	0.01
OH-R11: OH + CH ₃ (CH ₂) ₄ CH ₃ → H ₂ O + CH ₃ CH(CH ₂) ₃ CH ₃	0.37	0.41	0.04	-20.81	-20.84	0.03
OH-R12: OH + CH ₃ (CH ₂) ₄ CH ₃ → H ₂ O + CH ₃ CH ₂ CH(CH ₂) ₂ CH ₃	0.26	0.28	0.02	-20.52	-20.54	0.02
OH-R13: OH + CH ₃ (CH ₂) ₅ CH ₃ → H ₂ O + CH ₂ (CH ₂) ₅ CH ₃	1.64	1.68	0.03	-18.55	-18.55	0.00
OH-R14: OH + CH ₃ (CH ₂) ₅ CH ₃ → H ₂ O + CH ₃ CH(CH ₂) ₄ CH ₃	-0.17	-0.13	0.04	-21.67	-21.68	0.01
OH-R15: OH + CH ₃ (CH ₂) ₅ CH ₃ → H ₂ O + CH ₃ CH ₂ CH(CH ₂) ₃ CH ₃	-0.79	-0.74	0.05	-20.94	-20.96	0.02
OH-R16: OH + CH ₃ (CH ₂) ₅ CH ₃ → H ₂ O + CH ₃ (CH ₂) ₂ CH(CH ₂) ₂ CH ₃	-0.94	-0.86	0.08	-21.40	-21.43	0.03
OH-R17: OH + CH ₃ (CH ₂) ₆ CH ₃ → H ₂ O + CH ₂ (CH ₂) ₆ CH ₃	2.29	2.31	0.02	-18.39	-18.40	0.01
OH-R18: OH + CH ₃ (CH ₂) ₆ CH ₃ → H ₂ O + CH ₃ CH(CH ₂) ₅ CH ₃	-0.14	-0.08	0.06	-21.14	-21.16	0.02
OH-R19: OH + CH ₃ (CH ₂) ₆ CH ₃ → H ₂ O + CH ₃ CH ₂ CH(CH ₂) ₄ CH ₃	-0.24	-0.20	0.04	-20.94	-20.97	0.03
OH-R20: OH + CH ₃ (CH ₂) ₆ CH ₃ → H ₂ O + CH ₃ (CH ₂) ₂ CH(CH ₂) ₃ CH ₃	-0.86	-0.76	0.10	-20.89	-20.93	0.04

Table S3.4 The calculated results (EB and HR) for the hydrogen abstraction reactions of n -C_nH_{2n+2} + OH (n = 9-16) using ONIOM method (unit: kcal/mol).

Reactions	EB	HR
OH-R21: OH + CH ₃ (CH ₂) ₇ CH ₃ → H ₂ O + CH ₂ (CH ₂) ₇ CH ₃	1.79	-18.52
OH-R22: OH + CH ₃ (CH ₂) ₇ CH ₃ → H ₂ O + CH ₃ CH(CH ₂) ₆ CH ₃	-0.32	-21.59
OH-R23: OH + CH ₃ (CH ₂) ₇ CH ₃ → H ₂ O + CH ₃ CH ₂ CH(CH ₂) ₅ CH ₃	-0.43	-20.91
OH-R24: OH + CH ₃ (CH ₂) ₇ CH ₃ → H ₂ O + CH ₃ (CH ₂) ₂ CH(CH ₂) ₄ CH ₃	-0.39	-21.12
OH-R25: OH + CH ₃ (CH ₂) ₇ CH ₃ → H ₂ O + CH ₃ (CH ₂) ₃ CH(CH ₂) ₃ CH ₃	-0.67	-21.00
OH-R26: OH + CH ₃ (CH ₂) ₈ CH ₃ → H ₂ O + CH ₂ (CH ₂) ₈ CH ₃	2.24	-18.46
OH-R27: OH + CH ₃ (CH ₂) ₈ CH ₃ → H ₂ O + CH ₃ CH(CH ₂) ₇ CH ₃	-0.50	-21.26
OH-R28: OH + CH ₃ (CH ₂) ₈ CH ₃ → H ₂ O + CH ₃ CH ₂ CH(CH ₂) ₆ CH ₃	-0.52	-21.06
OH-R29: OH + CH ₃ (CH ₂) ₈ CH ₃ → H ₂ O + CH ₃ (CH ₂) ₂ CH(CH ₂) ₅ CH ₃	-1.13	-20.85
OH-R30: OH + CH ₃ (CH ₂) ₈ CH ₃ → H ₂ O + CH ₃ (CH ₂) ₃ CH(CH ₂) ₄ CH ₃	-0.49	-21.12
OH-R31: OH + CH ₃ (CH ₂) ₉ CH ₃ → H ₂ O + CH ₂ (CH ₂) ₉ CH ₃	1.92	-18.50
OH-R32: OH + CH ₃ (CH ₂) ₉ CH ₃ → H ₂ O + CH ₃ CH(CH ₂) ₈ CH ₃	-0.52	-21.52
OH-R33: OH + CH ₃ (CH ₂) ₉ CH ₃ → H ₂ O + CH ₃ CH ₂ CH(CH ₂) ₇ CH ₃	-0.59	-20.85
OH-R34: OH + CH ₃ (CH ₂) ₉ CH ₃ → H ₂ O + CH ₃ (CH ₂) ₂ CH(CH ₂) ₆ CH ₃	-0.53	-21.31
OH-R35: OH + CH ₃ (CH ₂) ₉ CH ₃ → H ₂ O + CH ₃ (CH ₂) ₃ CH(CH ₂) ₅ CH ₃	-1.20	-21.38
OH-R36: OH + CH ₃ (CH ₂) ₉ CH ₃ → H ₂ O + CH ₃ (CH ₂) ₄ CH(CH ₂) ₄ CH ₃	-0.52	-21.47
OH-R37: OH + CH ₃ (CH ₂) ₁₀ CH ₃ → H ₂ O + CH ₂ (CH ₂) ₁₀ CH ₃	1.80	-18.47
OH-R38: OH + CH ₃ (CH ₂) ₁₀ CH ₃ → H ₂ O + CH ₃ CH(CH ₂) ₉ CH ₃	-0.78	-21.29
OH-R39: OH + CH ₃ (CH ₂) ₁₀ CH ₃ → H ₂ O + CH ₃ CH ₂ CH(CH ₂) ₈ CH ₃	-0.91	-20.92
OH-R40: OH + CH ₃ (CH ₂) ₁₀ CH ₃ → H ₂ O + CH ₃ (CH ₂) ₂ CH(CH ₂) ₇ CH ₃	-1.29	-20.84
OH-R41: OH + CH ₃ (CH ₂) ₁₀ CH ₃ → H ₂ O + CH ₃ (CH ₂) ₃ CH(CH ₂) ₆ CH ₃	-0.56	-21.27
OH-R42: OH + CH ₃ (CH ₂) ₁₀ CH ₃ → H ₂ O + CH ₃ (CH ₂) ₄ CH(CH ₂) ₅ CH ₃	-0.63	-21.20
OH-R43: OH + CH ₃ (CH ₂) ₁₁ CH ₃ → H ₂ O + CH ₂ (CH ₂) ₁₁ CH ₃	1.84	-18.48
OH-R44: OH + CH ₃ (CH ₂) ₁₁ CH ₃ → H ₂ O + CH ₃ CH(CH ₂) ₁₀ CH ₃	-0.73	-21.46
OH-R45: OH + CH ₃ (CH ₂) ₁₁ CH ₃ → H ₂ O + CH ₃ CH ₂ CH(CH ₂) ₉ CH ₃	-1.33	-20.83
OH-R46: OH + CH ₃ (CH ₂) ₁₁ CH ₃ → H ₂ O + CH ₃ (CH ₂) ₂ CH(CH ₂) ₈ CH ₃	-1.18	-21.04
OH-R47: OH + CH ₃ (CH ₂) ₁₁ CH ₃ → H ₂ O + CH ₃ (CH ₂) ₃ CH(CH ₂) ₇ CH ₃	-1.41	-21.49
OH-R48: OH + CH ₃ (CH ₂) ₁₁ CH ₃ → H ₂ O + CH ₃ (CH ₂) ₄ CH(CH ₂) ₆ CH ₃	-1.06	-21.36
OH-R49: OH + CH ₃ (CH ₂) ₁₁ CH ₃ → H ₂ O + CH ₃ (CH ₂) ₅ CH(CH ₂) ₅ CH ₃	-1.00	-21.48
OH-R50: OH + CH ₃ (CH ₂) ₁₂ CH ₃ → H ₂ O + CH ₂ (CH ₂) ₁₂ CH ₃	2.17	-18.47
OH-R51: OH + CH ₃ (CH ₂) ₁₂ CH ₃ → H ₂ O + CH ₃ CH(CH ₂) ₁₁ CH ₃	-1.06	-21.30
OH-R52: OH + CH ₃ (CH ₂) ₁₂ CH ₃ → H ₂ O + CH ₃ CH ₂ CH(CH ₂) ₁₀ CH ₃	-1.16	-20.87
OH-R53: OH + CH ₃ (CH ₂) ₁₂ CH ₃ → H ₂ O + CH ₃ (CH ₂) ₂ CH(CH ₂) ₉ CH ₃	-1.36	-20.91
OH-R54: OH + CH ₃ (CH ₂) ₁₂ CH ₃ → H ₂ O + CH ₃ (CH ₂) ₃ CH(CH ₂) ₈ CH ₃	-1.19	-21.43
OH-R55: OH + CH ₃ (CH ₂) ₁₂ CH ₃ → H ₂ O + CH ₃ (CH ₂) ₄ CH(CH ₂) ₇ CH ₃	-1.27	-21.25
OH-R56: OH + CH ₃ (CH ₂) ₁₂ CH ₃ → H ₂ O + CH ₃ (CH ₂) ₅ CH(CH ₂) ₆ CH ₃	-1.21	-21.48
OH-R57: OH + CH ₃ (CH ₂) ₁₃ CH ₃ → H ₂ O + CH ₂ (CH ₂) ₁₃ CH ₃	2.04	-18.47
OH-R58: OH + CH ₃ (CH ₂) ₁₃ CH ₃ → H ₂ O + CH ₃ CH(CH ₂) ₁₂ CH ₃	-0.98	-21.40
OH-R59: OH + CH ₃ (CH ₂) ₁₃ CH ₃ → H ₂ O + CH ₃ CH ₂ CH(CH ₂) ₁₁ CH ₃	-1.57	-20.82

OH-R60: $\text{OH} + \text{CH}_3(\text{CH}_2)_{13}\text{CH}_3 \rightarrow \text{H}_2\text{O} + \text{CH}_3(\text{CH}_2)_2\text{CH}(\text{CH}_2)_{10}\text{CH}_3$	-1.24	-20.94
OH-R61: $\text{OH} + \text{CH}_3(\text{CH}_2)_{13}\text{CH}_3 \rightarrow \text{H}_2\text{O} + \text{CH}_3(\text{CH}_2)_3\text{CH}(\text{CH}_2)_9\text{CH}_3$	-1.53	-21.60
OH-R62: $\text{OH} + \text{CH}_3(\text{CH}_2)_{13}\text{CH}_3 \rightarrow \text{H}_2\text{O} + \text{CH}_3(\text{CH}_2)_4\text{CH}(\text{CH}_2)_8\text{CH}_3$	-1.06	-21.59
OH-R63: $\text{OH} + \text{CH}_3(\text{CH}_2)_{13}\text{CH}_3 \rightarrow \text{H}_2\text{O} + \text{CH}_3(\text{CH}_2)_5\text{CH}(\text{CH}_2)_7\text{CH}_3$	-1.45	-21.57
OH-R64: $\text{OH} + \text{CH}_3(\text{CH}_2)_{13}\text{CH}_3 \rightarrow \text{H}_2\text{O} + \text{CH}_3(\text{CH}_2)_6\text{CH}(\text{CH}_2)_6\text{CH}_3$	-1.06	-21.57
OH-R65: $\text{OH} + \text{CH}_3(\text{CH}_2)_{14}\text{CH}_3 \rightarrow \text{H}_2\text{O} + \text{CH}_2(\text{CH}_2)_{14}\text{CH}_3$	2.17	-19.35
OH-R66: $\text{OH} + \text{CH}_3(\text{CH}_2)_{14}\text{CH}_3 \rightarrow \text{H}_2\text{O} + \text{CH}_3\text{CH}(\text{CH}_2)_{13}\text{CH}_3$	-0.96	-21.29
OH-R67: $\text{OH} + \text{CH}_3(\text{CH}_2)_{14}\text{CH}_3 \rightarrow \text{H}_2\text{O} + \text{CH}_3\text{CH}_2\text{CH}(\text{CH}_2)_{12}\text{CH}_3$	-1.40	-20.84
OH-R68: $\text{HO}_2 + \text{CH}_3(\text{CH}_2)_{14}\text{CH}_3 \rightarrow \text{H}_2\text{O}_2 + \text{CH}_3(\text{CH}_2)_2\text{CH}(\text{CH}_2)_{11}\text{CH}_3$	-1.48	-21.00
OH-R69: $\text{HO}_2 + \text{CH}_3(\text{CH}_2)_{14}\text{CH}_3 \rightarrow \text{H}_2\text{O}_2 + \text{CH}_3(\text{CH}_2)_3\text{CH}(\text{CH}_2)_{10}\text{CH}_3$	-1.31	-21.98
OH-R70: $\text{HO}_2 + \text{CH}_3(\text{CH}_2)_{14}\text{CH}_3 \rightarrow \text{H}_2\text{O}_2 + \text{CH}_3(\text{CH}_2)_4\text{CH}(\text{CH}_2)_9\text{CH}_3$	-1.26	-21.18
OH-R71: $\text{HO}_2 + \text{CH}_3(\text{CH}_2)_{14}\text{CH}_3 \rightarrow \text{H}_2\text{O}_2 + \text{CH}_3(\text{CH}_2)_5\text{CH}(\text{CH}_2)_8\text{CH}_3$	-1.24	-21.54
OH-R72: $\text{HO}_2 + \text{CH}_3(\text{CH}_2)_{14}\text{CH}_3 \rightarrow \text{H}_2\text{O}_2 + \text{CH}_3(\text{CH}_2)_6\text{CH}(\text{CH}_2)_7\text{CH}_3$	-1.31	-21.62

Table S3.5 The comparison of calculated results (EB and HR) for the hydrogen abstraction reactions of $n\text{-C}_n\text{H}_{2n+2} + \text{HO}_2$ ($n = 1\text{-}7$) using the [QCISD(T)/CBS]₂ and ONIOM (unit: kcal/mol).

Reactions	EB			HR		
	[QCISD(T)/CBS] ₂	ONIOM Difference		[QCISD(T)/CBS] ₂	ONIOM Difference	
HO ₂ -R1: HO ₂ + CH ₄ → H ₂ O ₂ + CH ₃	24.11	24.11	0.00	17.04	17.04	0.00
HO ₂ -R2: HO ₂ + CH ₃ CH ₃ → H ₂ O ₂ + CH ₂ CH ₃	19.90	19.90	0.00	13.29	13.29	0.00
HO ₂ -R3: HO ₂ + CH ₃ CH ₂ CH ₃ → H ₂ O ₂ + CH ₂ CH ₂ CH ₃	19.40	19.40	0.00	13.68	13.68	0.00
HO ₂ -R4: HO ₂ + CH ₃ CH ₂ CH ₃ → H ₂ O ₂ + CH ₃ CHCH ₃	16.86	16.86	0.00	10.60	10.60	0.00
HO ₂ -R5: HO ₂ + CH ₃ (CH ₂) ₂ CH ₃ → H ₂ O ₂ + CH ₂ (CH ₂) ₂ CH ₃	19.25	19.31	0.06	13.61	13.62	0.01
HO ₂ -R6: HO ₂ + CH ₃ (CH ₂) ₂ CH ₃ → H ₂ O ₂ + CH ₃ CHCH ₂ CH ₃	16.37	16.37	0.00	10.89	10.89	0.00
HO ₂ -R7: HO ₂ + CH ₃ (CH ₂) ₃ CH ₃ → H ₂ O ₂ + CH ₂ (CH ₂) ₃ CH ₃	19.58	19.64	0.06	13.65	13.65	0.00
HO ₂ -R8: HO ₂ + CH ₃ (CH ₂) ₃ CH ₃ → H ₂ O ₂ + CH ₃ CH(CH ₂) ₂ CH ₃	16.24	16.29	0.05	10.89	10.89	0.00
HO ₂ -R9: HO ₂ + CH ₃ (CH ₂) ₃ CH ₃ → H ₂ O ₂ + CH ₃ CH ₂ CHCH ₂ CH ₃	16.10	16.10	0.00	11.21	11.21	0.00
HO ₂ -R10: HO ₂ + CH ₃ (CH ₂) ₄ CH ₃ → H ₂ O ₂ + CH ₂ (CH ₂) ₄ CH ₃	19.52	19.58	0.06	13.62	13.62	0.00
HO ₂ -R11: HO ₂ + CH ₃ (CH ₂) ₄ CH ₃ → H ₂ O ₂ + CH ₃ CH(CH ₂) ₃ CH ₃	16.38	16.44	0.06	10.85	10.85	0.00
HO ₂ -R12: HO ₂ + CH ₃ (CH ₂) ₄ CH ₃ → H ₂ O ₂ + CH ₃ CH ₂ CH(CH ₂) ₂ CH ₃	15.99	16.05	0.06	11.15	11.15	0.00
HO ₂ -R13: HO ₂ + CH ₃ (CH ₂) ₅ CH ₃ → H ₂ O ₂ + CH ₂ (CH ₂) ₅ CH ₃	19.45	19.51	0.06	13.63	13.64	0.01
HO ₂ -R14: HO ₂ + CH ₃ (CH ₂) ₅ CH ₃ → H ₂ O ₂ + CH ₃ CH(CH ₂) ₄ CH ₃	16.16	16.22	0.06	10.87	10.87	0.00
HO ₂ -R15: HO ₂ + CH ₃ (CH ₂) ₅ CH ₃ → H ₂ O ₂ + CH ₃ CH ₂ CH(CH ₂) ₃ CH ₃	16.39	16.46	0.07	11.17	11.16	0.01
HO ₂ -R16: HO ₂ + CH ₃ (CH ₂) ₅ CH ₃ → H ₂ O ₂ + CH ₃ (CH ₂) ₂ CH(CH ₂) ₂ CH ₃	15.77	15.88	0.11	11.13	11.13	0.00

Table S3.6 The calculated results (EB and HR) for the hydrogen abstraction reactions of n -C_nH_{2n+2} + HO₂ (n = 8-16) using ONIOM method (unit: kcal/mol).

Reactions	EB	HR
HO ₂ -R17: HO ₂ + CH ₃ (CH ₂) ₆ CH ₃ → H ₂ O ₂ + CH ₂ (CH ₂) ₆ CH ₃	19.46	13.63
HO ₂ -R18: HO ₂ + CH ₃ (CH ₂) ₆ CH ₃ → H ₂ O ₂ + CH ₃ CH(CH ₂) ₅ CH ₃	16.52	10.86
HO ₂ -R19: HO ₂ + CH ₃ (CH ₂) ₆ CH ₃ → H ₂ O ₂ + CH ₃ CH ₂ CH(CH ₂) ₄ CH ₃	16.46	11.16
HO ₂ -R20: HO ₂ + CH ₃ (CH ₂) ₆ CH ₃ → H ₂ O ₂ + CH ₃ (CH ₂) ₂ CH(CH ₂) ₃ CH ₃	15.85	11.10
HO ₂ -R21: HO ₂ + CH ₃ (CH ₂) ₇ CH ₃ → H ₂ O ₂ + CH ₂ (CH ₂) ₇ CH ₃	19.45	13.63
HO ₂ -R22: HO ₂ + CH ₃ (CH ₂) ₇ CH ₃ → H ₂ O ₂ + CH ₃ CH(CH ₂) ₆ CH ₃	16.44	10.87
HO ₂ -R23: HO ₂ + CH ₃ (CH ₂) ₇ CH ₃ → H ₂ O ₂ + CH ₃ CH ₂ CH(CH ₂) ₅ CH ₃	16.26	11.16
HO ₂ -R24: HO ₂ + CH ₃ (CH ₂) ₇ CH ₃ → H ₂ O ₂ + CH ₃ (CH ₂) ₂ CH(CH ₂) ₄ CH ₃	15.92	11.09
HO ₂ -R25: HO ₂ + CH ₃ (CH ₂) ₇ CH ₃ → H ₂ O ₂ + CH ₃ (CH ₂) ₃ CH(CH ₂) ₃ CH ₃	15.74	11.12
HO ₂ -R26: HO ₂ + CH ₃ (CH ₂) ₈ CH ₃ → H ₂ O ₂ + CH ₂ (CH ₂) ₈ CH ₃	19.47	13.64
HO ₂ -R27: HO ₂ + CH ₃ (CH ₂) ₈ CH ₃ → H ₂ O ₂ + CH ₃ CH(CH ₂) ₇ CH ₃	16.20	10.87
HO ₂ -R28: HO ₂ + CH ₃ (CH ₂) ₈ CH ₃ → H ₂ O ₂ + CH ₃ CH ₂ CH(CH ₂) ₆ CH ₃	15.92	11.15
HO ₂ -R29: HO ₂ + CH ₃ (CH ₂) ₈ CH ₃ → H ₂ O ₂ + CH ₃ (CH ₂) ₂ CH(CH ₂) ₅ CH ₃	15.79	11.09
HO ₂ -R30: HO ₂ + CH ₃ (CH ₂) ₈ CH ₃ → H ₂ O ₂ + CH ₃ (CH ₂) ₃ CH(CH ₂) ₄ CH ₃	16.28	11.07
HO ₂ -R31: HO ₂ + CH ₃ (CH ₂) ₉ CH ₃ → H ₂ O ₂ + CH ₂ (CH ₂) ₉ CH ₃	19.55	13.63
HO ₂ -R32: HO ₂ + CH ₃ (CH ₂) ₉ CH ₃ → H ₂ O ₂ + CH ₃ CH(CH ₂) ₈ CH ₃	16.15	10.87
HO ₂ -R33: HO ₂ + CH ₃ (CH ₂) ₉ CH ₃ → H ₂ O ₂ + H ₂ +CH ₃ CH ₂ CH(CH ₂) ₇ CH ₃	16.28	11.15
HO ₂ -R34: HO ₂ + CH ₃ (CH ₂) ₉ CH ₃ → H ₂ O ₂ + CH ₃ (CH ₂) ₂ CH(CH ₂) ₆ CH ₃	15.78	11.08
HO ₂ -R35: HO ₂ + CH ₃ (CH ₂) ₉ CH ₃ → H ₂ O ₂ + CH ₃ (CH ₂) ₃ CH(CH ₂) ₅ CH ₃	16.20	11.09
HO ₂ -R36: HO ₂ + CH ₃ (CH ₂) ₉ CH ₃ → H ₂ O ₂ + CH ₃ (CH ₂) ₄ CH(CH ₂) ₄ CH ₃	15.74	11.02
HO ₂ -R37: HO ₂ + CH ₃ (CH ₂) ₁₀ CH ₃ → H ₂ O ₂ + CH ₂ (CH ₂) ₁₀ CH ₃	19.55	13.64
HO ₂ -R38: HO ₂ + CH ₃ (CH ₂) ₁₀ CH ₃ → H ₂ O ₂ + CH ₃ CH(CH ₂) ₉ CH ₃	16.58	10.88
HO ₂ -R39: HO ₂ + CH ₃ (CH ₂) ₁₀ CH ₃ → H ₂ O ₂ + H ₂ +CH ₃ CH ₂ CH(CH ₂) ₈ CH ₃	15.88	11.15
HO ₂ -R40: HO ₂ + CH ₃ (CH ₂) ₁₀ CH ₃ → H ₂ O ₂ + CH ₃ (CH ₂) ₂ CH(CH ₂) ₇ CH ₃	15.74	11.09
HO ₂ -R41: HO ₂ + CH ₃ (CH ₂) ₁₀ CH ₃ → H ₂ O ₂ + CH ₃ (CH ₂) ₃ CH(CH ₂) ₆ CH ₃	15.45	11.06
HO ₂ -R42: HO ₂ + CH ₃ (CH ₂) ₁₀ CH ₃ → H ₂ O ₂ + CH ₃ (CH ₂) ₄ CH(CH ₂) ₅ CH ₃	16.07	11.05
HO ₂ -R43: HO ₂ + CH ₃ (CH ₂) ₁₁ CH ₃ → H ₂ O ₂ + CH ₂ (CH ₂) ₁₁ CH ₃	19.56	13.62
HO ₂ -R44: HO ₂ + CH ₃ (CH ₂) ₁₁ CH ₃ → H ₂ O ₂ + CH ₃ CH(CH ₂) ₁₀ CH ₃	16.31	10.85
HO ₂ -R45: HO ₂ + CH ₃ (CH ₂) ₁₁ CH ₃ → H ₂ O ₂ + H ₂ +CH ₃ CH ₂ CH(CH ₂) ₉ CH ₃	15.81	11.13
HO ₂ -R46: HO ₂ + CH ₃ (CH ₂) ₁₁ CH ₃ → H ₂ O ₂ + CH ₃ (CH ₂) ₂ CH(CH ₂) ₈ CH ₃	16.19	11.06
HO ₂ -R47: HO ₂ + CH ₃ (CH ₂) ₁₁ CH ₃ → H ₂ O ₂ + CH ₃ (CH ₂) ₃ CH(CH ₂) ₇ CH ₃	15.62	11.08
HO ₂ -R48: HO ₂ + CH ₃ (CH ₂) ₁₁ CH ₃ → H ₂ O ₂ + CH ₃ (CH ₂) ₄ CH(CH ₂) ₆ CH ₃	16.14	10.97
HO ₂ -R49: HO ₂ + CH ₃ (CH ₂) ₁₁ CH ₃ → H ₂ O ₂ + CH ₃ (CH ₂) ₅ CH(CH ₂) ₅ CH ₃	15.45	11.16
HO ₂ -R50: HO ₂ + CH ₃ (CH ₂) ₁₂ CH ₃ → H ₂ O ₂ + CH ₂ (CH ₂) ₁₂ CH ₃	19.00	13.64
HO ₂ -R51: HO ₂ + CH ₃ (CH ₂) ₁₂ CH ₃ → H ₂ O ₂ + CH ₃ CH(CH ₂) ₁₁ CH ₃	16.42	10.88
HO ₂ -R52: HO ₂ + CH ₃ (CH ₂) ₁₂ CH ₃ → H ₂ O ₂ + H ₂ +CH ₃ CH ₂ CH(CH ₂) ₁₀ CH ₃	15.68	11.15
HO ₂ -R53: HO ₂ + CH ₃ (CH ₂) ₁₂ CH ₃ → H ₂ O ₂ + CH ₃ (CH ₂) ₂ CH(CH ₂) ₉ CH ₃	16.20	11.10
HO ₂ -R54: HO ₂ + CH ₃ (CH ₂) ₁₂ CH ₃ → H ₂ O ₂ + CH ₃ (CH ₂) ₃ CH(CH ₂) ₈ CH ₃	15.61	11.04
HO ₂ -R55: HO ₂ + CH ₃ (CH ₂) ₁₂ CH ₃ → H ₂ O ₂ + CH ₃ (CH ₂) ₄ CH(CH ₂) ₇ CH ₃	16.16	11.17

HO ₂ -R56: HO ₂ + CH ₃ (CH ₂) ₁₂ CH ₃ → H ₂ O ₂ + CH ₃ (CH ₂) ₅ CH(CH ₂) ₆ CH ₃	15.68	11.18
HO ₂ -R57: HO ₂ + CH ₃ (CH ₂) ₁₃ CH ₃ → H ₂ O ₂ + CH ₂ (CH ₂) ₁₃ CH ₃	19.69	13.63
HO ₂ -R58: HO ₂ + CH ₃ (CH ₂) ₁₃ CH ₃ → H ₂ O ₂ + CH ₃ CH(CH ₂) ₁₂ CH ₃	16.25	10.87
HO ₂ -R59: HO ₂ + CH ₃ (CH ₂) ₁₃ CH ₃ → H ₂ O ₂ + H ₂ +CH ₃ CH ₂ CH(CH ₂) ₁₁ CH ₃	15.64	11.15
HO ₂ -R60: HO ₂ + CH ₃ (CH ₂) ₁₃ CH ₃ → H ₂ O ₂ + CH ₃ (CH ₂) ₂ CH(CH ₂) ₁₀ CH ₃	16.23	11.10
HO ₂ -R61: HO ₂ + CH ₃ (CH ₂) ₁₃ CH ₃ → H ₂ O ₂ + CH ₃ (CH ₂) ₃ CH(CH ₂) ₉ CH ₃	15.58	11.00
HO ₂ -R62: HO ₂ + CH ₃ (CH ₂) ₁₃ CH ₃ → H ₂ O ₂ + CH ₃ (CH ₂) ₄ CH(CH ₂) ₈ CH ₃	16.05	11.01
HO ₂ -R63: HO ₂ + CH ₃ (CH ₂) ₁₃ CH ₃ → H ₂ O ₂ + CH ₃ (CH ₂) ₅ CH(CH ₂) ₇ CH ₃	15.65	11.00
HO ₂ -R64: HO ₂ + CH ₃ (CH ₂) ₁₃ CH ₃ → H ₂ O ₂ + CH ₃ (CH ₂) ₆ CH(CH ₂) ₆ CH ₃	16.20	11.08
HO ₂ -R65: HO ₂ + CH ₃ (CH ₂) ₁₄ CH ₃ → H ₂ O ₂ + CH ₂ (CH ₂) ₁₄ CH ₃	19.36	13.64
HO ₂ -R66: HO ₂ + CH ₃ (CH ₂) ₁₄ CH ₃ → H ₂ O ₂ + CH ₃ CH(CH ₂) ₁₃ CH ₃	16.54	10.88
HO ₂ -R67: HO ₂ + CH ₃ (CH ₂) ₁₄ CH ₃ → H ₂ O ₂ + H ₂ +CH ₃ CH ₂ CH(CH ₂) ₁₂ CH ₃	15.66	11.15
HO ₂ -R68: HO ₂ + CH ₃ (CH ₂) ₁₄ CH ₃ → H ₂ O ₂ + CH ₃ (CH ₂) ₂ CH(CH ₂) ₁₁ CH ₃	16.05	11.10
HO ₂ -R69: HO ₂ + CH ₃ (CH ₂) ₁₄ CH ₃ → H ₂ O ₂ + CH ₃ (CH ₂) ₃ CH(CH ₂) ₁₀ CH ₃	15.45	10.94
HO ₂ -R70: HO ₂ + CH ₃ (CH ₂) ₁₄ CH ₃ → H ₂ O ₂ + CH ₃ (CH ₂) ₄ CH(CH ₂) ₉ CH ₃	16.09	11.07
HO ₂ -R71: HO ₂ + CH ₃ (CH ₂) ₁₄ CH ₃ → H ₂ O ₂ + CH ₃ (CH ₂) ₅ CH(CH ₂) ₈ CH ₃	15.56	11.01
HO ₂ -R72: HO ₂ + CH ₃ (CH ₂) ₁₄ CH ₃ → H ₂ O ₂ + CH ₃ (CH ₂) ₆ CH(CH ₂) ₇ CH ₃	15.98	11.00

Chapter 4 A Metric-based Multi-Structural Method for Calculating Conformational-Rovibrational Partition Functions of Large Molecules

4.1 Introduction

There are two crucial factors in the calculation of thermochemistry and chemical kinetics of large straight-chain alkanes, namely the single-point energy (introduced the ONIOM method for large straight-chain alkanes in Chapter 3) and the partition function. For example, the hydrogen abstraction reaction from an n-alkane by a hydrogen atom, $RH + H \rightarrow R \cdot + H_2$, has a distinct energy barrier along with its reaction coordinate, the transition state theory (TST) predicts its high-pressure limit rate coefficient as [87-89]:

$$k(T) = \frac{k_B T}{h} \frac{Q^\ddagger}{Q_{RH} Q_H} \exp\left(-\frac{E^\ddagger}{k_B T}\right) \quad (4.1)$$

where Q is the partition function, E is the energy barrier, the superscript “ \ddagger ” denotes the transition state, and k_B , T , and h are the Boltzmann constant, temperature, and the Planck constant, respectively. The uncertainty of the theoretical reaction rate constant is significantly affected by the accuracy of the energy barrier (particularly at relatively low temperatures) and partition functions (particularly at relatively high temperatures).

In recent years, there are extensive theoretical studies on high-level single-point energy calculation of large molecules. Based on the well-known ONIOM (our own N-layered integrated molecular orbital and molecular mechanics) [66], Zhang et al. [35, 67] proposed a two-layer ONIOM method, in which the QCISD(T)/CBS and DFT/6-

311++G(d,p) methods are used for the high layer and the low layer, respectively. Li et al. [90] developed a generalized energy-based fragmentation (GEBF) approach, in which a large molecule is divided into small fragments, and the total energy of the large molecule is obtained from synthesizing the small fragments. Wu et al. [91] proposed a cascaded group-additivity (CGA) ONIOM method by combining the group additivity and two-layer ONIOM methods, in which a large molecule is partitioned into cascaded individual groups and the ONIOM method is used for their energy calculations.

For calculating partition functions, a common approach is to assume the separability of various modes (degrees of freedom) of external and internal motions, which leads to the additivity of their energies and in turn the multiplicativity of their partition functions as such

$$Q = Q_{\text{trans}}Q_{\text{rot}}Q_{\text{vib}}Q_{\text{elec}} \quad (4.2)$$

where the translational (Q_{trans}), rotational (Q_{rot}), vibrational (Q_{vib}), and electronic (Q_{elec}) partition functions can be separately calculated. Generally, vibrational modes can be treated by using the harmonic oscillator (HO) approximation. However, using the HO approximation to treat those torsional modes with relatively low frequencies will result in large errors, particularly at relatively high temperatures.

Extensive studies have been conducted to deal with low-frequency torsional modes. Pitzer and Gwinn [36] performed a seminal work on the one-dimensional hindered rotor (1D-HR) treatments and their subsequent works [92, 93] also had far-reaching effects on later studies [94-97]. The Pitzer-Gwinn-like methods have been widely adopted in

dealing with torsional anharmonicity in partition function calculations [77, 98-101]. The applicability of the 1D-HR approach relies on the two approximations: the torsions are decoupled, and each torsion corresponds to (therefore is used to replace) a specific normal mode. However, torsions are often coupled with each other in a large molecule, and it is hard (even impossible) to establish a one-to-one correspondence between the low-frequency torsions and normal modes. As a result, there is a natural idea to treat torsional coupling through constructing the high-dimensional torsional potential energy surface (PES), which makes a more accurate treatment possible at the cost of the high computational load [102, 103].

Zheng et al. [38] proposed a new class of methods called multi-structural (MS) methods. The methods need neither to calculate high-dimensional torsional PES nor to manually correspond each torsion to a normal mode [104-107]. Instead, the MS methods use Voronoi tessellation [108] to divide the high-dimensional torsional PES into a number of Voronoi cells around local minima on the torsional PES; in each of the cells, the high-dimensional integral of classical partition function can be analytically expressed by virtue of the geometric and frequency information of stationary points (local minima and saddle points) on the torsional PES. An open-source code MSTor was developed based on the multi-structural approximation with torsional anharmonicity (referred to as MS-T hereinafter) and has been extensively used in many chemical systems [38, 39, 104, 107, 109].

One of the key procedures in the MS-T calculations is to identify all torsional

conformers on the high-dimensional torsional PES. A common approach for that is to generate initial-guess structures for all torsions and then to rule out the identical structures from the results of geometry optimization. Each torsion (excluding the simplest methyl groups) is assumed to have three conformers, and therefore 3^N initial-guess structures are needed for a molecular system with N non-methyl torsions [105]. Apparently, a huge number of geometry optimization calculations are needed by applying the MS-T method to large molecules. For example, common diesel fuel ranges approximately from $C_{10}H_{20}$ to $C_{15}H_{28}$ [110]. Taking *n*-decane as an example, the MS-T method needs to generate $3^7 = 2187$ initial-guess structures (excluding two methyl groups) for geometry optimization calculations. Furthermore, identifying distinguishable structures among these optimized structures is another challenging work and usually manually formidable.

To reduce the computational load of the MS-T method, Bao et al. [111] proposed a cost-effective method to approximate the MS-T partition function, called dual-level electronic structure method, in which a low-level method is used to optimize all initial-guess structures first, and then a high-level method is used to re-optimize some of the distinguishable structures in order of increasing energy identified by a low-level method. They studied a transition state structure of the hydrogen abstraction of ketohydroperoxide by OH radical, in which the 7 non-methyl torsions generate 2187 initial-guess structures. Although the dual-level method can reduce the computational cost to a certain extent, it still has to deal with a huge number of optimized structures,

particularly in large molecular systems. Wu et al. [112] proposed a multi-structural 2-dimensional torsion (MS-2DT) method, which considers all pairs of torsions to generate initial-guess structures, reducing the number of initial-guess structures from 3^N to $9N(N - 1)/2$. They used the MS-2DT method to study eighteen alkanes ($C_6 - C_8$) and the results are in good agreement with the original MS-T method.

Regardless of the noticeable success of the MS method and its variants in calculating partition functions accurately and efficiently, some critical questions remain to be answered: do we really need a complete set of distinguishable torsional conformers for partition function calculation? Can we find an appropriately chosen small subset of distinguishable torsional conformers which can significantly reduce the computational cost while retain acceptable accuracy? How do we assess the performance of various subsets (the complete set can be treated as a subset of itself)? In the present work, we proposed the simplest variant MS-2NN and a metric-based method to answer the above questions, particularly the last question that determines our answers to the first two. We shall expatiate the simplest variant MS-2NN and metric-based methods in Section 4.2, followed by the validation in Section 4.3, in which we compared the MS-T and MS-2NN methods in the systems of $n-C_nH_{2n+2} + H$ ($n=6-7$). In addition, we used the MS-2NN method to study larger n -alkanes ($n=8-10$) and compared the entropy results with the literature data. The other variants of the MS-T method, the MS-2DT and MS-3DT methods, are also considered to verify the findings by the metric-based method.

4.2 Theoretical Methods

4.2.1 Multi-structural (MS) Method

In the MS method [38], the quantum-mechanical torsional partition function is approximated by a classical mechanical (CM) configuration integral [113] as

$$Q^{\text{CM}} = \left(\frac{1}{2\pi\beta\hbar^2} \right)^{t/2} (\det\{\mathbf{D}\})^{1/2} \int_0^{2\pi/\sigma_1} \dots \int_0^{2\pi/\sigma_t} d\phi_1 \dots d\phi_t e^{-\beta V(\phi_1, \dots, \phi_t)} \quad (4.3)$$

where $\beta = 1/k_{\text{B}}T$, k_{B} the Boltzmann's constant, T the temperature, \hbar the reduced Planck's constant, \mathbf{D} the torsional kinetic energy matrix that evaluated at the global minimum, ϕ_{τ} the torsional internal coordinate, σ_{τ} the parameter characterizing the periodicity of torsional space, and t the total number of coupled torsions.

The MS method adopted interna- coordinates treatment to deal with the torsions. The method does not need to scan the potential energy surface and to establish a one-to-one correspondence between the low-frequency torsions and normal modes, for as only need the geometries and Hessians of the distinguish conformers (structures). The total partition function can be calculated as

$$Q = Q_{\text{trans}} Q_{\text{elec}} Q_{\text{rot}} \prod_{m=1}^F q_{\text{vib},m} \quad (4.4)$$

where the translational (Q_{trans}), electronic (Q_{elec}), and rotational (Q_{rot}) partition functions, can be separately calculated. $q_{\text{vib},m}$ is the vibrational partition function of mode m . Similarly, the total partition function can be written as

$$Q = Q_{\text{trans}} Q_{\text{elec}} Q_{\text{con-rovib}} \quad (4.5)$$

where $Q_{\text{con-rovib}}$ is the conformational-rovibrational partition function. The

conformational-rovibrational partition function is given by [38]:

$$Q_{con-rovib}^{MS-T} = \sum_{j=1}^J Q_j^{rot} \exp(-\beta U_j) Q_j^{HO} Z_j \prod_{\tau=1}^t f_{j,\tau} \quad (4.6)$$

where Q_j^{rot} and Q_j^{HO} are the rotational partition function of structure J and the usual normal-mode harmonic oscillator vibrational partition function of structure J , respectively. U_j is relative energy with respect to a benchmark structure; β is $1/k_B T$ where k_B is Boltzmann's constant and T is temperature; The internal-coordinate torsional anharmonicity function $f_{j,\tau}$ which is in conjunction with Z_j that is a factor designed to ensure the correct high-temperature limit accounts for the presence of the torsion τ in the j th structure.

Because of the existence of many local minima that contribute to the evaluation of the partition function, the entire torsional space can be divided into a certain number of distinct subspaces which correspond to each local minimum (structure), and such that the total partition function is a summation of that for all the local minima. For each structure j belonging to a certain torsion τ , the PES is assumed to be described by a periodic function:

$$V_{j,\tau} = U_j + \frac{W_{j,\tau}}{2} \{1 - \cos[M_{j,\tau}(\phi_\tau - \phi_{\tau,eq,j})]\}, \quad \frac{-\pi}{M_{j,\tau}} \leq (\phi_\tau - \phi_{\tau,eq,j}) \leq \frac{\pi}{M_{j,\tau}} \quad (4.7)$$

where U_j and $\phi_{\tau,eq,j}$ are the potential energy and the torsional internal coordinate of the local minimum j , $M_{j,\tau}$ the periodicity parameter. $W_{j,\tau}$ is the effective barrier height estimated by

$$W_{j,\tau} = \frac{2I_{j,\tau}\omega_{j,\tau}^2}{M_{j,\tau}^2} \quad (4.8)$$

where $\omega_{j,\tau}$ is the frequency and $I_{j,\tau}$ the internal moment of inertia. For the torsional anharmonicity induced by strongly coupled torsions, the PES within a certain structure j is assumed to be locally separable so that

$$V_j(\phi_1, \dots, \phi_t) \approx \sum_{\tau=1}^t V_{j,\tau}(\phi_\tau) \quad (4.9)$$

The assignment of $M_{j,\tau}$ is an essential part of the MS method. For nearly separable torsions with approximately evenly distributed local minima, $M_{j,\tau}$ simply equals the total number of local minima in the specific torsion; For strongly coupled torsions, $M_{j,\tau}$ is determined by Voronoi tessellation, in which $M_{j,\tau}$ is replaced by M_j^{SC} and assumed to be equivalent in every strongly coupled torsion. Then the local periodicity $M_{j,\tau}$ is defined by

$$M_{j,\tau} = M_j^{\text{SC}} = 2\pi(\Omega_j^{\text{SC}})^{-1/t_{\text{sc}}} \quad (4.10)$$

where Ω_j^{SC} is the hypervolume of subspace j and t_{sc} is the total number of strongly coupled torsions. Overall, $M_{j,\tau}$ plays three important roles in the method. First, it controls the local periodicity. Second, it determines the integral subspace for a specific structure. Third, it accounts for the evaluation of implicit barrier heights.

4.2.2 Metric-based Method

As discussed in the preceding section, identifying all possible distinguishable local minima is crucial in the MS method because it affects the Voronoi tessellation, the local PES, and in turn the partition function. Previous studies have shown that the calculation of partition function by using the MS method is sensitive to the number of identified local minima [111, 112].

The central idea of the metric-based method to be expatiated below is to mathematically quantify the “similarity” or “closeness” of two torsional conformers and then to quantify the contribution of a conformer to the calculation of partition function. In previous studies, two optimized structures were considered distinguishable if they have at least one different dihedral angle of torsion or if they have different single-point energies. Additional treatments should be given to the optical isomers. It is apparently unfeasible to manually distinguish all optimized structures because the total number of comparisons for each pair of structures is $N + 1$, including N comparisons of dihedral angles and one comparison of energy, and that for all structures is $(N + 1)M(M - 1)/2$, where M is the total number of optimized structures. Although computer programs can be developed to identify distinguishable conformers, the computational load is significant for usually very large M . For example, the total number of comparisons is about $3^{15} \approx 1.4 \times 10^7$ for $N = 7$ (e.g. *n*-decane).

Inspired by the mathematical concept of metric or distance function [114, 115], we defined a dihedral metric and an energy metric to quantify the difference between any two structures. For two structures s_j and s_k , where $j \neq k$, the dihedral metric $d_D(s_j, s_k)$ is defined by

$$d_D(s_j, s_k) = \sum_{n=1}^N d(\theta_j^n, \theta_k^n) \quad (4.11)$$

Where θ_j^n is the dihedral angle corresponding to the n -th torsion of the structure s_j , $d(\theta_j^n, \theta_k^n)$ is a distance function accounting for the difference of two corresponding dihedral angles:

$$(\theta_j^n, \theta_k^n) = \min \{|\theta_j^n - \theta_k^n|, |\theta_j^n - \theta_k^n + 2\pi|, |\theta_j^n - \theta_k^n - 2\pi|\} \quad (4.12)$$

Eq. (4.11) can be treated as a high-dimensional variant of the ‘‘Manhattan distance’’, also known as taxicab geometry [116-118]. As a metric, $d(x, y)$ must satisfy the three axioms such as 1) $d(x, y) \geq 0$ and the equality holds only for $x = y$; 2) $d(x, y) = d(y, x)$; and 3) $d(x, y) \leq d(x, z) + d(z, y)$ [119, 120]. No cases were found to violate the above three metric axioms in our computational results.

Considering two structures of the same energy may have different dihedral metric, for example the optical isomers, we defined the energy metric by

$$d_E(s_j, s_k) = |E_{s_j} - E_{s_k}| \quad (4.13)$$

where E denotes the single-point energy. It is readily seen that the energy metric satisfies all the three metric axioms. In the present metric-based method, two structures are considered similar or close if their dihedral and energy metrics are small. The ‘‘smallness’’ of a metric can be so determined that the calculation results reach a prescribed accuracy.

It is noted that the low-energy structures contribute to the partition function significantly more than the high-energy structures because the Boltzmann factor $e^{-\Delta E/kT}$ is significantly small for a large $\Delta E = E - E_{min}$, where E_{min} is the single-point energy of the lowest-energy conformer. For example, the contribution of a higher-energy conformer to the total partition function is about 13.5% (at $T = 1000K$) and 1.8% (at $T = 500K$) of that of the lower-energy conformer if ΔE is 2 kcal/mol. Consequently, a complete set of distinguishable local minima could be unnecessary for

the purpose of partition function calculation since many local minima might have negligible contribution to the partition function. Thus, an ideal way to reduce the computational cost while remain the computational accuracy is to find local minima close to the lowest-energy one.

For convenience of the statistical analysis to be discussed in the following sections, the dihedral and energy metrics can be normalized by

$$\bar{d}_D(s_j, s_k) = d_D(s_j, s_k)/2\pi N \quad (4.14)$$

$$\bar{d}_E(s_j, s_k) = d_E(s_j, s_k)/E_{max} \quad (4.15)$$

where N and E_{max} denote the number of torsions and the maximum of potential energy in the distinguishable structures, respectively. It is seen that the normalization ensures that $\bar{d}_D \in [0,1]$ and $\bar{d}_E \in [0,1]$.

4.2.3 Nearest Neighborhood Method

In the present method, there is no strict requirement for the selection of N (the number of coupled torsions) in generating the initial-guess structures of local minima. In principle, a better result would be obtained for a larger N (up to the total number of torsions), however, the total number of initial-guess structures will increase according to 3^N . The MS-2DT method [112] assumes that any two torsions are coupled and reduce the total number of initial-guess structures to $9N(N-1)/2$, which quadratically increases with N . Considering that nearby torsions often have stronger coupling than those being far away, we proposed to use the so-called nearest neighborhood method to generate initial-guess structures. Specifically, all N torsions

in a molecule are divided into a certain number of groups, each of which contains n neighborhood torsions. For each group, we can generate 3^n initial-guess structures and the total number of initial-guess structures for all groups is about $(N - 1)3^n$, which is significantly smaller than 3^N for $n < N$. In the following text, we denote the method with n nearest neighborhood torsions by nNN. It is noted that the MS-2DT method is not a special case of the nearest neighborhood method because every two (not every two neighbors) torsions are assumed to be coupled.

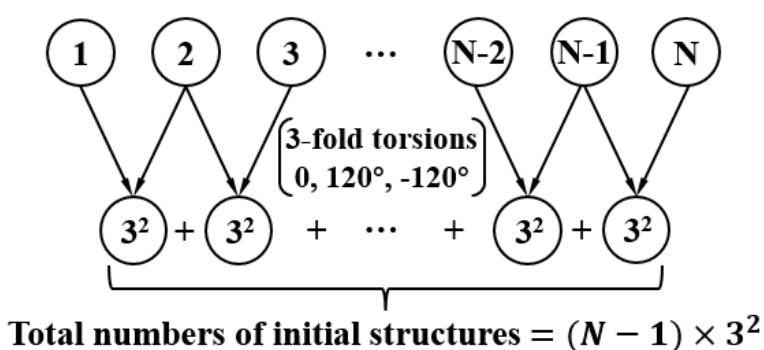


Figure 4.1 Schematic of the simplest variant MS-2NN (two nearest neighborhood torsions are coupled) method to generate initial-guess structures.

For the purpose of validating the proposed MS-nNN method, the present study adopted the simplest non-trivial scenario of $n = 2$, since $n = 1$ would result in the trivial case where all torsions are uncoupled, as shown in Figure 4.1. Taking n -decane again as an example (excluding methyl groups), the number of initial-guess structures by MS-T, MS-2DT, and the present MS-2NN method are $3^7 = 2189$, $C_7^2 \times 3^2 = 189$, and $(7 - 1) \times 3^2 = 54$, respectively. It is apparent that the MS-2NN method reduces greatly the computational cost compared to the other two methods. The comparison of their computational results for partition functions will be presented and their performance will be assessed by using the proposed metric-based method in the

following Section. It should be noted that the present metric-based method can be combined with any method for generating initial-guess structures.

4.2.4 Electronic Structure Method

For validating the present computational methods, we considered the large straight-chain alkane molecules $n\text{-C}_n\text{H}_{2n+2}$ ($n = 6\text{-}10$). The geometries optimization and vibrational frequencies of the stationary points for the hydrogen abstraction reactions of $n\text{-C}_n\text{H}_{2n+2} + \text{H}$ ($n = 6\text{-}7$) and larger n -alkanes molecules (from C_8 to C_{10}) were calculated at B3LYP/6-311++G(d,p) level [71]. All the calculations in the present study were performed with the Gaussian 09 program package [78].

Table 4.1 The number of distinguishable structures for reactants and transition states (excluding mirror-image structures)

Species	MS-T	MS-2NN
<i>n</i> -hexane	9	5
<i>n</i> -hexane-TS1	28	14
<i>n</i> -hexane-TS2	17	11
<i>n</i> -hexane-TS3	17	11
<i>n</i> -heptane	22	7
<i>n</i> -heptane-TS1	65	17
<i>n</i> -heptane-TS2	41	15
<i>n</i> -heptane-TS3	41	15
<i>n</i> -heptane-TS4	22	8

4.3 Results and Discussion

4.3.1 Structures Generation by MS-2NN and MS-T

For the comparison between the MS-T and MS-2NN methods, we studied the hydrogen abstraction reactions of *n*-hexane and *n*-heptane by H atom. The MS-T method is too computationally expensive for larger systems such as *n*-octane, *n*-nonane, and *n*-decane, which were studied by the MS-2NN method only. Table 4.1 summarizes

the number of distinguishable structures for all reactants and transition states of the hydrogen abstraction reactions of $n\text{-C}_n\text{H}_{2n+2} + \text{H}$ ($n = 6-7$) using MS-T and MS-2NN methods.

As an example of reactants, the n -heptane molecule has six torsions that are associated with internal rotations around the six C-C single bonds. The seven carbon atoms of n -heptane are labeled as: $\text{H}_3\text{C}^{(1)}\text{-H}_2\text{C}^{(2)}\text{-H}_2\text{C}^{(3)}\text{-H}_2\text{C}^{(4)}\text{-H}_2\text{C}^{(5)}\text{-H}_2\text{C}^{(6)}\text{-H}_3\text{C}^{(7)}$. Excluding the first and the last methyl groups, the rest of the four torsions are considered for generating initial-guess structures. Therefore, 81 initial-guess structures were generated by MS-T method and 27 initial-guess structures were generated by the MS-2NN method. The total number of distinguishable structures (excluding mirror-image structures) are 22 by MS-T method and 7 by MS-2NN method.

As an example of transition states, the n -heptane-TS1, an H atom in the methyl group was abstracted by H radical. The seven carbon atoms of n -heptane-TS1 are labeled as: $\text{H}_3\text{C}^{(1)}\text{-H}_2\text{C}^{(2)}\text{-H}_2\text{C}^{(3)}\text{-H}_2\text{C}^{(4)}\text{-H}_2\text{C}^{(5)}\text{-H}_2\text{C}^{(6)}\text{-H}_3\text{C}^{(7)}\text{-H}$. Excluding the $\text{H}_3\text{C}^{(1)}$ methyl group, 243 initial-guess structures were generated by the MS-T method and 36 initial-guess structures were generated by MS-2NN method. The total number of distinguishable structures (excluding mirror-image structures) are 65 by the MS-T method and 17 by the MS-2NN method.

Take n -hexane as an example, Table 4.2 lists all distinguishable structures which identified by using MS-T and MS-2NN methods in ascending sort order of the energy metric with respect to the benchmark structures (the lowest-energy structures, labeled

as S1). It is seen that the distinguishable structures generated by the MS-2NN method form a small subset of those generated by the MS-T method. Table S4.1 to Table S4.8 in Appendix of section 4.5 list all other distinguishable structures of reactants and transition states (including, *n*-hexane-(TS1-3), *n*-heptane, and *n*-heptane-(TS1-4)) in the hydrogen abstraction reactions of $n\text{-C}_n\text{H}_{2n+2} + \text{H}$ ($n = 6-7$) by using the same methods as *n*-hexane.

Table 4.2 Structural information (in the ascending order of energy metric) for *n*-hexane using the MS-T and MS-2NN (in bold red) methods (units in kcal/mol for energy and degree for dihedral angles).

Structure	Torsion			$d_D(S_1, S_j)$	Energy	$d_E(S_1, S_j)$
	C ⁽²⁾ -C ⁽³⁾	C ⁽³⁾ -C ⁽⁴⁾	C ⁽⁴⁾ -C ⁽⁵⁾			
S1	180.00	180.00	180.00	0.00	0.00	0.00
S2	-179.83	177.30	65.91	116.95	0.85	0.85
S3	176.89	66.87	176.89	119.36	0.88	0.88
S4	176.25	63.72	63.07	236.96	1.64	1.64
S5	66.38	174.70	66.38	232.54	1.70	1.70
S6	66.54	180.00	-66.54	226.93	1.76	1.76
S7	62.29	60.42	62.29	355.01	2.44	2.44
S8	174.88	64.72	-91.28	209.12	3.34	3.34
S9	62.74	65.75	-89.99	321.52	4.21	4.21

4.3.2 Qualitative Verification of MS-2NN Method based on Voronoi Tessellation

In our previous study [121] about MS-T method, we proposed an improved method (MS-ASB) to approximately reconstruct the torsional potential energy surface based on Voronoi tessellation. One of the important findings in the study is that the extent of torsional anharmonicity is correlated with the non-uniform distribution of local minima in the coordinate space of dihedrals. In the present study, we applied this understanding to examine the nearest neighborhood approximation.

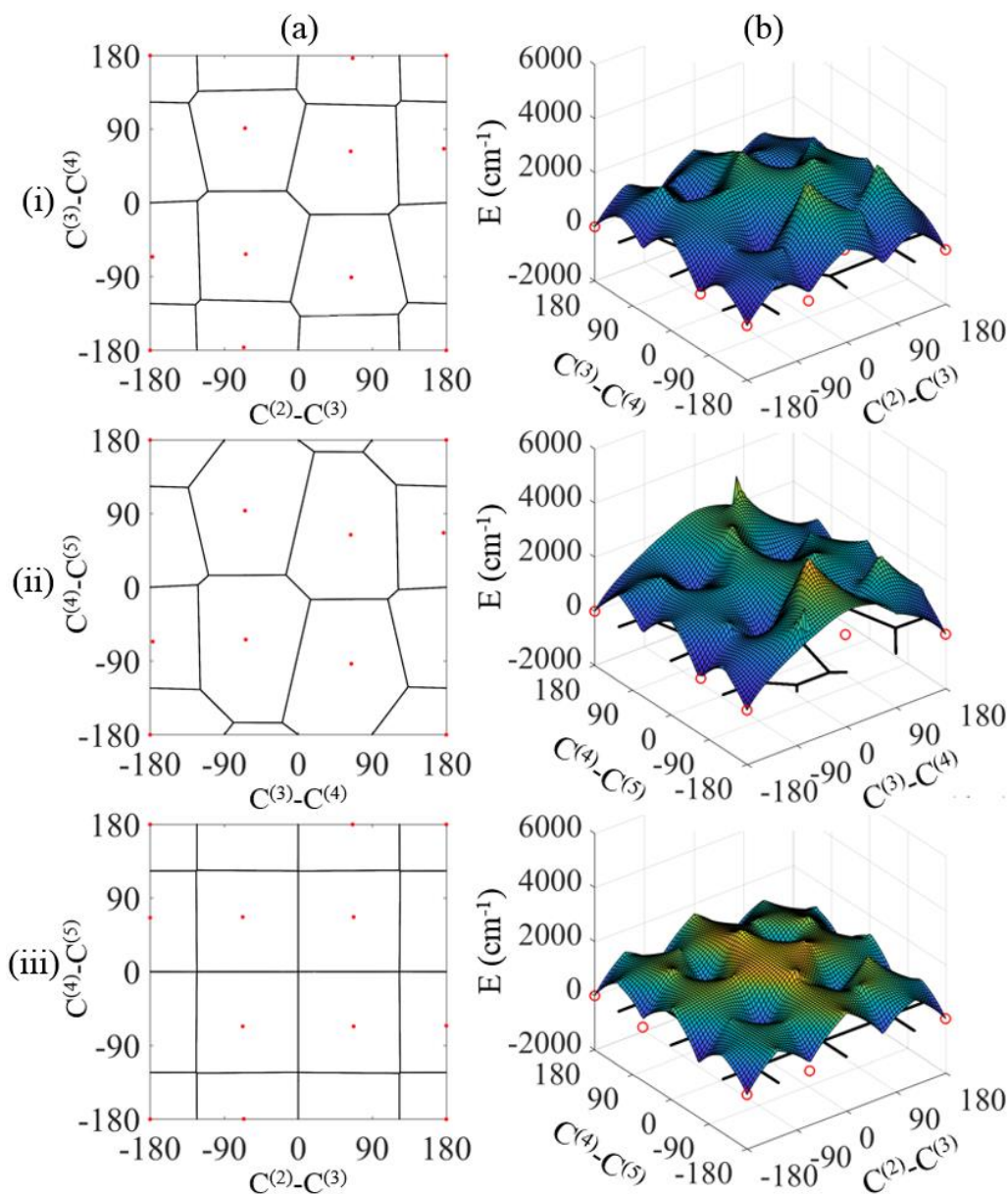


Figure 4.2 (a) weighted Voronoi tessellation and (b) reconstructed potential energy surface based on the method [121].

For *n*-heptane, 4 torsions, $C^{(2)}-C^{(3)}$, $C^{(3)}-C^{(4)}$, $C^{(4)}-C^{(5)}$, and $C^{(5)}-C^{(6)}$, are considered in the MS-T method. The present 2NN approximation considered only two distinct combinations, $[C^{(2)}-C^{(3)}, C^{(3)}-C^{(4)}]$ and $[C^{(3)}-C^{(4)}, C^{(4)}-C^{(5)}]$, as adjacent coupled torsions. As shown in Figure 4.2(i), it can be clearly seen that the coupling of $[C^{(2)}-C^{(3)}, C^{(3)}-C^{(4)}]$ results in a non-uniform distribution of local minima so that there is no strict periodic variation along either the $C^{(2)}-C^{(3)}$ coordinate or the $C^{(3)}-C^{(4)}$ coordinate. Similar non-

uniformity of local minima can be also seen in Figure 4.2(ii) due to the coupling of $[C^{(3)}-C^{(4)}, C^{(4)}-C^{(5)}]$. The torsions $C^{(2)}-C^{(3)}$ and $C^{(4)}-C^{(5)}$ are assumed to be uncoupled according to the present 2NN approximation. As a comparison, the Voronoi tessellation for the local minima generated by the $[C^{(2)}-C^{(3)}, C^{(4)}-C^{(5)}]$ is shown in Figure 4.2(iii). Apparently, the distribution of local minima is quite uniform and the periodic variation along each coordinate is well retained, implying the decoupling of these two torsions. It should be noted that the above examined case of *n*-heptane does not contain strongly coupled torsions. For the systems containing strongly coupled torsions, such as the molecules with the various functional groups or the transition state structures, the larger nearest neighborhood approximations (e.g. 3NN or 4NN) may be needed for satisfactory results.

4.3.3 Partition Function and Standard State Entropy

The comparison of the partition function ratio of all reactants and transition states of the hydrogen abstraction reactions, $n\text{-C}_n\text{H}_{2n+2} + \text{H}$ ($n = 6-7$), using MS-T and MS-2NN methods are shown in Figure 4.3. As expected, the MS-2NN method predicts smaller values of the partition function for it considers only a subset of the structures considered by the MS-T method. Surprisingly, the differences between the predictions of these two methods are not significant. Specifically, the partition function ratio, $\text{PFR} = Q^{\text{MS-T}}/Q^{\text{MS-2NN}}$, is generally less than 1.5 for *n*-hexane and its transition states and 2.2 for *n*-heptane and its transition states in the range of 300K-2000K, whereas the number of distinguishable structures by the MS-2NN is significantly smaller than the

MS-T method. Therefore, it can be deduced that the MS-2NN method is able to generate the important structures which make a dominant contribution to the partition function calculation.

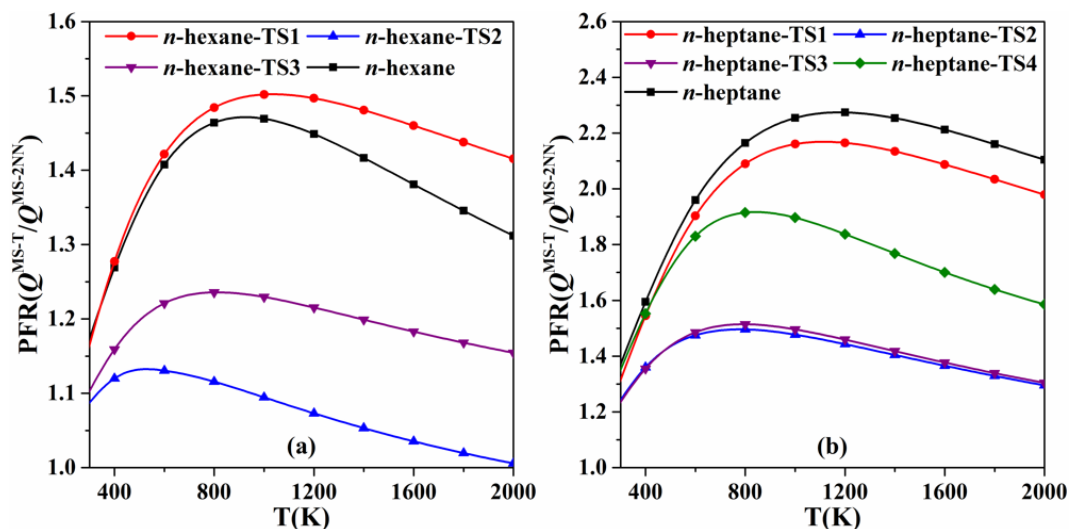


Figure 4.3 The partition function ratio (PFR), Q^{MS-T}/Q^{MS-2NN} , using MS-T and MS-2NN methods for (a) *n*-hexane and *n*-hexane-TS1 to TS3, and (b) *n*-heptane and *n*-heptane-TS1 to TS4.

To further validate the MS-2NN method, we also calculated the standard state entropy which is derived from the partition function as follow:

$$S = k_B \ln Q - \frac{1}{T} \left(\frac{\partial \ln Q}{\partial \beta} \right) \quad (4.13)$$

The calculated entropy results using the MS-T and MS-2NN methods for *n*-alkanes (from C_6 to C_{10}) and the available reference data [122] in the range of 298 to 2000 K are summarized in Table 4.3.

Generally, the calculated entropies using either the MS-T method or the MS-2NN method are slightly less than the reference data. For *n*-hexane and *n*-heptane, the entropies calculated by the MS-T method agree very well with the reference data and the differences are less than 1%. Although the MS-2NN method has very few structures

than the MS-T method, its entropy predictions also agree well with the reference data with the relative errors being less than 2%. We used the MS-2NN method to study the larger *n*-alkanes (from C₈ to C₁₀), for which the MS-T method is computationally unaffordable. It is seen that the differences between the MS-2NN predictions and the reference data slightly increase with the molecule size, but the relative errors are less than 5% from 298 to 1500 K. It is again demonstrated that the present method is capable of generating results with acceptable accuracy for a much lower computational cost compared with the MS-T method.

Table 4.3 Standard state entropy (in cal/mol/K) of *n*-alkanes (from C₆ to C₁₀) at 298.15 – 2000 K calculated using the MS-T and MS-2NN methods and compared with the reference data [122].

Molecule	Method	Standard entropy at different temperatures				
		298.15 K	500 K	1000 K	1500 K	2000 K
<i>n</i> -hexane	MS-T	92.21	114.37	159.70	194.49	222.05
	MS-2NN	91.36	113.26	159.01	194.21	222.00
	Ref. data	92.91	114.84	160.5	195.4	--
<i>n</i> -heptane	MS-T	101.47	127.27	179.93	220.24	252.12
	MS-2NN	99.81	125.10	178.10	218.93	251.18
	Ref. data	102.29	127.72	180.5	220.5	--
<i>n</i> -octane	MS-2NN	107.87	136.38	196.83	243.55	280.38
	Ref. data	111.67	140.61	200.4	245.7	--
<i>n</i> -nonane	MS-2NN	115.63	147.41	215.22	267.72	309.10
	Ref. data	121.04	153.49	220.4	270.8	--
<i>n</i> -decane	MS-2NN	123.56	158.55	233.61	291.88	337.84
	Ref. data	130.42	166.38	240.5	296.0	--

4.3.4 Distribution of Energy and Dihedral Metrics

The preceding sections have shown that the present method can predict partition functions with acceptable accuracy by using a small subset of structures generated by the MS-T method. To understand this result, we can make use of the concepts of energy

and dihedral metrics that we introduced in Section 4.2.2.

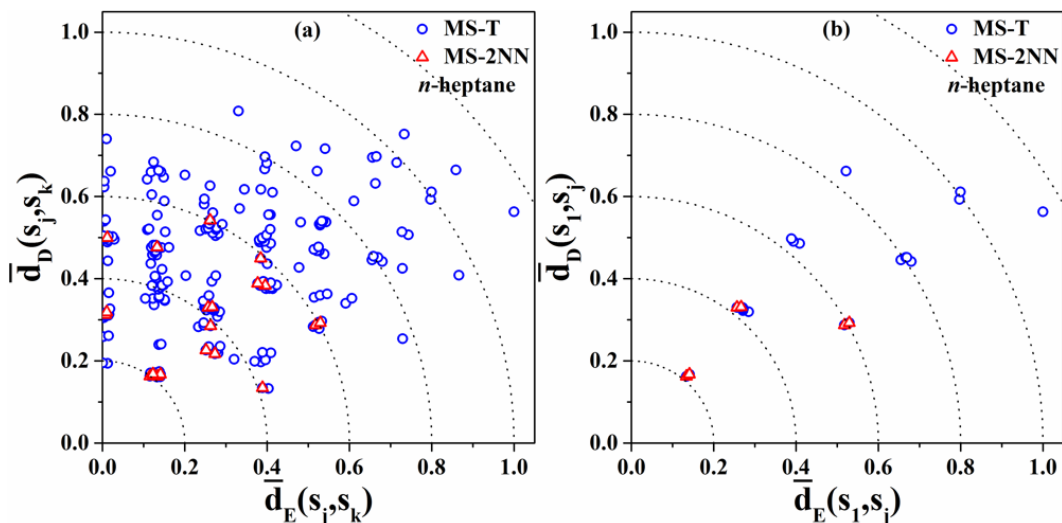


Figure 4.4 Distributions of distinguishable structures of n -heptane in the space of \bar{d}_D and \bar{d}_E using MS-T and MS-2NN methods for different coordinates (a) $(\bar{d}_E(s_j, s_k), \bar{d}_D(s_j, s_k))$ and (b) $(\bar{d}_E(s_1, s_j), \bar{d}_D(s_1, s_j))$.

For n -heptane, 22 and 7 distinguishable structures are identified by the MS-T and MS-2NN methods, respectively. Therefore, we can form $C_{22}^2 = 231$ and $C_7^2 = 21$ pairs of structures for the two methods. Each pair of the j -th and k -th structures has a dihedral metric $\bar{d}_D(s_j, s_k)$ and an energy metric $\bar{d}_E(s_j, s_k)$. We can show all identified structures in the Cartesian space of the metrics as shown in Figure 4.4(a), where each point presents a pair of structures (denoted by the subscript “j” and “k”) and has the coordinates $(\bar{d}_E(s_j, s_k), \bar{d}_D(s_j, s_k))$.

Although Figure 4.4(a) can represent the “similarity” or “closeness” of any two structures, it does not provide information about the relative importance of each structure to the prediction of partition functions. As discussed in the Introduction, those structures that are sufficiently “close” to the lowest energy conformer are more important than those being “far” from it. Consequently, we replotted the figure by

presenting each distinguishable structure in terms of its metrics with respect to the lowest energy conformer (denoted by the subscript “1”), as shown in Figure 4.4(b), where each point presents a structure (denoted by the subscript “j”) has the coordinates $(\bar{d}_E(s_1, s_j), \bar{d}_D(s_1, s_j))$.

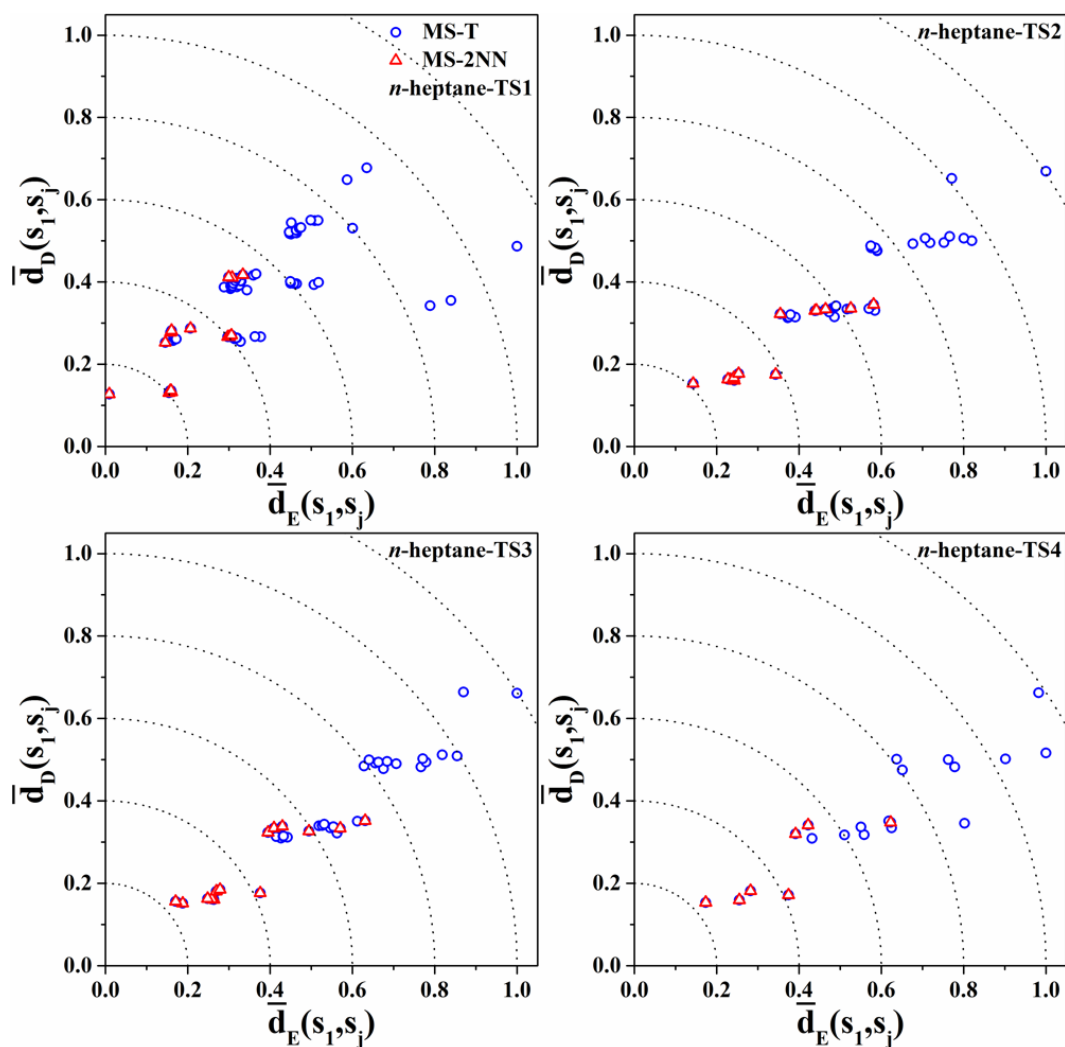


Figure 4.5 Distribution of distinguishable structures (with respect to the lowest energy conformer) in the space of \bar{d}_D and \bar{d}_E using MS-T and MS-2NN methods for *n*-heptane-TS1 to TS4.

In the new representation, those being closer to the origin (representing the lowest energy conformer) make larger contributions to the partition function calculation than those being farther from the origin. It is clearly seen that the structures generated by the

MS-2NN method are all close to the origin, but quite a number of structures generated by the MS-T method are far from the origin. Consequently, the good performance of the MS-2NN method can be understood by that it contains a small but important subset of the structures, and that a full set of distinguishable structures may be unnecessary for calculations with a certain tolerance of errors. The same observation and interpretation apply to the 4 transition states of *n*-heptane, as shown in Figure 4.5, and to *n*-hexane and its transition states, as shown in Figure 4.6.

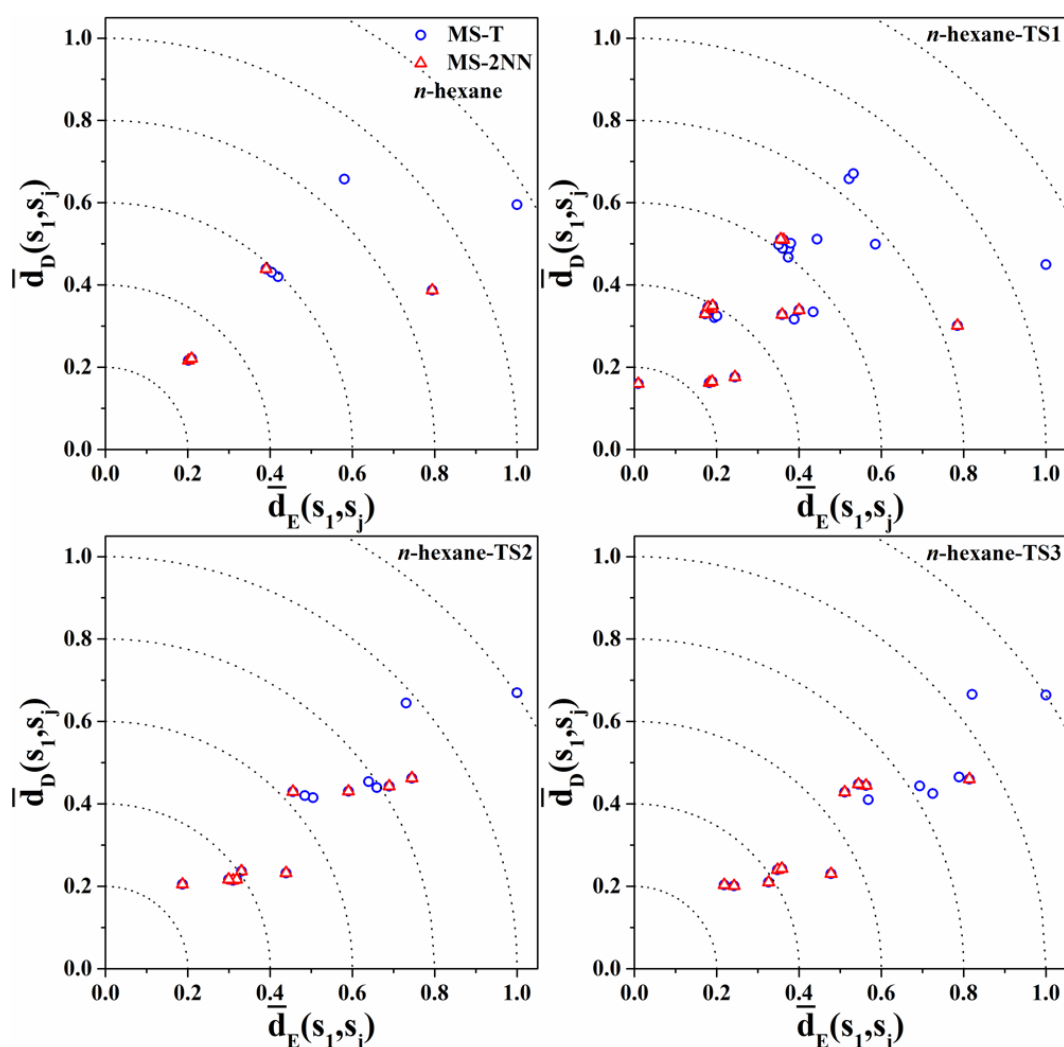


Figure 4.6 Distribution of distinguishable structures (with respect to the lowest energy conformer) in the space of \bar{d}_D and \bar{d}_E using MS-T and MS-2NN methods for *n*-hexane and *n*-hexane-TS1 to TS3.

4.3.5 Comparison of MS-2DT and MS-3DT with MS-T

We can use the above developed metric-based method to assess the performance of other methods, for example the MS-2DT (any two torsions are assumed to be coupled) method of Wu et al. [112] and the MS-3DT (any three torsions are assumed to be coupled) method following the same idea. Compared with the present MS-2NN method, these two methods generate larger subsets of the structure set generated by the MS-T method. The inclusion relation of these subsets is $MS-2NN \subseteq MS-2DT \subseteq MS-3DT \subseteq MS-T$.

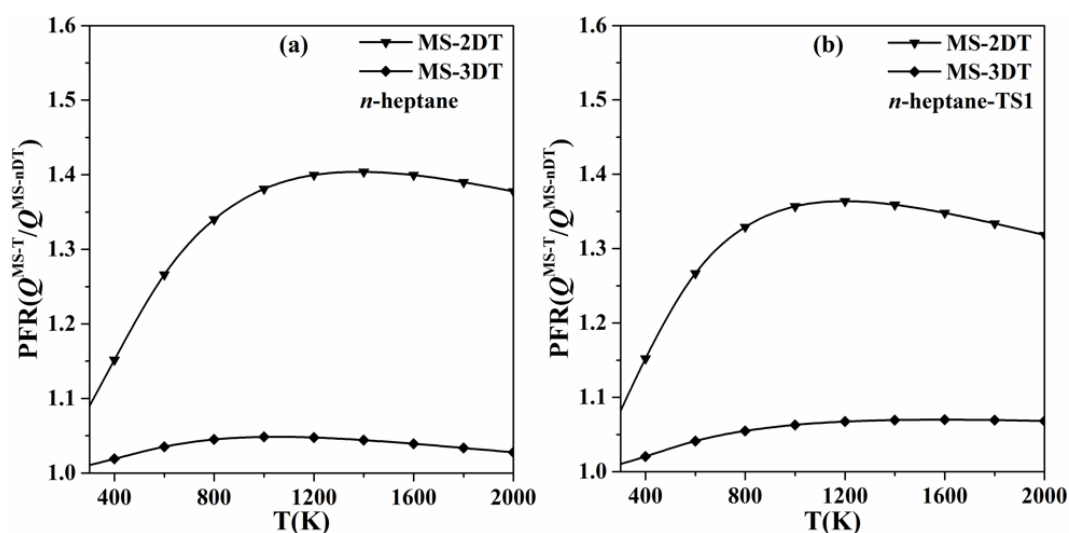


Figure 4.7 The partition function ratio (PFR) of Q^{MS-T}/Q^{MS-nDT} using MS-T and MS-nDT methods for (a) *n*-heptane and (b) *n*-heptane-TS1.

For *n*-heptane, there are 11 and 18 distinguishable structures (excluding mirror-image structures) generated by MS-2DT and MS-3DT, respectively. For *n*-heptane-TS1, there are 32 and 55 distinguishable structures (excluding mirror-image structures) generated by MS-2DT and MS-3DT, respectively. As expected, more structures can make the calculations more accurate. Figure 4.7 shows that the partition function ratio

of $Q^{\text{MS-T}}/Q^{\text{MS-2DT}}$ is less than 1.4 for both cases of *n*-heptane and *n*-heptane-TS1, and the similar small ratios were obtained for other systems. Furthermore, the partition function ratio of $Q^{\text{MS-T}}/Q^{\text{MS-3DT}}$ is as small as 1.1 for all the cases considered in the present study.

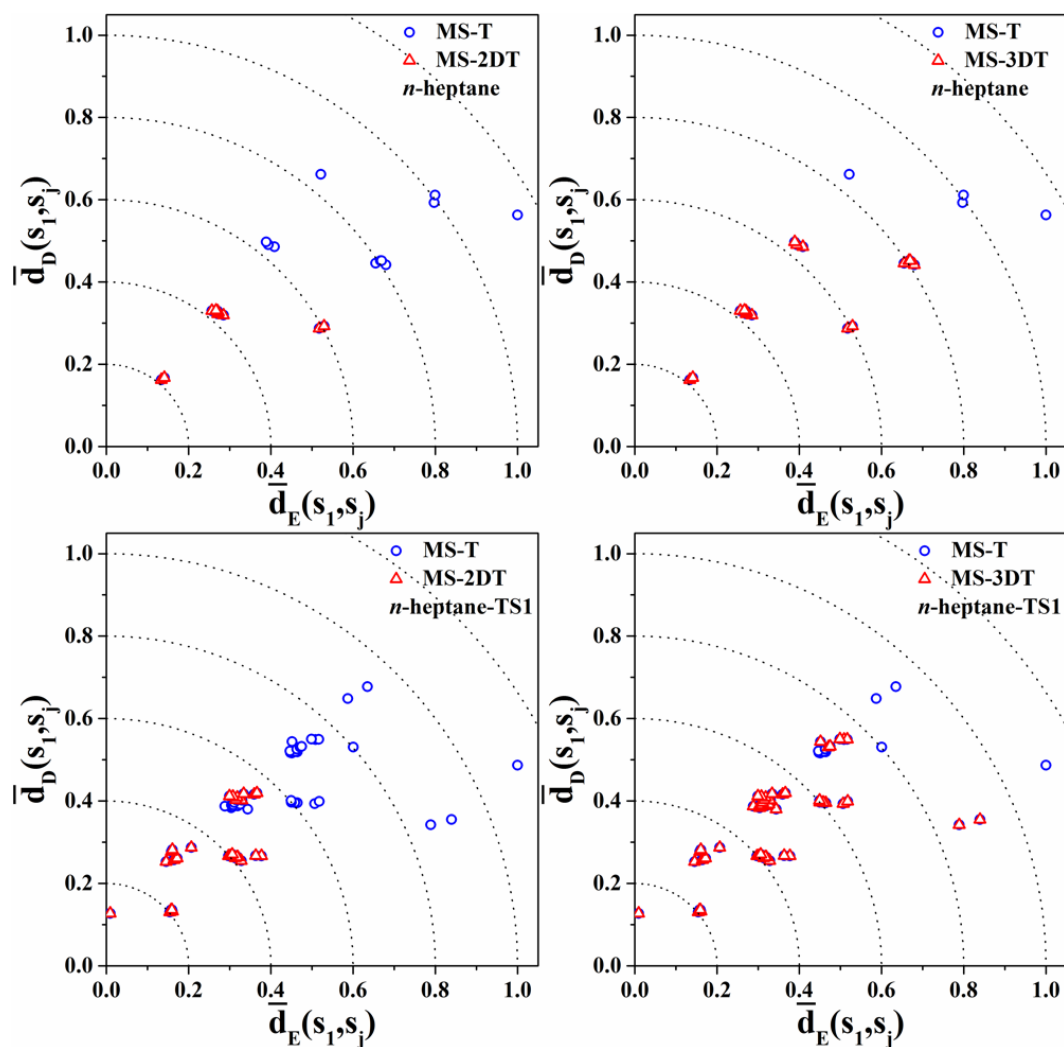


Figure 4.8 Distribution of distinguishable structures (with respect to the lowest energy conformer) in the space of \bar{d}_D and \bar{d}_E using MS-T and MS-nDT methods for *n*-heptane and *n*-heptane-TS1.

To understand the good performance of MS-2DT and MS-3DT, we compared their metric distributions with that of MS-T in Figure 4.8. Again, it is seen that the structures generated by MS-2DT and MS-3DT are concentrated in the region close to the origin

and that the structures of MS-3DT occupy a larger region and therefore generate better predictions than MS-2DT. Consequently, the present metric-based method can be considered as a useful measure to assess the “quality” of a subset for partition function calculation.

4.4 Concluding Remarks

The multi-structural approximation with torsional anharmonicity (MS-T) method proposed by Zheng et al. [38] and the related open-source code MSTor [105, 106] has been proved to be an effective tool for calculating partition functions of large molecules, where the torsional modes are often coupled so that the widely-used one-dimensional hindered rotor (1D-HR) treatment is inapplicable. The MS-T method has a few great advantages such as avoiding evaluating high-dimensional integrals and establishing one-to-one correspondence between the low-frequency torsions and normal modes. But it requires identifying all local minima (and even saddle points) on the torsional potential energy surface, which often results in a huge number of geometry optimization calculations for large molecules. Several variants of MS-T have been proposed to reduce the number of geometry optimization calculations by considering subsets of the complete set of all local minima. The remaining issue to be addressed is that what kinds of subsets can predict the partition function with acceptable accuracy and less computational cost.

In the present work, we proposed a metric-based method to assess the performance of various variants of the MS-T method for calculating conformational-rovibrational

partition function. The central idea of the method is to mathematically quantify the concept of “similarity” of two torsional conformers by defining the dihedral and energy metrics between the two conformers. Consequently, two torsional conformers are “similar” if they have close dihedral and energy metrics. Furthermore, a torsional conformer is considered important in partition function calculation if it is “similar” to the lowest-energy conformer. The underlying physics is based on that those torsional conformers with lower energies have larger contributions to the partition function according to the Boltzmann factor in the definition of the partition function.

We first compared the MS-T method with the proposed MS-2NN method, which can be treated as the simplest variant of the former by considering the coupling of two nearest neighborhood torsions. The results show that the MS-2NN method agrees with the MS-T method in the systems of $n\text{-C}_n\text{H}_{2n+2} + \text{H}$ ($n=6-7$) with computational discrepancies being about a factor of two. In addition, the entropy predictions for $n\text{-C}_n\text{H}_{2n+2}$ ($n=6-10$) by MS-2NN agree with the literature data with errors being generally less than 5%. Considering that MS-2NN method uses a very small subset of the complete set of local minima used in the MS-T method, the above results are astonishing. Our metric-based diagnosis indicates that the local minima including in the subset used by the MS-2NN are close to the origin (representing the lowest-energy conformer) in the space of dihedral and energy metrics.

To verifying the above findings, we also considered the other two variants of the MS-T method, such as the MS-2DT method, which uses a subset of local minima by

considering the coupling of any (unnecessarily nearest) two torsions, and the MS-3DT method, which uses a larger subset of local minima by considering the coupling of any three torsions. As expected, the MS-2DT and MS-3DT methods made increasingly better predictions to the partition functions because they include more local minima “similar” to the lowest-energy conformers.

Overall, the present method provides a mathematically rigorous and computationally effective diagnosis tool to assess various MS-T methods dealing with the torsional anharmonicity of large molecules in partition function calculation. Further validation for more molecules and reaction systems merits future studies. In addition, the metric-based method may play an important role in identifying the Q(partition function)-important torsional conformers without introducing any coupling assumption and when the complete set of local minima is unavailable.

4.5 Appendix

Table S4.1 Structural information (in the ascending order of energy metric) for *n*-hexane-TS1 using the MS-T and MS-2NN (in bold red) methods (units in kcal/mol for energy and degree for dihedral angles).

Structure	Torsion				$d_D(S_1, S_j)$	Energy	$d_E(S_1, S_j)$
	C ⁽²⁾ -C ⁽³⁾	C ⁽³⁾ -C ⁽⁴⁾	C ⁽⁴⁾ -C ⁽⁵⁾	C ⁽⁵⁾ -C ⁽⁶⁾			
S1	179.96	179.90	-179.33	-65.62	0.00	0.00	0.00
S2	180.00	180.00	180.00	-180.00	115.19	0.04	0.04
S3	-179.88	177.05	65.49	175.37	237.21	0.78	0.78
S4	65.81	177.14	179.46	65.46	249.20	0.81	0.81
S5	65.78	177.73	-179.29	-65.06	116.94	0.82	0.82
S6	-179.95	177.24	66.63	63.74	246.16	0.85	0.85
S7	176.87	67.05	177.89	-65.38	118.96	0.85	0.85
S8	176.66	67.10	176.57	65.77	251.59	0.86	0.86
S9	66.11	177.39	-179.92	-179.74	231.05	0.88	0.88
S10	176.78	67.08	177.05	-179.61	233.61	0.91	0.91
S11	-179.80	177.13	66.80	-75.69	126.95	1.10	1.10
S12	175.81	63.23	62.44	174.81	358.62	1.58	1.58
S13	63.16	64.56	176.11	65.83	368.15	1.60	1.60
S14	62.74	64.16	176.75	-65.98	236.22	1.62	1.62
S15	66.18	174.67	66.12	175.72	352.20	1.63	1.63
S16	175.76	63.29	63.29	63.37	367.17	1.64	1.64
S17	66.85	-179.47	-65.80	-175.04	336.70	1.69	1.69
S18	62.98	64.20	176.30	179.81	351.62	1.70	1.70
S19	66.32	174.44	66.99	63.92	360.97	1.72	1.72
S20	65.68	179.06	-67.93	-64.23	227.91	1.75	1.75
S21	176.54	64.27	64.81	-74.88	244.17	1.81	1.81
S22	66.73	175.23	67.78	-75.58	240.74	1.96	1.96
S23	66.59	-179.36	-66.86	76.07	368.27	2.01	2.01
S24	62.76	60.77	62.31	175.55	473.51	2.36	2.36
S25	61.83	60.74	63.18	62.47	482.87	2.40	2.40
S26	62.56	62.23	65.54	-74.63	359.21	2.65	2.65
S27	-178.88	-91.53	64.97	-77.22	217.03	3.55	3.55
S28	-70.12	-92.94	65.39	-76.80	323.54	4.52	4.52

Table S4.2 Structural information (in the ascending order of energy metric) for *n*-hexane-TS2 using the MS-T and MS-2NN (in bold red) methods (units in kcal/mol for energy and degree for dihedral angles).

Structure	Torsion			$d_D(S_1, S_j)$	Energy	$d_E(S_1, S_j)$
	C ⁽²⁾ -C ⁽³⁾	C ⁽³⁾ -C ⁽⁴⁾	C ⁽⁴⁾ -C ⁽⁵⁾			
S1	-179.83	179.93	-179.98	0.00	0.00	0.00
S2	179.90	-178.53	-71.15	110.64	0.54	0.54
S3	66.32	176.62	180.00	117.17	0.86	0.86
S4	-66.29	-177.82	179.80	116.02	0.89	0.89
S5	177.22	67.96	177.95	116.99	0.91	0.91
S6	179.72	177.15	55.34	127.90	0.95	0.95
S7	-176.83	-67.01	-170.43	125.61	1.26	1.26
S8	-176.71	-64.16	-66.89	232.12	1.31	1.31
S9	-66.20	-175.60	-71.13	226.95	1.39	1.39
S10	66.38	178.55	-71.07	224.07	1.45	1.45
S11	63.65	65.58	178.38	232.51	1.69	1.69
S12	66.03	173.47	55.48	245.14	1.84	1.84
S13	-66.92	179.42	55.94	237.51	1.89	1.89
S14	-64.49	-65.52	-170.61	239.27	1.98	1.98
S15	-62.64	-61.76	-67.53	347.95	2.10	2.10
S16	176.42	65.45	48.56	249.69	2.14	2.14
S17	63.53	64.81	50.18	361.60	2.87	2.87

Table S4.3 Structural information (in the ascending order of energy metric) for *n*-hexane-TS3 using the MS-T and MS-2NN (in bold red) methods (units in kcal/mol for energy and degree for dihedral angles).

Structure	Torsion			$d_D(S_1, S_j)$	Energy	$d_E(S_1, S_j)$
	C ⁽²⁾ -C ⁽³⁾	C ⁽³⁾ -C ⁽⁴⁾	C ⁽⁴⁾ -C ⁽⁵⁾			
S1	179.57	179.41	-179.55	0.00	0.00	0.00
S2	-178.45	-73.65	-178.49	109.98	0.58	0.58
S3	179.85	178.52	72.97	108.64	0.64	0.64
S4	67.28	178.77	-179.08	113.41	0.86	0.86
S5	179.98	-175.81	-54.94	129.80	0.92	0.92
S6	176.55	55.38	176.21	131.29	0.94	0.94
S7	-66.66	-170.08	-179.71	124.44	1.26	1.26
S8	-64.17	-68.45	-176.44	231.51	1.35	1.35
S9	-177.91	-67.28	-53.54	241.84	1.43	1.43
S10	176.89	54.68	67.71	240.15	1.48	1.48
S11	67.34	177.06	73.47	221.56	1.50	1.50
S12	68.56	-177.11	-54.63	239.41	1.83	1.83
S13	-66.25	-170.42	75.10	229.69	1.91	1.91
S14	-66.89	-167.21	-55.17	251.30	2.08	2.08
S15	66.20	49.47	175.16	248.59	2.14	2.14
S16	-63.39	-64.74	-53.03	359.42	2.16	2.16
S17	66.14	48.20	66.39	358.69	2.63	2.63

Table S4.4 Structural information (in the ascending order of energy metric) for n -heptane using the MS-T and MS-2NN (in bold red) methods (units in kcal/mol for energy and degree for dihedral angles).

Structure	Torsion				$d_D(S_1, S_j)$	Energy	$d_E(S_1, S_j)$
	C ⁽²⁾ -C ⁽³⁾	C ⁽³⁾ -C ⁽⁴⁾	C ⁽⁴⁾ -C ⁽⁵⁾	C ⁽⁵⁾ -C ⁽⁶⁾			
S1	180.00	180.00	180.00	180.00	0.00	0.00	0.00
S2	179.85	-179.90	177.20	66.11	116.95	0.85	0.85
S3	179.83	176.71	66.32	176.62	120.53	0.89	0.89
S4	179.86	175.94	63.75	62.64	237.81	1.63	1.63
S5	176.95	63.89	63.89	176.95	238.31	1.69	1.69
S6	65.08	176.31	176.31	65.08	237.22	1.71	1.71
S7	66.63	177.25	-177.25	-66.63	232.24	1.72	1.72
S8	177.12	67.17	173.62	66.86	235.23	1.73	1.73
S9	176.76	67.14	179.40	-66.79	229.91	1.81	1.81
S10	175.96	62.77	60.58	62.39	358.30	2.47	2.47
S11	66.18	173.15	64.00	63.20	353.46	2.50	2.50
S12	67.72	-177.38	-62.74	-62.35	349.81	2.59	2.59
S13	175.55	64.65	-93.30	-179.60	206.90	3.29	3.29
S14	62.65	59.07	59.07	62.65	476.57	3.31	3.31
S15	179.40	174.29	64.51	-91.04	210.76	3.36	3.36
S16	178.31	91.13	-66.09	-63.61	320.86	4.15	4.15
S17	66.19	171.96	66.29	-90.24	325.31	4.23	4.23
S18	176.01	63.24	65.12	-90.13	325.50	4.25	4.25
S19	68.05	-176.85	-63.56	93.32	318.22	4.31	4.31
S20	64.62	65.11	-93.72	-69.64	426.90	5.06	5.06
S21	62.59	61.14	66.88	-89.36	440.02	5.07	5.07
S22	63.79	-93.58	-93.58	63.79	405.25	6.34	6.34

Table S4.5 Structural information (in the ascending order of energy metric) for *n*-heptane-TS1 using the MS-T and MS-2NN (in bold red) methods (units in kcal/mol for energy and degree for dihedral angles).

Structure	Torsion					$d_D(S_1, S_j)$	Energy	$d_E(S_1, S_j)$
	C ⁽²⁾ -C ⁽³⁾	C ⁽³⁾ -C ⁽⁴⁾	C ⁽⁴⁾ -C ⁽⁵⁾	C ⁽⁵⁾ -C ⁽⁶⁾	C ⁽⁶⁾ -C ⁽⁷⁾			
S1	-179.89	-179.68	-179.59	-179.97	66.18	0.00	0.00	0.00
S2	180	-180.00	-180.00	-180.00	-180.01	114.67	0.05	0.05
S3	179.86	-180.00	176.95	65.62	175.35	227.60	0.79	0.79
S4	66.09	177.77	-179.84	179.68	65.65	117.70	0.84	0.84
S5	176.67	66.9	176.7	179.42	65.23	122.12	0.85	0.85
S6	179.99	176.75	66.78	175.8	65.21	122.51	0.86	0.86
S7	66.27	177.91	-179.86	-178.36	-65.49	249.78	0.86	0.86
S8	179.77	-179.90	177.45	66.73	63.88	119.12	0.87	0.87
S9	179.91	176.77	66.47	177.41	-65.71	252.20	0.87	0.87
S10	176.71	66.69	176.23	-179.37	-65.70	253.68	0.87	0.87
S11	66.34	177.12	-179.96	179.6	179.93	231.52	0.89	0.89
S12	-179.96	176.84	66.91	176.87	-179.35	234.67	0.92	0.92
S13	176.61	66.43	176.82	179.76	-179.80	235.27	0.93	0.93
S14	179.94	-179.91	177.24	66.96	-75.65	258.46	1.12	1.12
S15	-179.99	176.12	63.57	62.03	175.59	348.54	1.56	1.56
S16	-180.01	176.14	64.11	63.4	63.51	239.89	1.61	1.61
S17	63.37	63.85	175.35	-179.59	-65.86	370.70	1.62	1.62
S18	62.27	62.71	176.71	179.27	65.77	240.31	1.64	1.64
S19	65.73	177.05	176.8	65.41	175.47	345.16	1.65	1.65
S20	66.5	177.27	-177.34	-66.21	-175.38	351.11	1.65	1.65
S21	176.88	67.06	173.8	66.19	176.02	346.77	1.66	1.66
S22	176.03	63.11	63.2	175.5	65.68	243.52	1.66	1.66
S23	176.83	63.62	64.15	178.08	-65.32	369.68	1.67	1.67
S24	62.7	64.19	176.59	179.99	-179.95	351.28	1.68	1.68
S25	175.62	62.79	63.46	176.19	-179.83	356.79	1.69	1.69
S26	66.24	177.36	177.24	66.59	63.94	235.67	1.70	1.70
S27	65.71	176.68	-178.06	-67.41	-64.41	362.72	1.71	1.71
S28	66.51	173.5	67.02	176.41	65.74	237.87	1.72	1.72
S29	66.63	173.51	66.98	177.84	-65.86	367.95	1.73	1.73
S30	176.77	66.85	174.59	67.05	64.08	237.70	1.74	1.74
S31	176.86	67.49	-179.64	-65.75	-174.98	349.17	1.74	1.74
S32	65.77	173.62	66.78	176.65	-179.35	352.52	1.77	1.77
S33	66.66	-179.29	-67.15	-177.43	65.55	229.47	1.78	1.78
S34	66.91	-178.83	-67.04	-176.13	-65.36	361.98	1.78	1.78
S35	176.46	66.38	178.47	-68.47	-64.52	361.72	1.79	1.79
S36	179.92	176.28	64.01	65.35	-74.27	375.76	1.81	1.81

S37	66.78	-179.16	-67.34	-177.16	179.33	342.05	1.87	1.87
S38	66.57	177.48	177.37	66.82	-75.69	374.49	1.95	1.95
S39	66.42	177.1	-177.33	-67.62	75.42	240.75	1.97	1.97
S40	176.55	66.79	173.57	67.54	-74.95	377.53	1.99	1.99
S41	176.85	67.31	-179.83	-66.41	76.35	240.22	2.05	2.05
S42	175.97	62.83	59.9	62.04	175.21	469.14	2.43	2.43
S43	62.84	63.56	173.1	65.39	175.81	465.60	2.43	2.43
S44	176.13	62.67	60.87	63.23	62.87	361.28	2.44	2.44
S45	62.59	60.89	63.81	176.58	66.21	357.01	2.44	2.44
S46	66.14	172.96	63.62	62.53	175.02	464.45	2.45	2.45
S47	62.23	60.35	63.01	177.66	-65.62	489.42	2.45	2.45
S48	66.04	173.17	63.73	63.62	63.63	356.85	2.49	2.49
S49	62.83	63.66	178.23	-66.48	-175.54	467.86	2.50	2.50
S50	66.97	-178.24	-63.51	-62.73	-174.82	466.90	2.52	2.52
S51	63.25	64.07	173.21	66.74	63.68	356.10	2.52	2.52
S52	62.25	60.09	63.39	176.19	-179.68	473.07	2.52	2.52
S53	62.96	64.2	179.2	-67.25	-64.45	477.82	2.56	2.56
S54	67.9	-176.49	-62.26	-62.70	-63.06	479.24	2.58	2.58
S55	175.93	63.77	62.58	64.68	-75.29	495.36	2.71	2.71
S56	66.6	-179.18	-65.09	-64.14	75.72	353.89	2.75	2.75
S57	62.89	64.11	173.45	67.73	-75.32	494.19	2.77	2.77
S58	65.31	170.73	64.94	66.35	-75.15	494.86	2.81	2.81
S59	62.16	64.31	-179.61	-65.81	77.24	359.20	2.81	2.81
S60	62.21	60.41	60.43	62.48	174.54	583.69	3.19	3.19
S61	62.87	60.06	60.53	62.99	63.11	477.48	3.26	3.26
S62	62.47	60.97	62.77	65.83	-74.65	609.65	3.45	3.45
S63	179.72	-72.66	-100.45	62.41	62.4	307.97	4.28	4.28
S64	179.35	71.5	94.81	-64.97	75.49	319.48	4.56	4.56
S65	66.07	68.7	92.89	-66.35	77.52	438.13	5.43	5.43

Table S4.6 Structural information (in the ascending order of energy metric) for *n*-heptane-TS2 using the MS-T and MS-2NN (in bold red) methods (units in kcal/mol for energy and degree for dihedral angles).

Structure	Torsion				$d_D(S_1, S_j)$	Energy	$d_E(S_1, S_j)$
	C ⁽²⁾ -C ⁽³⁾	C ⁽³⁾ -C ⁽⁴⁾	C ⁽⁴⁾ -C ⁽⁵⁾	C ⁽⁵⁾ -C ⁽⁶⁾			
S1	179.98	179.84	-179.95	179.87	0.00	0.00	0.00
S2	179.92	-179.94	178.56	71.24	110.40	0.53	0.53
S3	-66.27	-177.13	-179.81	-179.21	117.85	0.84	0.84
S4	65.89	177.90	-179.44	-179.44	117.23	0.86	0.86
S5	176.83	66.92	177.33	-179.92	119.01	0.89	0.89
S6	-176.40	-66.85	-176.88	-179.73	120.40	0.89	0.89
S7	179.74	-178.01	-68.32	-178.50	115.66	0.90	0.90
S8	179.99	-179.81	-177.19	-55.60	127.66	0.94	0.94
S9	179.93	176.69	66.89	169.96	126.27	1.27	1.27
S10	-179.99	176.82	64.70	66.26	232.01	1.31	1.31
S11	66.58	177.58	178.66	71.42	225.50	1.38	1.38
S12	-66.72	-177.01	178.04	71.78	226.55	1.39	1.39
S13	176.78	66.54	174.58	71.08	230.76	1.40	1.40
S14	-176.67	-66.99	-178.46	71.29	226.58	1.45	1.45
S15	-62.78	-63.70	-176.19	180.00	237.59	1.63	1.63
S16	62.86	63.58	175.27	179.78	238.25	1.64	1.64
S17	-176.15	-63.43	-63.76	-176.62	240.30	1.72	1.72
S18	-66.37	-174.47	-67.36	-176.89	235.18	1.75	1.75
S19	-66.14	-177.40	-177.68	-56.78	242.27	1.78	1.78
S20	66.24	179.66	-69.15	-177.96	226.90	1.80	1.80
S21	66.46	177.53	-176.61	-55.72	243.59	1.80	1.80
S22	-176.92	-67.06	-173.85	-56.23	246.20	1.81	1.81
S23	176.59	68.10	-179.15	-55.71	240.36	1.91	1.91
S24	176.26	63.92	65.78	171.93	241.84	1.95	1.95
S25	66.51	174.32	67.43	170.35	241.12	2.11	2.11
S26	176.64	63.82	61.61	66.31	351.36	2.13	2.13
S27	66.01	173.68	64.89	67.65	347.52	2.13	2.13
S28	179.80	-177.46	-65.68	-48.66	248.63	2.15	2.15
S29	-66.90	178.54	66.55	169.72	238.06	2.17	2.17
S30	62.71	63.76	174.54	70.93	347.79	2.17	2.17
S31	-62.47	-64.34	-179.44	70.26	343.49	2.18	2.18
S32	-66.51	179.50	64.80	66.33	342.65	2.19	2.19
S33	-62.40	-61.04	-64.41	-177.41	355.00	2.51	2.51
S34	-63.20	-64.08	-172.69	-55.70	364.59	2.62	2.62
S35	63.34	66.13	-178.74	-55.28	356.41	2.66	2.66
S36	61.89	62.43	66.84	171.52	357.07	2.79	2.79

S37	-176.06	-63.71	-63.67	-49.23	367.60	2.84	2.84
S38	62.40	60.55	60.89	66.43	469.47	2.86	2.86
S39	-66.43	-172.99	-66.64	-49.80	364.41	2.96	2.96
S40	66.25	-179.27	-65.86	-48.73	360.12	3.04	3.04
S41	-62.65	-61.78	-64.24	-49.76	481.84	3.70	3.70

Table S4.7 Structural information (in the ascending order of energy metric) for *n*-heptane-TS3 using the MS-T and MS-2NN (in bold red) methods (units in kcal/mol for energy and degree for dihedral angles).

Structure	Torsion				$d_D(S_1, S_j)$	Energy	$d_E(S_1, S_j)$
	C ⁽²⁾ -C ⁽³⁾	C ⁽³⁾ -C ⁽⁴⁾	C ⁽⁴⁾ -C ⁽⁵⁾	C ⁽⁵⁾ -C ⁽⁶⁾			
S1	179.90	-179.71	-179.93	179.56	0.00	0.00	0.00
S2	-179.97	177.89	72.41	177.44	112.31	0.58	0.58
S3	179.94	179.85	-178.56	-73.19	109.11	0.64	0.64
S4	-66.45	-176.52	-179.63	179.24	117.46	0.85	0.85
S5	66.09	178.00	-179.54	179.37	116.67	0.88	0.88
S6	-177.76	-68.14	-178.41	179.11	115.87	0.90	0.90
S7	179.45	179.84	175.54	54.79	130.19	0.92	0.92
S8	-179.41	-176.16	-54.95	-176.46	133.20	0.95	0.95
S9	176.92	66.85	169.27	179.58	127.24	1.28	1.28
S10	176.82	64.00	68.70	177.27	233.03	1.35	1.35
S11	179.98	176.67	68.79	54.00	240.54	1.40	1.40
S12	66.58	175.74	73.72	177.98	225.79	1.41	1.41
S13	-66.45	-179.01	73.40	177.75	222.84	1.45	1.45
S14	-179.46	-175.71	-53.93	-67.45	243.64	1.47	1.47
S15	65.79	176.95	-178.44	-73.44	225.94	1.47	1.47
S16	-65.96	-176.58	-178.43	-72.85	226.35	1.47	1.47
S17	-177.57	-68.37	-176.65	-73.24	224.36	1.51	1.51
S18	-63.88	-64.68	-176.10	179.36	235.27	1.69	1.69
S19	66.29	177.50	176.82	54.85	244.36	1.77	1.77
S20	-66.65	-177.12	176.05	54.82	244.80	1.79	1.79
S21	-66.12	-174.15	-56.31	-176.23	247.38	1.81	1.81
S22	-177.74	-69.70	176.74	54.49	240.78	1.86	1.86
S23	67.62	-178.15	-55.18	-176.06	242.97	1.89	1.89
S24	176.67	66.86	170.24	-75.11	231.83	1.92	1.92
S25	63.98	66.22	170.21	179.85	240.14	1.94	1.94
S26	177.14	67.67	166.73	55.59	252.68	2.09	2.09
S27	62.74	61.77	69.39	176.95	348.97	2.14	2.14
S28	-177.19	-65.94	-48.13	-175.54	253.40	2.15	2.15
S29	177.06	64.23	65.06	53.77	359.69	2.18	2.18
S30	-66.11	-178.69	67.26	53.24	354.14	2.23	2.23
S31	66.67	174.81	68.89	53.85	355.59	2.26	2.26
S32	-63.35	-64.85	-175.11	-72.79	344.08	2.30	2.30
S33	-66.28	-173.71	-55.13	-68.01	357.05	2.33	2.33
S34	66.64	-179.23	-54.22	-67.00	352.89	2.41	2.41
S35	64.16	64.82	168.61	-75.75	347.37	2.61	2.61
S36	-176.52	-65.79	-48.77	-67.57	361.54	2.63	2.63

S37	-63.78	-65.69	178.87	55.24	355.86	2.65	2.65
S38	64.18	65.28	166.59	55.35	368.41	2.79	2.79
S39	-64.18	-65.61	-49.62	-174.42	366.36	2.91	2.91
S40	62.75	60.81	64.54	53.79	477.93	2.96	2.96
S41	-64.36	-64.49	-48.21	-67.17	475.95	3.41	3.41

Table S4.8 Structural information (in the ascending order of energy metric) for *n*-heptane-TS4 using the MS-T and MS-2NN (in bold red) methods (units in kcal/mol for energy and degree for dihedral angles).

Structure	Torsion				$d_D(S_1, S_j)$	Energy	$d_E(S_1, S_j)$
	C ⁽²⁾ -C ⁽³⁾	C ⁽³⁾ -C ⁽⁴⁾	C ⁽⁴⁾ -C ⁽⁵⁾	C ⁽⁵⁾ -C ⁽⁶⁾			
S1	179.57	179.87	-179.88	-179.58	0.00	0.00	0.00
S2	179.86	178.30	73.58	178.30	110.54	0.59	0.59
S3	179.94	179.27	-178.29	-67.16	114.98	0.87	0.87
S4	179.62	-176.31	-55.60	-176.78	130.94	0.96	0.96
S5	179.59	-179.97	170.38	66.73	123.62	1.28	1.28
S6	179.67	176.68	69.26	64.23	230.35	1.34	1.34
S7	175.69	53.71	67.54	177.29	245.75	1.44	1.44
S8	-178.53	-74.10	-177.08	-67.81	222.50	1.47	1.47
S9	67.23	177.90	-177.89	-67.22	228.66	1.74	1.74
S10	176.44	54.90	176.69	-68.51	242.61	1.88	1.88
S11	-179.15	-76.22	170.30	66.68	228.77	1.91	1.91
S12	177.45	56.29	166.61	66.66	252.99	2.11	2.11
S13	179.91	-173.96	-49.18	-66.31	250.46	2.12	2.12
S14	66.16	177.40	169.72	65.80	240.90	2.13	2.13
S15	176.90	54.07	64.66	63.34	361.02	2.17	2.17
S16	68.02	175.86	69.98	64.05	342.08	2.22	2.22
S17	-177.31	-68.09	-48.87	-65.79	359.96	2.60	2.60
S18	-65.76	-170.09	73.11	64.91	347.23	2.66	2.66
S19	-66.96	-169.16	169.16	66.96	248.87	2.74	2.74
S20	68.13	-175.46	-48.58	-65.69	361.30	3.08	3.08
S21	65.31	48.86	65.39	63.67	476.75	3.35	3.35
S22	65.69	49.17	166.03	67.60	371.50	3.41	3.41

Chapter 5 Approximation of Torsional Potential Energy Surface Reconstructed by Voronoi Tessellation

5.1 Introduction

Evaluation of partition functions is challenging for thermochemical calculations on complex molecules [34, 123-125]. This is because torsional modes within a complex molecule containing various functional groups are often strongly coupled (SC), and the involved torsional anharmonicity [38, 126] would result in the harmonic approximation [95, 127] being highly inaccurate. A variety of studies [96, 100] employ one-dimensional (1D) internal rotation treatments to replace the harmonic contributions by a specific torsional mode, however, it is often difficult to identify strongly coupled torsions with specific normal modes [102]. Then, it spawned the non-separable treatments of mixed torsions. The widely discussed Pitzer-Gwinn approximations [36], Feynman path integrals [128], and Monte Carlo phase space integrals [129] have been used but they are usually computational expensive and unaffordable for complex molecules.

As mentioned in Chapter 4, Zheng et al. [38] proposed a class of multi-structural (MS) method that could satisfactorily with the torsional anharmonicity, in which the MS-AS (the former name of MS-T) denoting “multi-structural method including all structures” is particularly of interests because it does not require any information about conformational barriers or the paths that connect various structures. We noted that the torsional anharmonicity results in an “almost periodic function” of potential energy on

the parameter space of dihedral angles corresponding to the torsional modes. The MS-AS method invokes an essential approximation by expressing such a potential energy function as a summation of several local periodic functions. It means that the constructed potential energy surface (PES) along a specific dihedra angle is always symmetric on two sides of each local minimum. This approximation becomes increasingly inaccurate when torsional modes present non-uniformly distributed local energy minima. In the present study, we attempt to theoretically analyze the uncertainties of the MS-AS method and to propose improved methods for reconstructing approximate PES based on the mathematical technique of Voronoi tessellation.

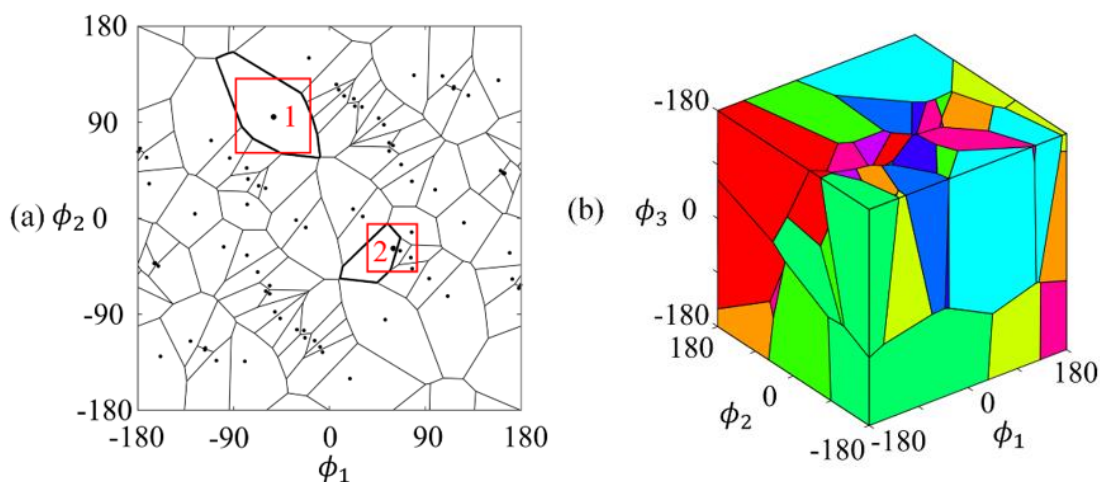


Figure 5.1 Schematic (a) 2D and (b) 3D Voronoi tessellation generated from the presently calculated 78 conformational structures of transition state in the hydrogen abstraction of MB (methyl butanoate) by HO_2 radical.

5.2 Theoretical methods

To deal with the torsional anharmonicity induced by SC torsional modes, the MS-AS method [38] uses Voronoi tessellation [108] to identify the influence region for each conformational structure on the parameter space of dihedral angles so as to circumvent

the difficulties of assigning coupled torsions to specific normal modes. Voronoi tessellation cuts the entire parameter space into several one-by-one subspaces to each local minimum (solid points) and guarantees every point in a subspace is nearest to its corresponding local minimum than other minima, as shown in Figure 5.1. It can be mathematically described as that, for each structure (point) j , its influence region $R(j)$ is defined as

$$R(j) = \{x \in X | d(x, j) \leq d(x, k), \text{ for all } j \neq k\} \quad (5.1)$$

where x is a point in the parameter space X , and d the distance metric. The Euclidean norm is generally used as the default distance metric. The periodic replicas are also included in the tessellation calculation so that could properly handle the periodic nature of the torsional modes. To physically reflect the influence region for each structure, a multiplicatively weighted Voronoi diagram [130] be used in the present study. More details about the mathematical theory of Voronoi tessellation can be found in [108, 130].

Voronoi tessellation and reconstruction of PES require information from electronic structure calculations. In the present study, all conformational structures with local potential energy minima can be identified by internal torsions from an initial structure (generally a lowest energy state). Density functional theory (DFT) employing the B3LYP functional with the 6-311++G(d,p) basis set [71] was used for geometry optimization, frequency calculation, and zero-point energy correction. All the calculations were performed by the Gaussian 09 program package [78].

5.3 Results and Discussion

5.3.1 Uncertainty Analysis of MS-AS Method

The MS-T method has been detailed in Chapter 4. The periodic potential assumption of Eq. (4.4) in the MS-AS method is conditionally accurate if the local minima are uniformly distributed with same energies and frequencies. As the 1D example shown in Figure 5.2, the potential $V_1/\text{cm}^{-1} = 750 \cos(2\phi) + 750$ is a periodic function with the periodicity of 180° . Then it can be divided into two identical periodic functions that corresponding to two local minima, respectively, in which each periodic function traverses a complete period of 180° .

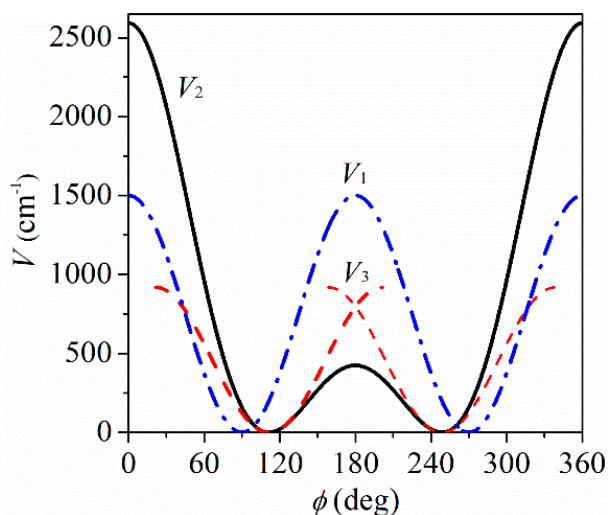


Figure 5.2 Potentials of a periodic function V_1 , an almost periodic function V_2 (corresponding to H_2O_2), and piecewise periodic functions V_3 that constructed in the MS-AS method.

The exact potential is generally not a periodic function if existing the torsional anharmonicity, as the 1D torsional potential for H_2O_2 [131] that the potential $V_2/\text{cm}^{-1} = 830.7 + 1037.4 \cos(\phi) + 674.2 \cos(2\phi) + 46.9 \cos(3\phi) + 2.7 \cos(4\phi)$ is an almost periodic function with a permanent periodicity of 360°

because of the natural torsion, as shown in Figure 5.2. The MS-AS method splits the potential V_2 into two piecewise periodic functions V_3 that corresponding to two local minima. According to Eq. (4.4) and (4.5) with the periodicity parameter $M = 2$, the internal moment of inertia $I = 0.4232 \text{ amu \AA}^2$, and the harmonic frequency $\omega = 382.6 \text{ cm}^{-1}$ for both two minima, the reconstructed potential V_3 is also shown in Figure 5.2. It is seen that the potential curve V_3 is always symmetric on two sides of the local minimum with same barrier heights, which causes the potential to be one side higher and the other side lower than the exact potential. It is also found an overlapped region between two neighboring periodic functions. Consequently, the periodic potential assumption properly leads to inaccurate estimation of the partition function, which is believed to be increasingly exacerbated when the local minima become more non-uniformly distributed.

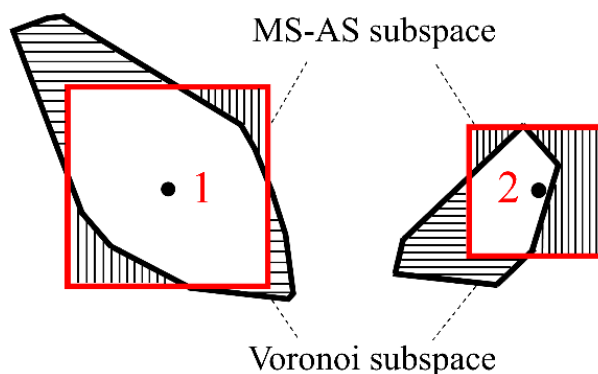


Figure 5.3 Closeup of Voronoi subspace and constructed MS-AS subspace in Figure 5.1.

The uncertainty of the MS-AS method becomes prominent when considering SC torsions. As the red frame of representative structures 1 and 2 shown in Figure 5.1(a), the constructed subspace in the MS-AS method is a square for 2D and a cube for 3D

coupled torsions. From a closeup of structure 1 shown in Figure 5.3, we can infer that the Voronoi subspace and the constructed MS-AS subspace contribute approximately equally on the partition function for those structures with local minimum located almost centrally. However, for those structures whose local minima are very close to the boundary of their Voronoi cells, for example structure 2, the periodic potential assumption in the MS-AS method would induce highly inaccurate partition function estimation. This can be understood by a closeup of structure 2, as shown in Figure 5.3. Apart from the overlapped white region, the shade region denoted by vertical lines of isotropic subspace is closer to the local minimum than that denoted by horizontal lines of Voronoi subspace, and thereby has a lower potential energy V and a high partition function $Q \sim e^{-V/k_B T}$. It is predicted that the deviations of partition function estimation between the MS-AS method and the exact value would be increasingly enlarged when considering three SC torsions in the transition state involving extremely non-uniformly distributed local minima.

5.3.2 Improved Reconstruction of Torsional PES

Considering the uncertainties of the MS-AS method, we considered to relax the assumption of the periodic potential and to obtain a physically reliable potential. We noted that a higher-level MS method (MS-ASCB) [38] has been introduced and ASCB denotes “based on all structures and conformational barriers”. It includes the explicit conformational barrier heights and positions obtained from electronic structure calculations, and hence the continuous torsional potential can be given as

$$V_{j,\tau} = \begin{cases} U_j + \frac{W_{j,\tau}^L}{2} \left[1 - \cos \left(\frac{(\phi_\tau - \phi_{\tau,\text{eq},j})\pi}{(\phi_{\tau,\text{eq},j} - \phi_{j,\tau}^L)} \right) \right], & (\phi_{j,\tau}^L \leq \phi_\tau \leq \phi_{\tau,\text{eq},j}) \\ U_j + \frac{W_{j,\tau}^R}{2} \left[1 - \cos \left(\frac{(\phi_\tau - \phi_{\tau,\text{eq},j})\pi}{(\phi_{j,\tau}^R - \phi_{\tau,\text{eq},j})} \right) \right], & (\phi_{\tau,\text{eq},j} \leq \phi_\tau \leq \phi_{j,\tau}^R) \end{cases} \quad (5.2)$$

where $W_{j,\tau}^L$ and $W_{j,\tau}^R$ are the exact left and right barrier heights along torsion τ of structure j , and $\phi_{j,\tau}^L$ and $\phi_{j,\tau}^R$ are their corresponding barrier positions. Theoretically, the MS-ASCB method can provide more reliable potential than the MS-AS method. However, the additionally required information of barrier heights and positions would cause a significant amount of computational cost and human efforts. Consequently, it is quite compelling to think of a more physical potential to replace the periodic potential in the MS-AS method because the information of barrier positions and heights are reflected by the shape and boundary of the Voronoi tessellation.

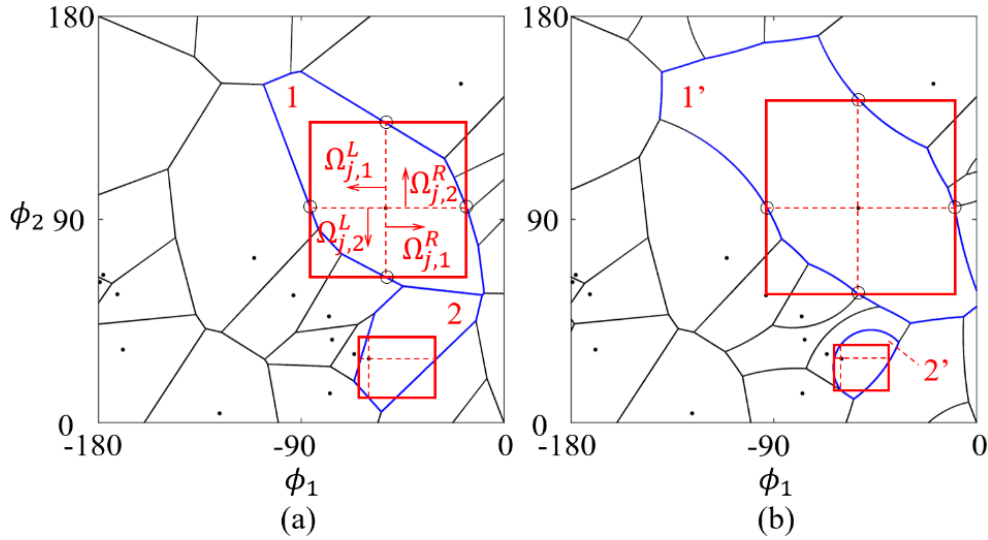


Figure 5.4 A closeup of upper left corner of Figure 5.1(a) which shows the improvements of the MS-AS method with corrected (a) barrier heights based on original Voronoi diagram and (b) barrier positions based on multiplicatively weighted Voronoi diagram.

We attempt to reconstruct an almost periodic function of potential based on the

Voronoi tessellation in two steps. First, we assume that the barrier positions are at the boundaries of Voronoi cells, and then calculate the barrier heights according to Eq. (4.5) by defining another two periodicity parameters, $M_{j,\tau}^L$ and $M_{j,\tau}^R$, which are related to $M_{j,\tau}$. As a result, we can characterize the asymmetric barrier positions and heights for the local minimum. Second, recognizing that barrier positions tend to vary with the energy and frequency of the local minimum, we define a structure-related distance metric to recalculate the Voronoi tessellation and to obtain the corrected barrier positions and heights.

Specifically, the left and right boundaries of Voronoi cells in each torsion, $\phi_{j,\tau}^L$ and $\phi_{j,\tau}^R$, are assumed as the exact barrier positions, which are already determined from the Voronoi tessellation, as the hollow intersection points of blue Voronoi subspace and red MS-AS subspace shown in Figure 5.4(a). The local periodicity parameter $M_{j,\tau}$ for each structure is equivalent in every torsion and determined by Eq. (4.7). Then, to characterize the barrier height difference on the left and right sides of the local minimum in each torsion, we define two periodicity parameters, $M_{j,\tau}^L$ and $M_{j,\tau}^R$, by

$$M_{j,\tau}^L \Omega_{j,\tau}^L = M_{j,\tau}^R \Omega_{j,\tau}^R \quad (5.3)$$

$$(M_{j,\tau}^L)^2 + (M_{j,\tau}^R)^2 = 2M_{j,\tau}^2 \quad (5.4)$$

where $\Omega_{j,\tau}^L$ and $\Omega_{j,\tau}^R$ are the hypervolumes obtained by cutting the subspace into “left” and “right” parts with a specific plane, in which the specific plane is perpendicular to the torsion axis and across the internal coordinate $\phi_{j,\tau}$ of the local minimum, as shown in Figure 5.4(a). Subsequently, we can obtain the corrected barrier heights, $W_{j,\tau}^L$ and

$W_{j,\tau}^R$, by Eq. (4.5), and the almost periodic potential by Eq. (5.2).

In general cases, the barrier positions are not exactly at the boundaries of Voronoi cells, since the Voronoi tessellation topologically divides the space merely in geometry by assuming all structures contribute equally to the total potential. But in fact, the barrier positions would change as varying the energy and the frequency of each local minimum. Physically, for the ideal states of evenly distributed local minima with same energies and frequencies, the exact barrier positions should be completely located at the boundaries of Voronoi cells. However, for the general states involving frequency and energy differences between neighboring structures, the barrier positions tend to be closer to those minima with higher frequencies or higher energies. Based on this understanding, we define a new structure-related distance metric as $d_{j,\tau}^1 = \varepsilon_{j,\tau} d_{j,\tau}^0$, where $d_{j,\tau}^0$ is the distance metric that used in the original Voronoi tessellation. The correction coefficient $\varepsilon_{j,\tau}$ is defined as

$$\varepsilon_{j,\tau} = \frac{d_{j,\tau}^1}{d_{j,\tau}^0} = \frac{U_j + \frac{2I_{j,\tau}\omega_{j,\tau}^2}{M_{j,\tau}}}{\frac{1}{N} \sum_{j=1}^N \left(U_j + \frac{2I_{j,\tau}\omega_{j,\tau}^2}{M_{j,\tau}} \right)} \quad (5.5)$$

to reflect the synergetic effects of frequency and energy changing on the variation of barrier positions. A weighted correction coefficient ε_j is defined as the root mean square of all concerned torsions $\varepsilon_{j,\tau}$. Eq. (5.5) shows that either increasing U_j or $\omega_{j,\tau}$ would result in an increased $\varepsilon_{j,\tau}$ and $d_{j,\tau}^1$, and thereby a reduced hypervolume of Voronoi subspace j . This can be clearly shown by the multiplicatively weighted Voronoi diagram in Figure 5.4(b) that the Voronoi cells for structure 1' ($\varepsilon_1 = 0.5$)

and 2° ($\epsilon_2 = 1.3$) are enlarged and reduced, respectively. Furthermore, for any two neighboring local minima with same U_j and $\omega_{j,\tau}$, their $\epsilon_{j,\tau}$ are the same (but not has to be 1) so that the original boundaries of Voronoi cells are not changed.

The proposed improved method is named as MS-ASB, where B denotes the corrected “barrier heights and positions” by information of Voronoi tessellation. It is noted that, for 1D case, the potential integration of Eq. (4.3) is performed in Voronoi subspace rather than the constructed isotropic subspace in the original MS-AS method. Whereas, for high dimensional cases, the potential integration is performed in a rectangle subspace, as the red frame shown in Figure 5.4(a), rather than the Voronoi subspaces (arbitrary polygon) owing to the separability assumption of potential in each coupled torsion.

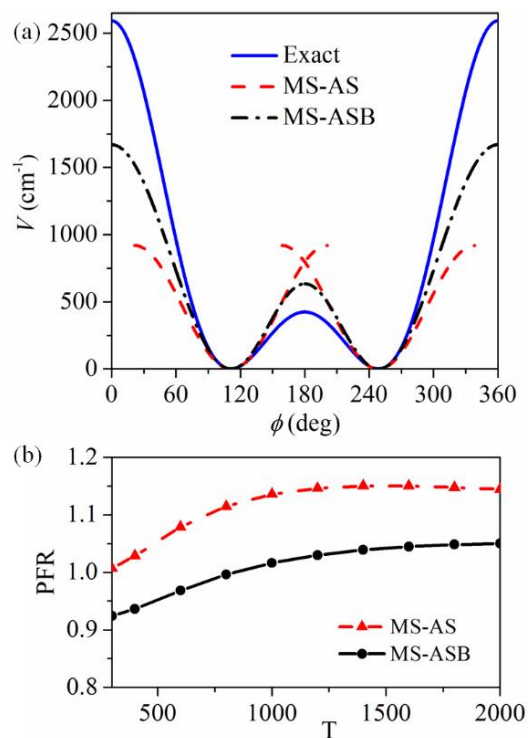


Figure 5.5 Comparison of (a) the potential curve and (b) partition function ratio (PFR) of the 1D torsional mode of H_2O_2 [38].

5.3.3 Validation Testing Cases by MS-ASB

In the present study, the improved MS-ASB method was validated against a few test cases. Here, a 1D torsional potential of H_2O_2 , a 2D 1-pentyl radical, and a 3D 1-butanol radical were chosen for better illustration.

The first testing case is the 1D torsion potential of H_2O_2 [38] that has been discussed in Figure 5.2. Owing to the symmetric distribution of local minima, the exact barrier positions are just at the boundaries of Voronoi subspaces. As shown in Figure 5.5(a), the reconstructed almost periodic function of potential by the MS-ASB method is more physically reliable than the symmetric potential by the MS-AS method. Figure 5.5(b) shows the PFR with partition functions normalized by the exact value. The MS-AS method overestimates the partition function. However, the improved MS-ASB method can reduce the overestimation by a factor of 1.2 and obtain an accurate estimation of partition function that closer to the exact value particularly at high temperatures, regardless of some deviations at low temperature. This might be attributed to the slightly larger barrier height estimated by MS-ASB.

The second testing case is the 2D torsional mode of 1-pentyl radical with 15 conformational structures [38]. The comparison of PFR with partition functions normalized by the value calculated by the multi-structural harmonic-oscillator (MS-HO) method, due to the lack of exact value, as shown in Figure 5.6(a). The PFR of the MS-ASB method is about one-order smaller than that of the MS-AS method because of the extremely non-uniform distribution of local energy minima. The validation

substantiates our motivation for the present theoretical work that the improvement of the MS-ASB method is increasingly significant for the larger non-uniform distribution of the local minima in complex molecules. Geometrically, the weighted Voronoi tessellation in the MS-ASB method can modify the original “banded” Voronoi subspace in the MS-AS method to a more “round” subspace with the local minima located centrally, as shown in Figure 5.6(b)-(c).

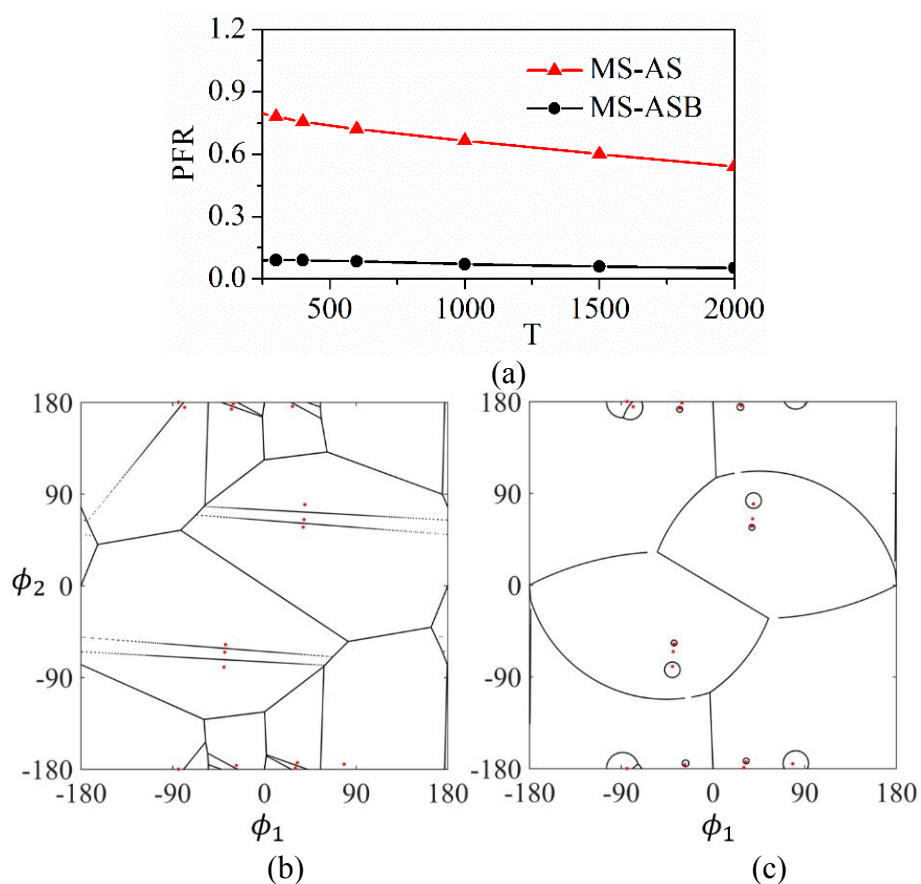


Figure 5.6 Test of the 2D torsional mode of 1-pentyl radical [38]. (a) comparison of partition function (PFR). Schematic of the (b) original Voronoi diagram by MS-AS method and (c) weighted Voronoi diagram by MS-ASB method.

The third testing case is the 3D torsional mode of 1-butanol radical with 29 conformational structures [38]. It is seen that, as show in Figure 5.7(a), the difference of PFR between the MS-AS and MS-ASB methods is not continuously enlarged by

considering more coupled torsions when compared to that in Figure 5.6(a) of 2D torsional mode of 1-pentyl radical. This is probably owing to the relatively uniform distribution of the local energy minima shown in Figure 5.7(b). It implies that the improvement of the MS-ASB method mainly relies on the larger non-uniform distribution of the local minima as discussed in Figure 5.6(b)-(c) rather than by considering more coupled torsions.

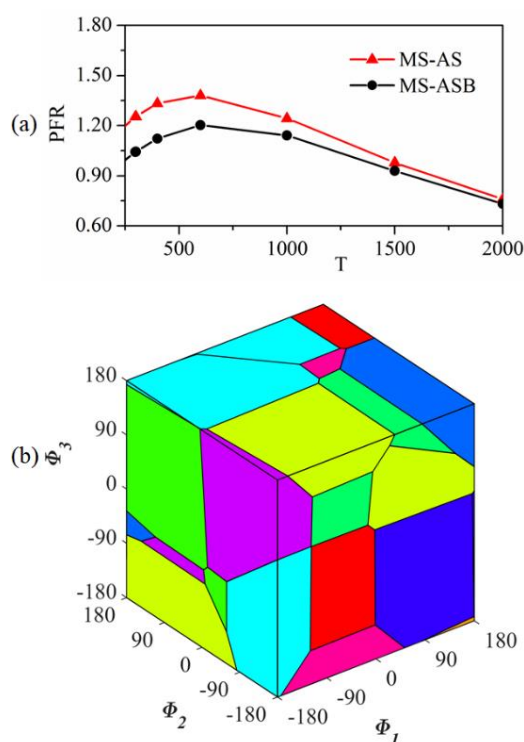


Figure 5.7 Test of a 3D torsional mode of 1-butanol radical. (a) comparison of partition function ratio and (b) schematic of weighted Voronoi diagram.

In summary, both the theoretical analysis and all numerical results show that the MS-AS method tends to overestimate the partition function, but the proposed MS-ASB method can reduce the possible overestimation by a factor that depends on the specific chemical system. Furthermore, the proposed MS-ASB method does not cause much additional cost because all the parameters used in it are obtained from the Voronoi

Tessellation, which is the required procedure for other MS-based methods.

5.4 Concluding Remarks

Motivated by the observations that the widely-used MS-AS method to deal with the torsional anharmonicity often overpredicts partition functions of complex molecular system, we performed an uncertainty analysis to show that its periodic potential assumption would result in inaccurate estimation of partition function when torsional modes present non-uniformly distributed local energy minima. To remedy this problem, we proposed an improved MS-ASB method to reconstruct an almost periodic function of potential to replace the periodic potential based on the Voronoi tessellation of local minima. The proposed MS-ASB method can be treated as an intermediate method, which aims to have the comparable computational cost to the MS-AS method but to have computational accuracy approximate to that of the MS-ASCB method. The proposed method has been validated by several testing cases. The results show that the effectiveness of the MS-ASB method becomes increasingly substantial when addressing the torsional anharmonicity problem with extremely non-uniformly distributed local minima. The validation by comparing with other theoretically appealing methods or with experiments will be considered in the future work once the proposed MS-ASB method and its future improvements have been proved to be as accurate as possible to the MS-ASCB method.

Part 2

Experimental Study of Coupled Flickering Buoyant Diffusion Flames

Chapter 6 Background and Motivation

6.1 Flickering Diffusion Flames

Diffusion flames are ubiquitous in nature (e.g. wildland and urban fires), industrial applications (e.g. gas-turbine and rocket engines), and domestic application (e.g. fireplaces and furnaces). In combustion, a diffusion flame [132, 133] is that a flame in which the fuel and oxidizer are initially and spatially separated before burning, and Burke and Schumann [132] first applied the term “diffusion flame” for the class of flame in 1928. It is often referred to as a non-premixed flame to differentiate it from the premixed flame in which the fuel and oxidizer are mixed before burning.

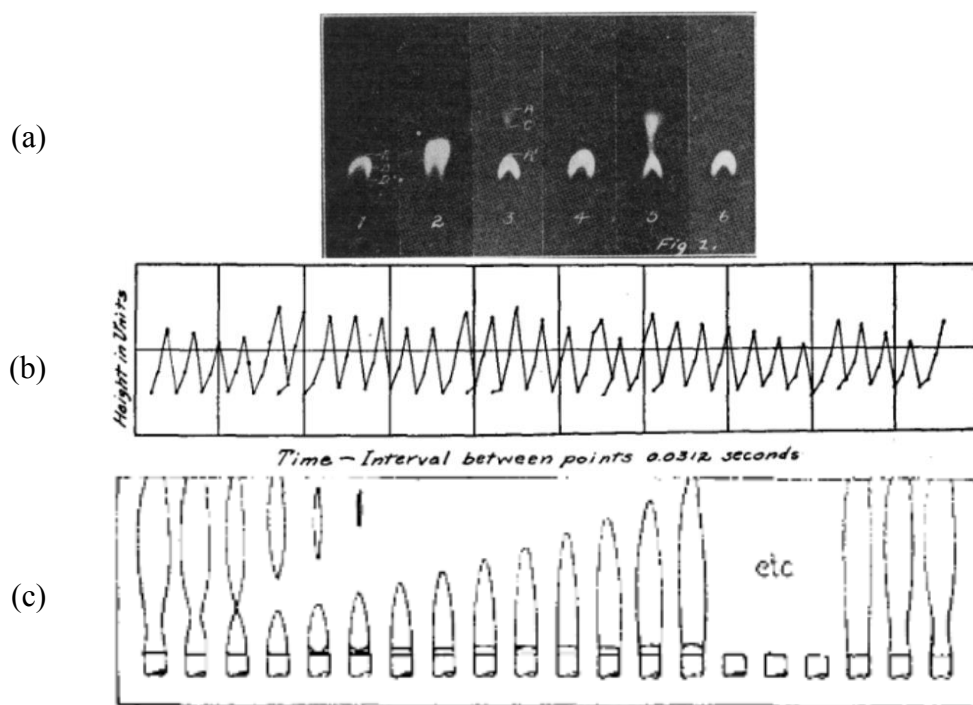


Figure 6.1 (a) Experimental photographs of flickering of diffusion flame, (b) the time series of the flame height [134], and (c) the progressive necking process of flickering diffusion flame [135].

Vibratory motion of Bunsen-type natural gas/air diffusion flames was observed and referred to as “the flicker of luminous flames” by Chamberlin and Rose [134], as shown

in Figure 6.1(a), and they found “the upper portion of the luminous zone rises to a maximum height ten times per second”, as shown in Figure 6.1(b), and it was found the “vibration rate” which is referred to as oscillation frequency is not affected largely by outside conditions. Subsequently, Barr [135] also discovered the similar phenomena in butane/air diffusion flame, in which butane flame vibrates about 20 cycles per second between the maximum and minimum positions and the vibration motion seemed like a progressive necking process of the flame which can lead to the formation of a flame bubble that would burn itself out when it separated from the anchored flame, as shown in Figure 6.1(c). Similar phenomena were also observed in pool fires and often referred to as “puffing flames” [136, 137].

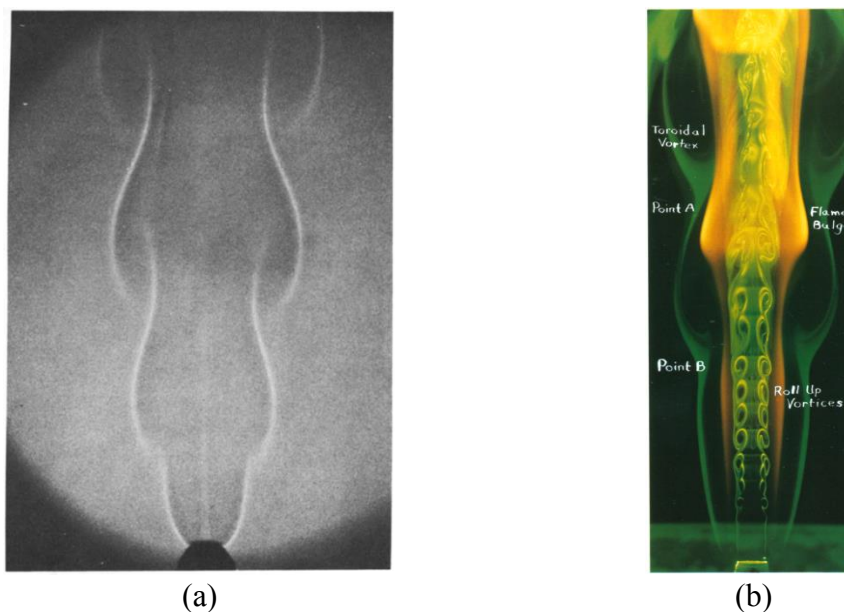


Figure 6.2 Experimental photographs of (a) wave structure of hydrogen jet diffusion flame [138] and (b) toroidal vortices of methane jet diffusion flame [139].

Many previous studies have focused on investigating and understanding the physics of the flickering diffusion flames [138-142], and these studies pointed to a striking feature of the flickering diffusion flames that the flicker is not caused by an externally

forced vibration or by the alternate flame extinction and re-ignition. Instead, the flicker of diffusion flames is a self-exciting flow oscillation. Grant and Jones [138] found that the frequency of oscillation of diffusion flame is always around of the order of 10 Hz, and it could not be affected greatly by the burner's size and type, and flow rate of the fuel, and meanwhile they observed the flow structure of hydrogen diffusion flame with low-frequency, as shown in Figure 6.2(a). A prominent substantiation of the feature was owing to Chen et al.'s [139] flow visualization of a methane jet diffusion flame, as shown in Figure 6.2(b), in which the small vortices inside of the luminous flame are due to the Kelvin-Helmholtz instability of the fuel jet, and the large toroidal vortices outside the luminous flame are due to the buoyance-induced Kelvin-Helmholtz instability. The frequency of the toroidal vortices was found to well correlate with the flicker frequency. Buckmaster and Peters [141] conducted a linear stability analysis to a self-similar solution of an annular burner diffusion flame and confirmed that the Kelvin-Helmholtz instability of the buoyancy-induced flow is responsible for the flicker. The quantitatively poor predictions of the stability analysis based on the quasi-parallel approximation were remedied by Moreno-Boza et al [142] using the global linear stability analysis. Previous experimental studies [143-147] identified a prominent empirical scaling law for the frequency of flame flickering as follows:

$$f \propto (g/D)^{1/2} \quad (6.1)$$

where g is the gravitational acceleration and D is fuel inlet diameter of burner and Figure 6.3 shows the summary of empirical flickering frequency as a function of burner

diameter. The correlation led to the dimensionless scaling law as follows:

$$St \sim Fr^{-1/2} \quad (6.2)$$

$$St = f \cdot D/V \quad (6.3)$$

$$Fr = V^2/gD \quad (6.4)$$

where St is the Strouhal number; Fr is the Froude number, and V is the fuel flow at the exit of the burner. Among the studies, Cetegen and Ahmed [147] extended the empirical scaling law to account for the buoyancy-induced flow velocity by introducing a Richardson number correction factor, so the expression for the frequency of flickering given by

$$f \propto (g/D)^{1/2} [(1 + Ri^{-1})^{1/2} + Ri^{-1/2}] \quad (6.5)$$

$$Ri = (\rho_{\infty}/\rho - 1)gD/V^2 \quad (6.6)$$

where Ri is Richardson number, and ρ and ρ_{∞} are the density of flame and ambient, respectively.

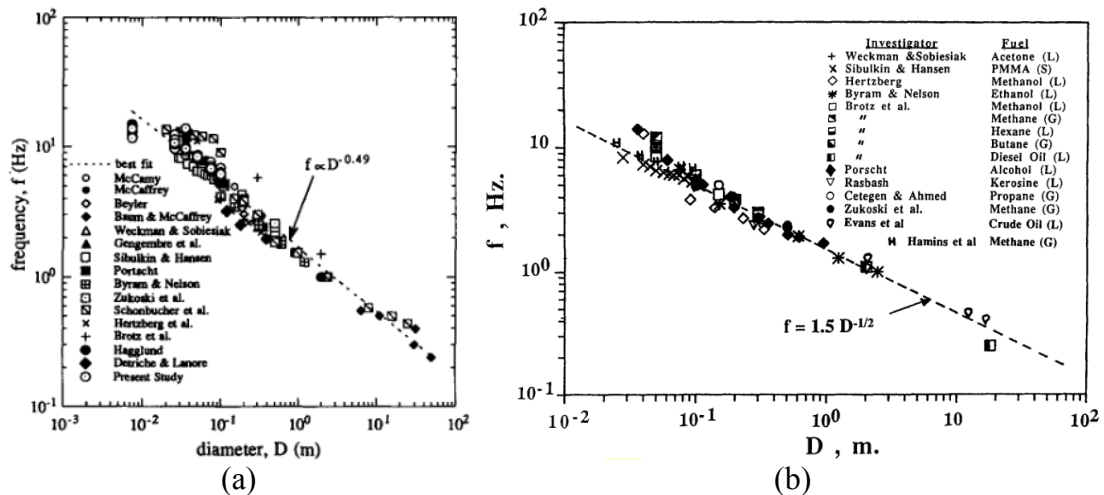


Figure 6.3 The summary of flickering frequencies of diffusion flame as a function of burner diameter: (a) Hamins et al. [146] and (b) Cetegen and Ahmed [147].

It is worth mentioning that Xia and Zhang [148] mathematically established the

connection between the periodicity of the toroidal vortices and the flickering of a buoyant diffusion flame with small Froude number ($Fr \ll 1$, for buoyancy-dominated flames). By applying a vortex shedding criterion, they obtained a scaling law that can well predicts the experimental results with $Fr \ll 1$ and $Ri \gg 1$.

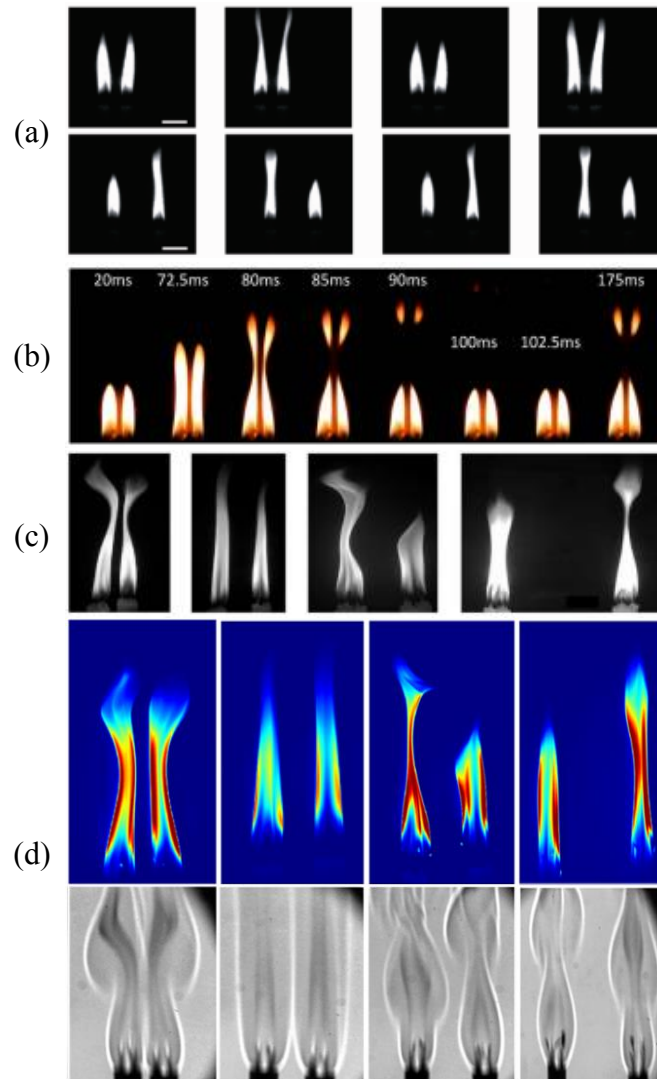


Figure 6.4 Experimental photographs of coupled dual candle flames: (a) in-phase (above) mode and anti-phase mode (below) by Kitahata et al. [149]; (b) in-phase mode by Forrester [150]; (c) from left to right are in-phase mode, death mode, anti-phase mode, and desynchronization mode by Manoj et al. [151]; and (d) from left to right are in-phase mode, death mode, anti-phase mode, and desynchronization mode by Dange et al. [152].

6.2 Coupled Dual Flickering Diffusion Flames

Compared with single flickering diffusion flame, more interesting dynamical behaviors were observed in coupled dual flickering diffusion flames. Kitahata et al. [149] made an oscillating flame by bundling three identical candles made of paraffin with a diameter of 6 mm while each candle burns steadily and observed that two such oscillating flames exhibit two distinct dynamical modes, in-phase mode and anti-phase mode, by increasing the distance between the two flames, as shown in Figure 6.4(a). Forrester [150] also found the similar phenomenon by two identical paraffin candles of 20 mm in diameter, as shown in Figure 6.4(b).

Besides the in-phase and anti-phase modes, with change of distance between the two flames, the amplitude death mode and desynchronization mode were reported by Manoj et al. [151] for each of the oscillating flame was made of bundling four identical candles of 8 mm in diameter, as shown in Figure 6.4(c). Subsequently, Dange et al. [152] also observed these four distinct dynamical modes, and it should be mentioned that they used high-speed shadowgraph and CH^* chemiluminescence which can show the interaction between buoyance-induced vortices plays a significant role in producing different dynamical modes, as shown in Figure 6.4(d).

The in-phase and anti-phase flicker of coupled dual buoyant diffusion flames was numerically reproduced by Yang et al. [153] for pool flames, and their results substantiated the vortex-dynamical conjecture that the interaction between toroidal vortices is responsible for the different flickering modes. Vortex-dynamical mechanism

of coupled dual flames were also substantiated by Fujisawa et al.'s [154] using PIV velocity field measurement of pipe-burner diffusion flames, by Bunkwang et al.'s [155, 156] experimental observations in methane/air jet diffusion flames, and by Tokami et al.'s [157] numerical simulation of buoyance-induced turbulent diffusion flames. Their results substantiate the vortex-dynamical conjecture that the interaction between two toroidal vortices is responsible for the different flickering modes.

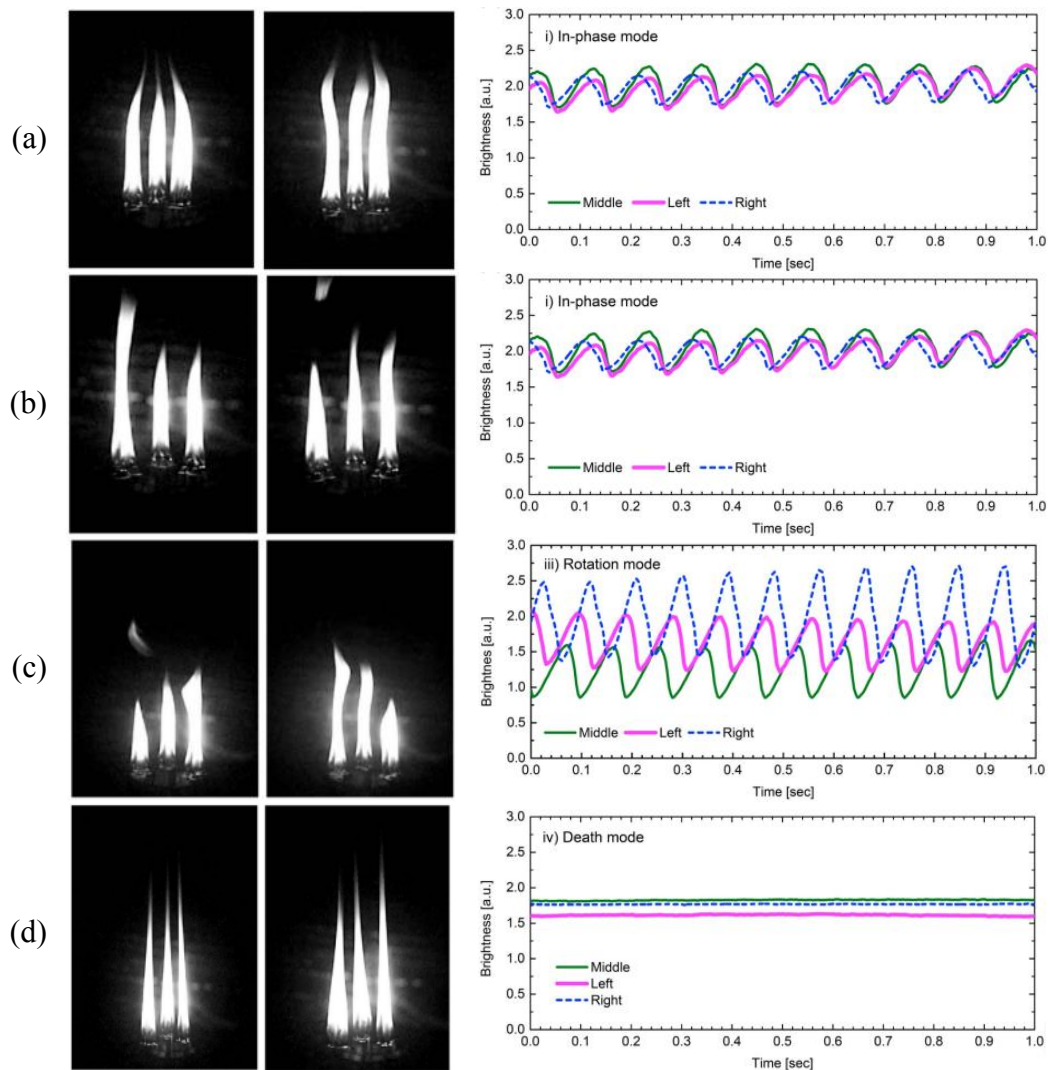


Figure 6.5 Experimental photographs and time series of each flame brightness [158] of four distinct dynamical modes: (a) the in-phase mode, (b) the partial in-phase mode, (c) the rotation mode, and (d) the death mode.

6.3 Coupled Multiple Flickering Diffusion Flames

For coupled multiple flickering diffusion flames, there will appear richer dynamical phenomena. Okamoto et al. [158] studied three coupled flickering flames by bundling three identical candles made of paraffin with a diameter of 9 mm in an equilateral triangle arrangement, and four distinct dynamical modes were observed: in-phase mode, the partial in-phase mode, the rotation mode, and the death mode, as shown in Figure 6.5.

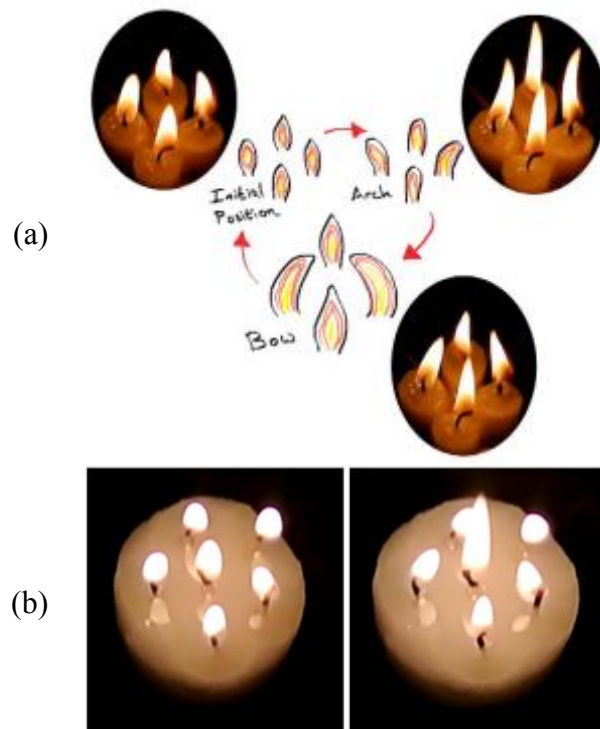


Figure 6.6 Experimental photographs [150] of (a) four coupled candle flames in an initial-arch-bow-initial “worship” oscillation mode and (b) five coupled candle flames in a ring-shape arrangement showing an outer ring of four candle flames enslaving a central flame, collectively enhancing (left) and suppressing (right) the height of the central flame.

Apart from two candle flames, Forrester [150] further investigated the system with more candle flames and observed an initial-arch-bow-initial “worship” oscillation

mode for four candles in a square arrangement, as shown in Figure 6.6(a), and conjectured the existence of a chimera state [159, 160], which is characterized by the hybrids of synchronized and desynchronized flames. Manoj et al. [161] also investigated the coupled four flickering candle flames in a rectangle arrangement, each of which was made of bundling four identical candles of 10 mm in diameter, and observed the clustering mode, in which the flames separate into two clusters of synchronized flames, the chimera mode, in which the flames separate into synchronized and desynchronized groups of flames, and the weak chimera mode, in which three frequency-synchronized flames coexist with one desynchronized flame.

Furthermore, the dynamical behaviours of coupled multiple flickering diffusion flames in various geometrical arrangements have been experimentally investigated by using candle flames. Forrester [150] studied candle flames in a ring arrangement and observed the ring flames collectively enhance and suppress the height of a central flame, as shown in Figure 6.6(b). Manoj et al. [162] experimentally observed very rich dynamical states in a network of flames with various arrangements such as straight line, triangle, square, star, and annular networks also by using candle flames. Chan et al. [163] also used candle flame to study the non-identical asymmetric flames and attributed the flame interaction to thermal radiation.

6.4 Research Objectives

Based on the above discussion, we can find that the study on a single flickering diffusion flame has achieved fairly fruitful results. Despite the noteworthy progress in

understanding dynamical behaviors of coupled (dual and multiple) flickering diffusion flames, there are many interesting problems to be solved and the relative studies are still in the preliminary stage, because the important difficulties are mainly focus on these three aspects: 1) lack of a well-controlled experiment platform with adjustable flame parameters; 2) the scarcity of reliable simulation results; 3) inadequately justified hypotheses of the existing models. Consequently, the present study was motivated by recognizing difficulty in experiment aspect, because reliable experimental results would play a significant role in the simulation and modelling studies.

Chapter 7 Dynamical Mode Recognition of Coupled Multiple Flickering Buoyant Diffusion Flames

7.1 Introduction

As discussed in Chapter 6, the objective of the study is two-fold: to establish a well-controlled gas-fuel diffusion flame experiment and to develop an objective methodology for dynamical mode recognition. The present study has solved the two major deficiencies in the existing experimental studies for hypothesis verification and phenomena discovery.

First, most previous experimental studies adopted candle flames [149-152, 158, 161-164], which are experimentally accessible but have a major drawback of the imprecise and inadequate controllability of flame parameters. In these experiments, an observed dynamical mode was often unstable and just sustained for a certain percentage of entire experimental duration. Although Gergely et al. [164] used a mixture of nitrogen, air and oxygen to study the effect of the oxygen concentration on candle flames. Such a “flame manipulation” can be easily realized by modifying the fuel supply for a diffusion flame burner. We hypothesized that the lack of adequate flame controllability is responsible for the unstable modes and that a well-controlled gas-fuel diffusion flame experiment could enhance their stability to external disturbances. Very recently, Aravind et al. [165] made an interesting attempt to use an ethanol lamp to enhance the tunability of their flame system.

Second, almost all previous experimental studies reported dynamical modes by

presenting their most distinct and representative cases. Based on our experimental results to be expatiated in the present study, many cases significantly deviate from the representative cases and appear as “transition modes” that are very difficult to recognize by observing the time-resolved images and analyzing their flicker frequencies [151, 165]. Dynamical mode recognition in physical space or frequency space becomes increasingly difficult for a system consisting of an increasing number of flames. Inspired by Bifurcation theory [166, 167], we hypothesized that the different modes are actually caused by the bifurcation of the flame dynamical system due to the change of its parameter values (the bifurcation parameters, e.g. the ratio of flame distance to flame diameter). Consequently, the conceptually correct method for mode recognition would focus on examining the topological structures of phase portraits in phase space.

The present study adopted Bunsen burners to produce flickering buoyant diffusion flames of methane. Owing to the precise controllability of flame parameters and the novel data analysis methodology based on Wasserstein Distance, a concept from optimal transport [168] and deep learning [169] theories, we could recognize more untypical dynamical modes in an objective way. It should be emphasized that, although the present study focused on triple flame systems, the proposed methodologies can be readily extended to larger flame systems.

7.2 Experimental Methodology

A schematic of the key experimental apparatus established for the present study is shown in Figure 7.1. Some of the apparatus have been used in our previous

experimental works [170-172]. Each Bunsen burner is 1 cm in diameter and 12 cm in height, and the nozzle outlet is pinched slightly to reduce the effect of tube thickness. The fuel flow rate Q of each individual burner is accurately regulated by a mass flow controller (Alicat Scientific, MC-Series:5SLPM-D/5M). In a trial, all burners are placed at same level and supplied at same Q to make flames identical. A high-speed camera (Chronos 2.1-HD) with a 105 mm UV lens was used to obtain time-resolved (500 fps) images of front views. As the camera was 2-meter away from the burners, which significantly larger than the flame characteristic scale (< 0.1 m), the influence of depth of field on the physical quantity of each flame is negligible in our image processing. To ensure the consistency in both phenomena observed and experimental data at the same testing conditions, not only a fire-proof curtain and mesh screen were used to minimize any external disturbance, but also the ambient environment was kept at a constant condition (25°C and 1 atm) prior to each trial. Furthermore, each case was carried out for multiple times, each trial was continuously recorded for 22 second after triple flames were fully developed.

To unify previous studies by Okamoto et al. [158] on equal-lateral triangle flame system and Manoj et al. [162] on straight-line and equal-lateral triangle flame systems, we arranged the triple flames in an isosceles triangle with variable leg (L) and base (B), also denoted the distance between the two flames in the study of dual flickering buoyant diffusion flames. As a limiting case of $B = 2L$, the isosceles triangle is degenerated to a straight line. The case of $B = L$ belongs to the equal-lateral triangle flame system. It

should be noted that the D_2 symmetry of the isosceles triangle arrangement imposes additional constraints to the flame dynamical system. The present symmetric triple flames retain the nature of the problem (interaction among flames) and avoid unnecessary complexity (multifarious arrangements). Therefore, we have a systematic and comprehensive study of the triple flickering diffusion flames in this arrangement and the merit will be seen in recognizing flame modes.

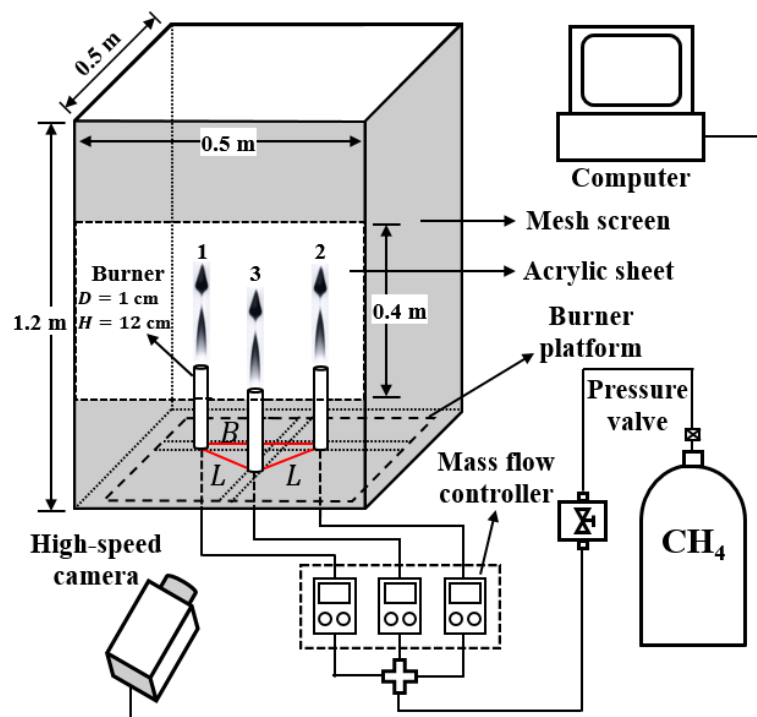


Figure 7.1 Schematic of the established experimental apparatus consisting of burners, fuel flow controls, and visualization systems.

7.3 Dynamical Mode Recognition for Stable Modes in Physical Space

7.3.1 Dynamical Modes of Dual Flickering Buoyant Diffusion Flames

To validate the present experimental setup, we reproduced the previous experimental observations [142, 147, 149-152, 154-156, 173-176] in single and dual flame systems.

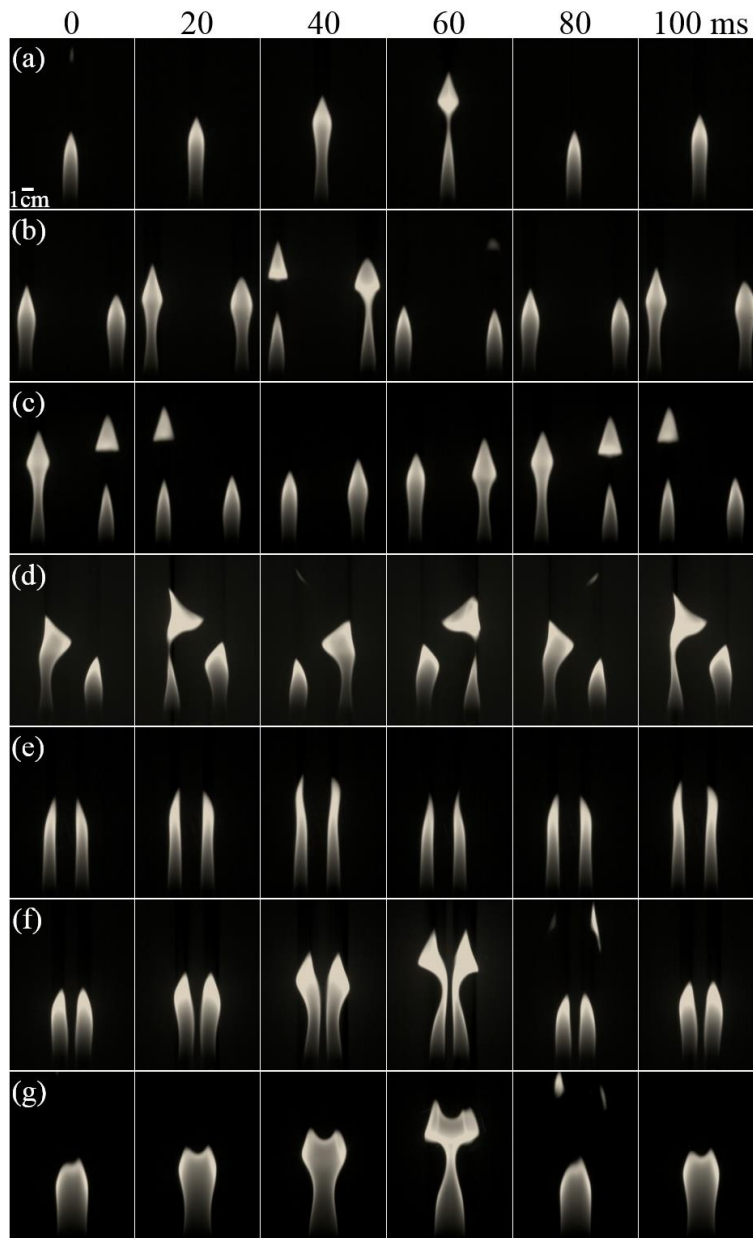


Figure 7.2 Experimental photographs of flickering buoyant diffusion flames for (a) single flame system and dual flame system in (b) the decoupled mode, (c) the weakly coupled mode, (d) the anti-phase mode, (e) the flickering death mode, (f) the in-phase mode, and (g) the merged case, at the distance of 8.0, 6.0, 4.0, 3.0, 2.0, and 1.5 cm, respectively. All the flames have the fuel flow rate $Q = 0.55$ slpm.

As shown in Figure 7.2(a), a diffusion flame significantly oscillates up and down in accompany with the flame pinch-off (an upper part of flame gets separated from the main flame). The periodic motion, named as the flame flicker here, is clearly observed in the flow rate range of $Q = 0.45 \sim 0.65$ slpm, as shown in Figure 7.3. Such

flickering flames were used to constitute multiple flame systems in the present study. In Figure 7.2(b)-(f), by changing the distance between two identical flickering flames, there are five distinct modes such as the decoupled mode (at sufficiently large distance, e.g., $B = 8$ cm), the weakly coupled mode (at relatively large distance, e.g., $B = 6$ cm), the anti-phase (at intermediate distances, e.g., $B = 4$ cm), the flickering death (at intermediate distances of a narrow range, e.g., $B = 3$ cm), and the in-phase modes (at relatively small distances, e.g., $B = 2$ cm). Further reducing the distance (e.g., $B = 1.5$ cm) between the two flames will cause them to merge as shown in Figure 7.2(g), which is often not considered as a dynamic mode. It is interesting to note that the flickering death mode is characterized by that the flame pinch-off vanishes and the flame tip oscillates with a slight amplitude. The similar amplitude death phenomenon was observed in the candle-flame experiment of Manoj et al. [151] as those flames ceases to oscillate.

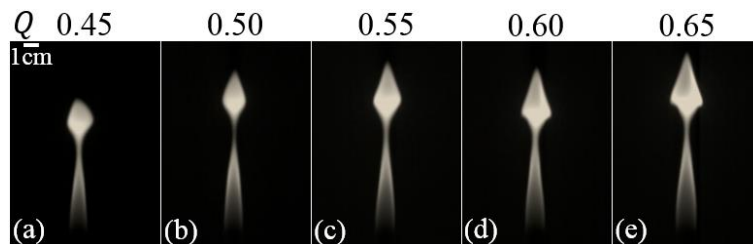


Figure 7.3 Single flickering buoyant diffusion flames. The flow rates (a-e) are fixed at $Q = 0.45, 0.50, 0.55, 0.60$ and 0.65 slpm, respectively.

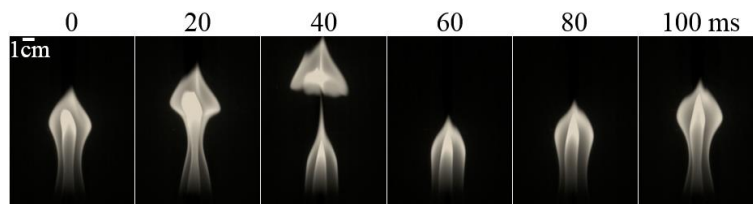


Figure 7.4 Merged triple flickering buoyant diffusion flames at $Q = 0.45$ slpm.

7.3.2 Dynamical Modes of Triple Flickering Buoyant Diffusion Flames

By using the present flame system, we investigated 125 cases of triple flames in an isosceles triangle by varying the base ($B/D = 4\sim 8$), the leg ($L/D = 2\sim 10.8$) and the flow rate ($Q = 0.45\sim 0.65$ slpm). As three flames are too close to each other, they can merge into a bigger one with a smaller flickering frequency, as shown in Figure 7.4, which renders a case of no interest to the present study. After examining all experimental cases, seven representative dynamical modes, as shown in Figure 7.5, were readily identified by observing the different phase and amplitude of the flames and described in detail below. Their flame setups are given in Table 7.1.

Mode I: the in-phase mode appears as the three flames flicker synchronously with negligible phase difference, when the flame burners are sufficiently separated (e.g., $B = 4.0$ cm, $L = 2.8$ cm, $Q = 0.55$ slpm). It is noted that Manoj et al. [162] named the mode as “clustering”, where three flames exhibit the same frequency and maintain a constant phase difference. However, they found the case of vanishing phase difference (i.e., the in-phase mode) was unstable in their candle experiments. In the recent computational work of Yang et al. [177], a “trefoil” vortex is formed around the flames due to the vortex reconnection. The periodic shed-off of the “trefoil” vortex results in the necking and pinch-off of the three flames in a synchronous manner.

Mode II: the flickering death mode appears as the three flames oscillate with a small amplitude without the flame flicker, if flow rate is slightly smaller (e.g., $B = 4.0$ cm, $L = 2.8$ cm, $Q = 0.45$ slpm) than that in Mode I. The death mode reported by

Okamoto et al. [158] is a special case of Model II when the oscillation amplitude is sufficiently suppressed. According to Yang et al. [177], this mode occurs when the formed “trefoil” vortex sheds off in the downstream of the flames, resulting in no necking and pinch-off of the flames.

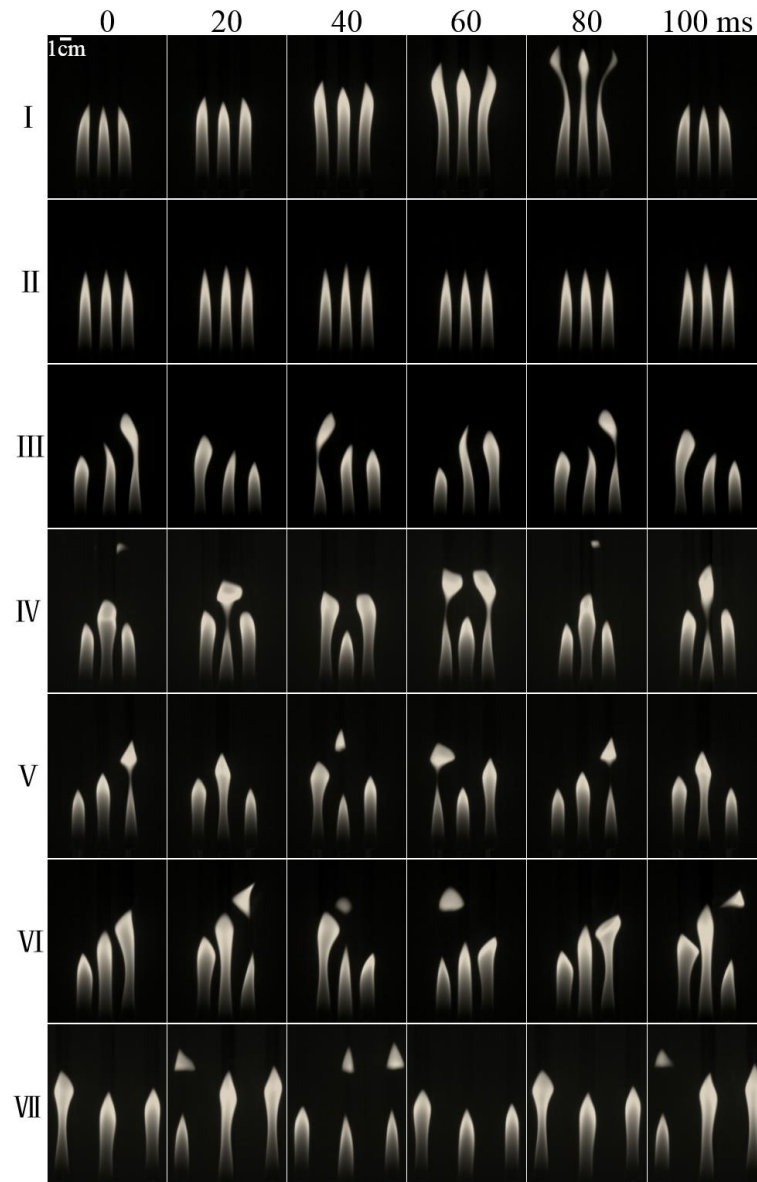


Figure 7.5 Experimental photographs of seven distinct stable dynamical modes of triple flickering buoyant diffusion flames. I-VII are in-phase, flickering death, partial flickering death, partial in-phase, rotation, partial decoupled, decoupled respectively. See details of flame setup in Table 7.1.

Mode III: partial flickering death mode occurs when the distances of three flame

burners are further increased (e.g., $B = 5.0$ cm, $L = 3.2$ cm, $Q = 0.45$ slpm). The two base flames flicker in an anti-phase way while the vertex flame oscillates without the flame flicker.

Mode IV: the partial in-phase mode appears as the two base flames are in-phase to each other but anti-phase to the vertex flame, if the vertex flame is farther compared with that in Mode I (e.g., $B = 4.0$ cm, $L = 4.5$ cm, $Q = 0.50$ slpm). This mode was interpreted by Yang et al. [177] as that the vorticity reconnection occurs between the toroidal vortices around two flames. This mode was reported by Okamoto et al. [158] as an unstable one. Manoj et al. [162] categorized it into a “rotating cluster” mode predominantly observed for the straight-line flame configuration, in which the in-phase flame pairs transition in time.

Mode V: the rotation mode appears as the flames alternatively flicker with a fixed phase difference, if the three flames are arranged to an equal-lateral triangle (e.g., $B = 5.0$ cm, $L = 5.0$ cm, $Q = 0.45$ slpm). Computational results of Yang et al. [177] showed that each toroidal vortex alternatively sheds off but without apparent vorticity reconnection and that the vortex-induced flows are responsible for the vortex interaction. The phase difference is $2\pi/3$ for an equal-lateral triangle due to its D_3 symmetry, but it can slightly deviate from $2\pi/3$ for the isosceles triangle with D_2 symmetry (for example, the case of $B = 5.0$ cm, $L = 4.7$ cm, $Q = 0.50$ slpm).

Mode VI: the partial decoupled mode appears as the two base flames are anti-phase while the vertex flame flickers independently, if the vertex flame is sufficiently away

from the two base flames (e.g., $B = 4.0$ cm, $L = 10.2$ cm, $Q = 0.50$ slpm).

Mode VII: the decoupled mode occurs if the two base flames are also sufficiently away from each other (e.g., $B = 8.0$ cm, $L = 10.8$ cm, $Q = 0.50$ slpm), so that the three flames flicker independently. It is noted that Manoj et al. [162] named Mode VI as “weak chimera” and Mode VII as “complete desynchrony”.

Table 7.1. The flames setup parameters in an isosceles triangle for Mode I – Mode VII and stable cases C1 – C7 (unit of B and L : cm; unit of Q : slpm).

Mode	B	L	Q	Case	B	L	Q
I	4.0	2.8	0.55	C1	4.0	2.8	0.65
II	4.0	2.8	0.45	C2	4.0	2.8	0.50
III	5.0	3.2	0.45	C3	6.0	3.6	0.45
IV	4.0	4.5	0.50	C4	7.0	4.0	0.50
V	5.0	5.0	0.45	C5	5.0	5.0	0.50
VI	4.0	10.2	0.50	C6	4.0	8.2	0.50
VII	8.0	10.8	0.50	C7	8.0	8.9	0.50

It should be emphasized that the above seven representative modes can exist within almost the entire time duration of recorded flame videos and were highly repeatable for any longer duration. However, in the previous candle flame experiment [158, 162], dynamical modes were often unstable as different modes were found during different time durations in the same test run. We hypothesized that the unstable behavior was due to the use of undisciplinable candle flames and can be completely eliminated by using independent fuel control system for each flame in the present experiment. In fact, our experimental results verify that dynamical modes of coupled flickering flame system should be stable in a well-controlled gas-fuel diffusion flame experiment.

7.4 Dynamical Mode Recognition for Stable Modes in Phase Space

To verify our second hypothesis that different modes of the flame system correspond to the different topological structures of the phase portrait in phase space,

we proposed to reduce the present infinite-dimensional dynamical system, which is governed by the partial differential equations describing the time-space evolution of the chemically reacting flow, to a finite-dimensional dynamical system, whose temporal evolution can be described by ordinary differential equations. The crucial procedure of the dimension reduction is to choose a certain number of time-dependent variables that can characterize each flickering flames and their interaction.

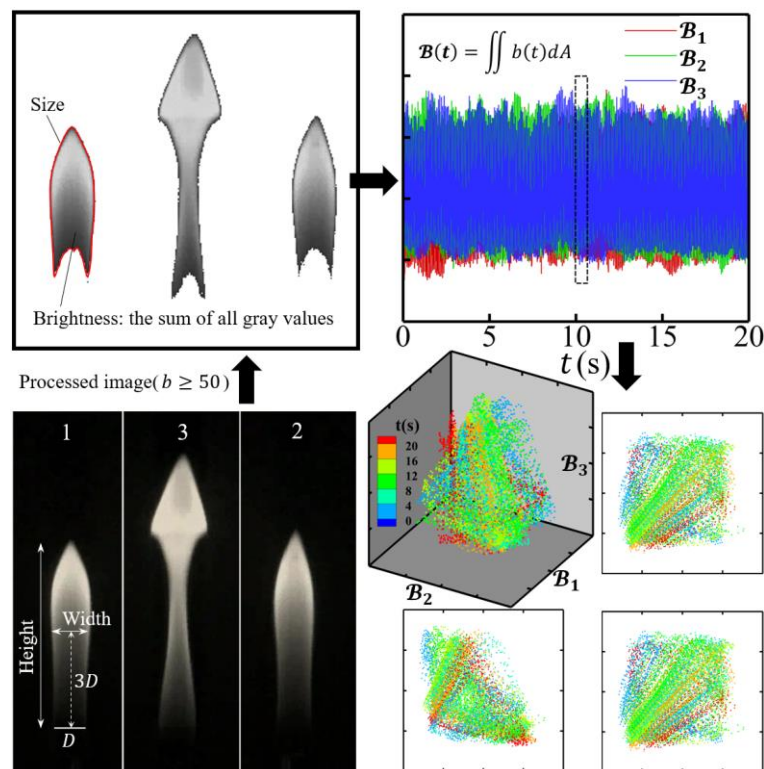


Figure 7.6 The schematic of establishing phase portraits in a three-dimensional phase space. Each grayscale image is processed and extracted for four time-varying quantities (height, width, size, and brightness) of each flickering flame. The flame brightness is taken an example here. The 22s duration of triple flickering flames yields 11000 phase points in phase space.

7.4.1 Characteristic Quantities of Flickering Flames

As we have discussed in the Introduction, the flickering of a buoyant diffusion flame results from the formation, growth and shed-off of toroidal vortex around the flame.

Apparently, there is quite freedom in selecting and acquiring characteristic quantities from the flames, for example, the pressure or temperature of flickering flame at a certain position [147]; the flame luminosity at a certain height [178]; the flame morphology information obtained from high-speed images. The first two contain local flame information of the flickering flames, while the last one contains both local (e.g., flame height and amplitude [150, 154]) and global (e.g., flame size and brightness [149, 164, 165]) information of the flickering flames. In the present study, we adopted the simplest approach by acquiring one time-dependent variable for each flame directly from the experimental high-speed images. Similar approaches have been widely used in previous studies [149-152, 154, 158, 161-165].

On each grayscale high-speed image at a certain time instant, the brightness of each pixel can be represented by an integer $b(t)$ from 0 (pure black) to 255 (pure white). A truncation value of $b = 50$ was used to obtain the bright contour for each flame in current experiments, which is equivalently the Otsu method for binarizing grayscale image [164, 179]. As shown in Figure 7.6, four time-varying quantities (height, width, size, and brightness) of each flickering flame can be defined: the flame height is the vertical distance between the flame tip and the nozzle; the flame width is the horizontal distance of flame contour at the height of three nozzle diameters; the flame size is the contour area of each flame; the flame brightness is the integration of all brightness values within a flame contour. Our results show that all of the quantities exhibit the same frequency with the flickering flame, while there are phase differences among them,

as shown in Figure 7.7.

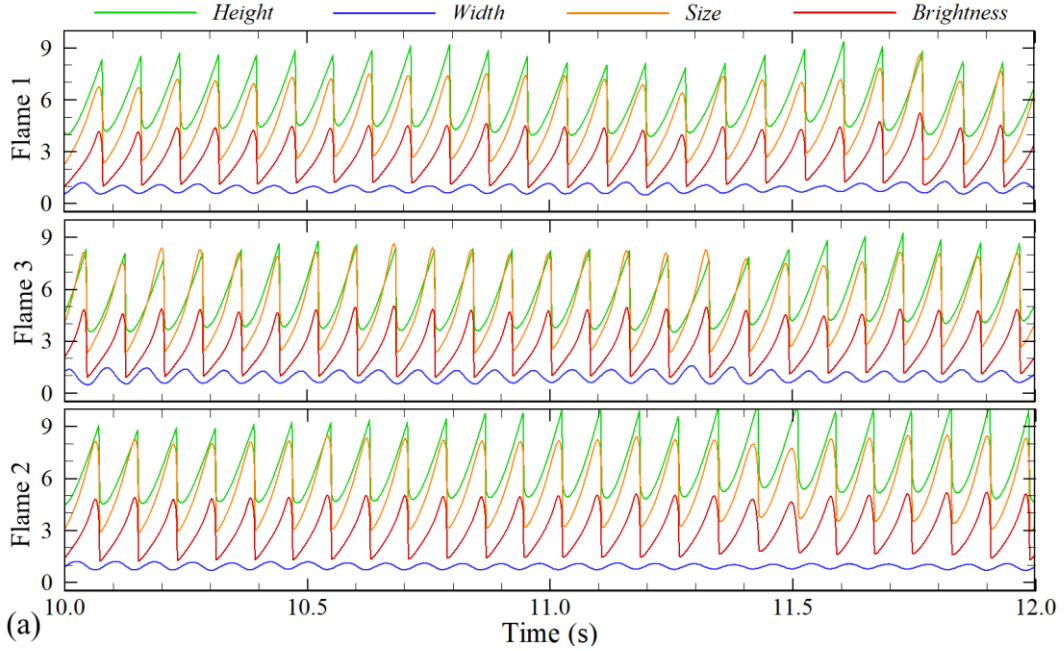


Figure 7.7 Time-varying graphs of scalar quantities (height, width, size, and brightness) for each flickering flame. The time corresponds to 10-12s in Figure 7.6 The height and width are normalized by the nozzle diameter, the size by the nozzle area, and the brightness by the product of 255 and the nozzle area.

By use of the time-varying characteristic quantities for each flame, we can obtain a representation of the dynamical behavior of the flame system in phase space. For instance, the flame brightness is expressed as $\mathcal{B}_i(t) = \iint b(t) dA$, where i indicates the flame 1-3 and A is the contour area of each flame. Consequently, the dynamical state of the triple flame system at time t is represented by a phase point in a three-dimensional phase space with coordinates $(\mathcal{B}_1(t), \mathcal{B}_2(t), \mathcal{B}_3(t))$. The time-evolution of the triple flame system generates a continuous phase trajectory, and the phase trajectory within a sufficiently long-time duration generates an approximately continuous phase portrait. In addition, to facilitate the recognition of topological structure of phase portraits, the two-dimensional phase portraits are generated by

projecting the three-dimensional phase portraits to each coordinate planes, as shown in Figure 7.6.

By comparing the phase portraits based on the flame height, width, size, and brightness respectively, we found that they have similar topological structures except that based on the flame width. The reason can be explained from the perspective of vortex dynamics. The flickering flame is a periodic phenomenon due to the streamwise evolution of toroidal vortices, while the flame width just manifests the local transverse information. Consequently, the global quantity of flame brightness may be better to characterize the flames than the other local flame quantities, particularly under the presence of flame interaction. It is noted that the flame brightness is calculated from the front-view snapshot and neglects the three-dimensional effect of flame collective behavior [150], because we found that the flame brightness of each one in triple flickering flames compared with that in single flickering flame has no significant difference in magnitude. Based on the above considerations, the flame brightness was adopted in the following data analysis, and this choice is consistent with previous studies [158, 161-163].

7.4.2 Phase Portraits for Dynamical Modes of Dual Flickering Flames

To facilitate the dynamical mode recognition of triple flickering flames and to validate the phase-space-based mode recognition, we analyzed the experimental results for dual flicking flames, as shown in Figure 7.8, which correspond to the cases in Figure 7.2(b)-(f), namely the decoupled, weakly decoupled, anti-phase, flickering death, and

in-phase modes, respectively, with decreasing the distance between two flames.

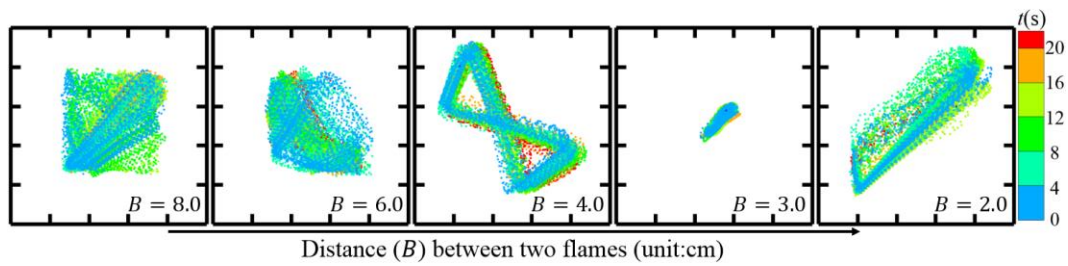


Figure 7.8 Two-dimensional phase portraits for dual flickering buoyant diffusion flames, corresponding to the cases in Figure 7.2(b)-(f). There are five synchronized flickering modes with the distance decreasing. All phase spaces, plotted by the flame brightness, have the same ranges of values in all dimensions.

The phase portrait for dual decoupled flames, i.e., the case in Figure 7.2(b), shows a square-shape, probably due to the “ergodic” nature of the decoupled dynamical system where the two flames have no interaction. As a result, the flames can exhibit almost all dynamical states, and the phase points can fill up almost the entire accessible phase space. The phase portrait for dual anti-phase flames, i.e., the case in Figure 7.2(d), has a butterfly-like shape along the (1, -1) direction. The anti-phase synchronization can be seen as the coordinates of phase points vary temporarily in an opposite way. The phase portrait for dual weakly decoupled flames, i.e., the case in Figure 7.2(c), has a mixed shape of a butterfly and a square, implying an intermediate mode between the decoupled and anti-phase modes. The phase portrait for dual flickering-death flames, i.e., the case in Figure 7.2(e), occupies a significantly smaller phase volume in the phase space than other modes. If the small-amplitude oscillation of the flames’ ceases, this phase volume may be vanishingly small. The phase portrait for dual in-phase flames, i.e., the case in Figure 7.2(f), is a slender ellipse along the (1, 1) direction, indicating

that the coordinates of the phase points vary temporarily in the same way.

It is noted that previous studies [151, 165] adopted the correlation coefficient to distinguish the dynamical modes because of the directional features of phase-point distribution. But the approach cannot be suitable for complex synchronized modes in more than two coupled flickering flames. The significance of the present approach of identifying distinct shapes (topological structures) for the five typical flickering modes of dual flames is based on the following hypotheses to be verified in the following section. The phase portraits of larger dynamical systems are substantially more complex, but their two-dimensional projections can be readily analyzed by comparing them with the five typical phase portraits of the dual flame systems.

7.4.3 Phase Portraits for Dynamical Modes of Triple Flickering Flames

The three-dimensional phase portraits and their two-dimensional projections for seven representative dynamical modes, corresponding to the cases of Mode I-Mode VII in Figure 7.5 respectively, are shown in Figure 7.9. The 2D projections (i.e., $\mathcal{B}_1 - \mathcal{B}_2$, $\mathcal{B}_1 - \mathcal{B}_3$ and $\mathcal{B}_2 - \mathcal{B}_3$ phase portraits) are convenient to recognize the topological structures of 3D phase portraits, which imply the interaction between each pair of flames. It should be noted that all phase portraits have the same time duration (i.e., 22s physical time and about 250 periods) and that all phase spaces have the same ranges of coordinates in all dimensions. Subsequently, several important observations for the triple flame system can be made as follows:

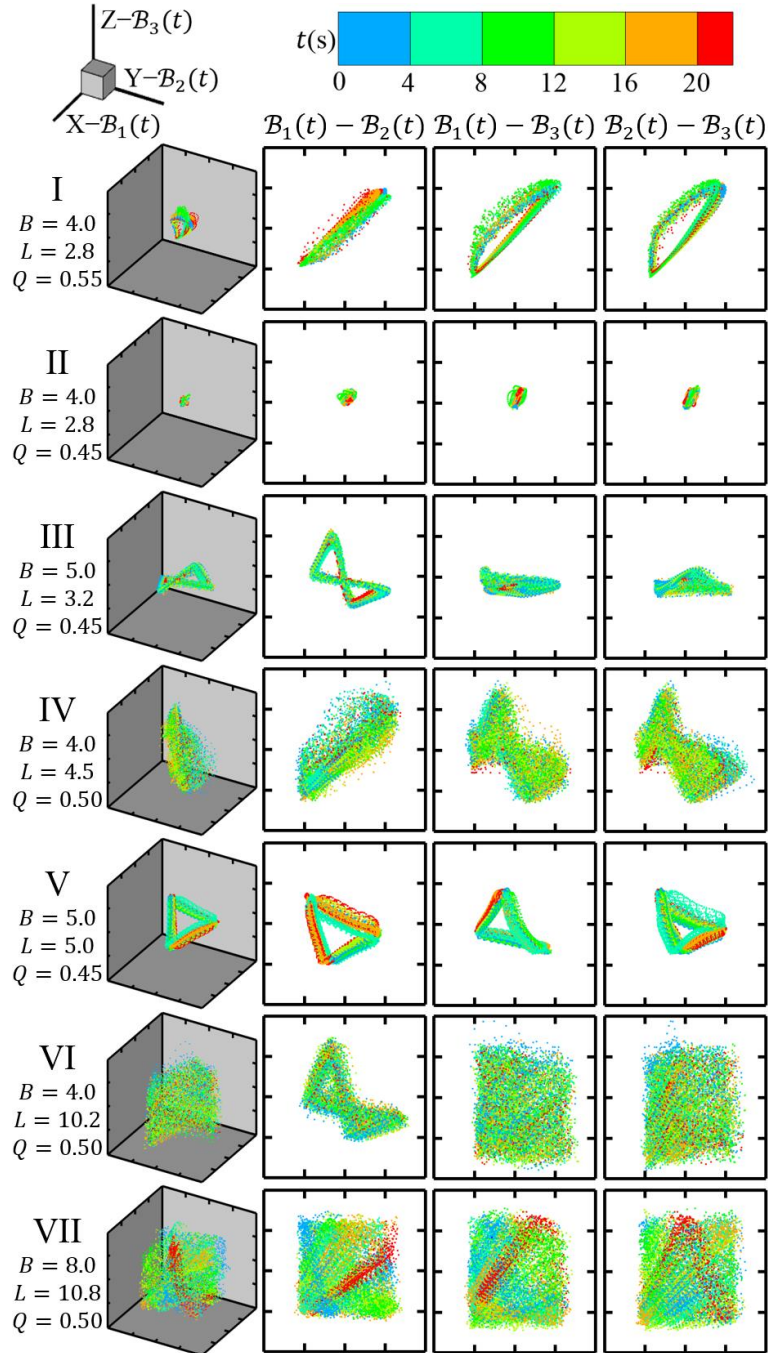


Figure 7.9 Three-dimensional phase portraits, their two-dimensional projections, and flame setup parameters (unit of B and L : cm; unit of Q : slpm) for seven stable dynamical modes, corresponding to the cases of Mode I-Mode VII in Figure 7.5 respectively. All phase spaces, plotted by the flame brightness, have the same ranges of coordinates in all dimensions.

First, the phase volume occupied by a phase portrait can be used as a measure of the dynamic amplitude of triple flickering flames. After unifying same ranges of

coordinates in all dimensions, we obtain that the flickering death mode (Mode II) has the smallest phase volume while the decoupled mode (Mode VII) has the largest phase volume.

Second, the in-phase mode (Mode I) has a 3D phase portrait in the shape of slender ellipsoid, whose major principal axis is along the direction $(1,1,1)$ in the phase space. Their three 2D projections are all in the shape of slender ellipse, whose major axis is along the direction of $(1,1)$. There is a consistency for the phase spaces in dual and triple flickering flame systems.

Third, the flickering death mode (Mode II) has a 3D phase portrait in the nearly spherical shape and all its three 2D projections in the nearly round disk shape. It means that the triple flickering flames cease flicker. The partial flickering death mode (Mode III) has two horizontal 2D projections and a butterfly-shaped 2D projection. The horizontal phase portrait for $\mathcal{B}_1 - \mathcal{B}_3$ or $\mathcal{B}_2 - \mathcal{B}_3$ suggests that one of flames stops flickering. The butterfly phase portrait for $\mathcal{B}_1 - \mathcal{B}_2$ is a closed loop spreading out along the direction $(1, -1)$ and reflectionally symmetric with respect to the axis $(1,1)$, which is a typical phase portrait for two anti-phase flames.

Fourth, the partial in-phase mode (Mode IV) has an ellipse-shaped 2D projection and two butterfly-shaped 2D projections. It is easy to understand that the two vertex-base flame pairs must have the same dynamical behaviors due to the D_2 symmetry of isosceles triangle. As shown in the two rightmost columns of Figure 7.9, the symmetry constraint results in the same topological structure of 2D phase portraits for $\mathcal{B}_1 - \mathcal{B}_3$

and $\mathcal{B}_2 - \mathcal{B}_3$ in all cases.

Fifth, the rotation mode (Mode V) has three 2D projections in the shape of triangle. It is seen that some phase points deviate from the triangular closed loop due to external disturbance but will be attracted back to the closed loop. In fact, the nearly same interactions between toroidal vortices around each two flames are through the vortex-induced flow, instead of the vortex reconnection [177].

Finally, the decoupled mode (Mode VII) has three square-shaped 2D projections. All the phase points tend to homogenously spread out in the square probably due to the ergodicity of the decoupled system. The triangular patterns can be barely recognized in the phase portraits as the result of the very weakly flame interaction at large flame separation distance. The partial decoupled mode (Mode VI) has a butterfly phase portrait for $\mathcal{B}_1 - \mathcal{B}_2$ and two square phase portraits for $\mathcal{B}_1 - \mathcal{B}_3$ and $\mathcal{B}_2 - \mathcal{B}_3$ because the two base flames are in anti-phase but without dependence with the vertex flame.

7.5 Dynamical Mode Recognition based on Wasserstein Distance

7.5.1 Motivations for Wasserstein-distance-based Mode Recognition

Hereto, seven representative dynamical modes have been recognized in the present experiment of triple flickering flames, but the above proposed methodology for dynamical mode recognition in phase space lacks sufficient generality and precision if the phase portraits are different from those of the representative cases, as shown in Figure 7.10.

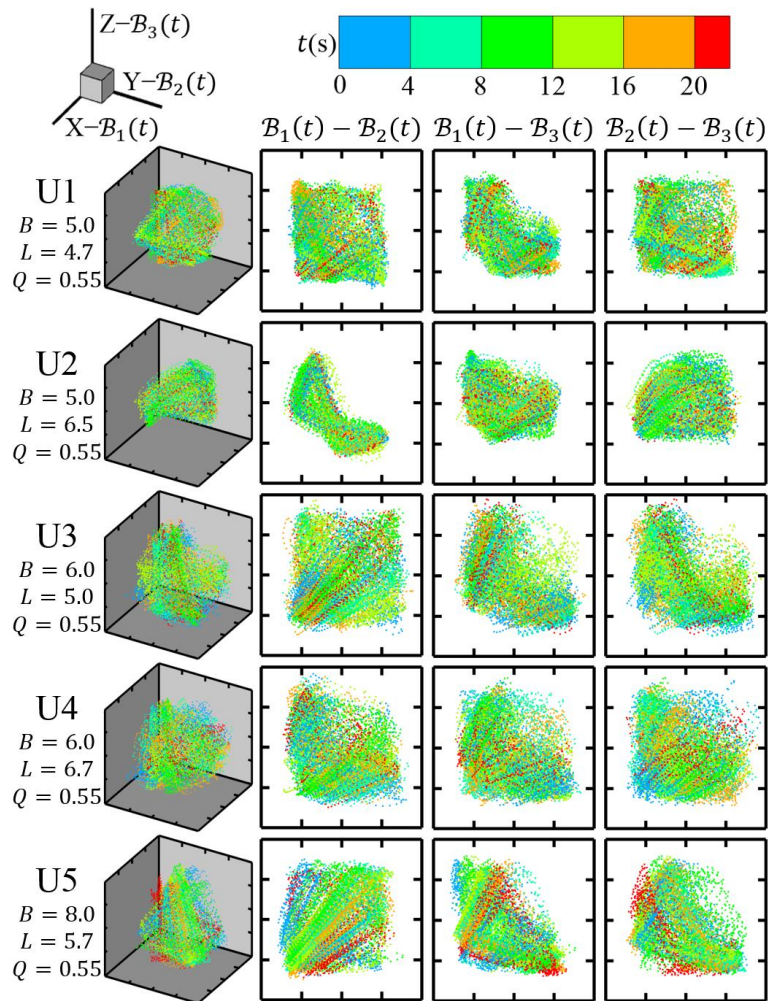


Figure 7.10 Three-dimensional phase portraits, their two-dimensional projections, and the flame setup parameters (unit of B and L : cm; unit of Q : slpm) for untypical dynamical modes. All phase spaces, plotted by the flame brightness, have the same ranges of coordinates in all dimensions.

There are a few considerations about the model recognition in general situation. First, many experimental cases do not generate the typical phase portraits due to the occurrence of “intermittent” behaviors. Namely, two or more typical modes transition in time within a certain time duration, for example the case shown in Figure 7.11. Second, the mode recognition based on the human visual perception of shapes in phase space, is unavoidably subjective and imprecise. In addition, different understanding and cognition usually cause different choices of terminology, such as the shapes of phase

portraits for $\mathcal{B}_2 - \mathcal{B}_3$ during 4.0-4.2s, $\mathcal{B}_1 - \mathcal{B}_2$ and $\mathcal{B}_1 - \mathcal{B}_3$ during 12.0-12.2s, and $\mathcal{B}_1 - \mathcal{B}_3$ during 20.0-20.2s in Figure 7.11. Third, the shape of a phase portrait may not be a useful concept in a higher-dimensional phase space, which certainly emerges in a system with more than three flames. Therefore, the above insights on the phase-space recognition naturally motivate us to seek a more objective methodology for model recognition.

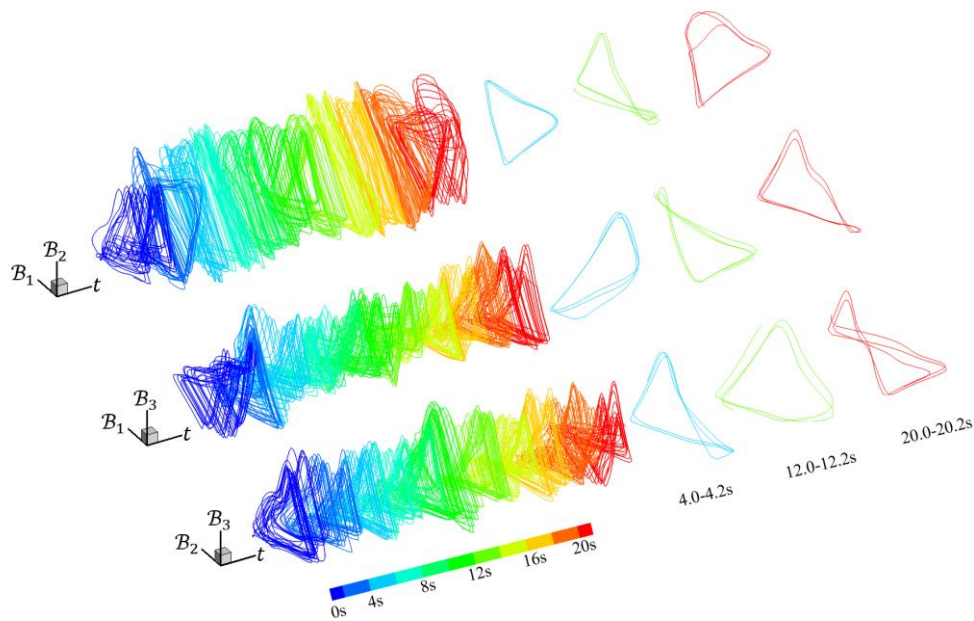


Figure 7.11 The time-varying topological structures of phase portraits. The 2D phase portraits for $\mathcal{B}_1 - \mathcal{B}_2$, $\mathcal{B}_1 - \mathcal{B}_3$ and $\mathcal{B}_2 - \mathcal{B}_3$ are unstable during the 22s and not recognized readily. All phase spaces, plotted by the flame brightness, have the same ranges of coordinates in all dimensions.

Inspired by the Manifold Distribution Hypothesis from Generative Adversarial Networks [169], we proposed to identify different dynamical modes according to the probability distributions of phase points instead of the shapes of phase portraits. Specifically, any two dynamical modes of the multiple flame system are the same if the probability distributions of their phase points are close to each other. In mathematics,

the Wasserstein distance (or Kantorovich-Rubinstein metric) is a natural way to quantify the closeness of two probability distributions [180, 181]. Therefore, if any dynamical mode of the flame system is chosen as the reference, the closeness of other modes to it can be quantified by the Wasserstein distance between their probability distributions of phase points. As the result, we obtain a metric space with probability distributions as points and Wasserstein distance as the metric; this metric space is called Wasserstein space.

7.5.2 Calculation of Wasserstein Distance

In the present work, we adopted the simplest 1-Wasserstein distance (also known as the earth mover's distance [182] defined by

$$W_1(\mu, \nu) = \inf_{\gamma \in \Gamma(\mu, \nu)} \int d(x, y) d\gamma(x, y) \quad (7.1)$$

where μ and ν are two distribution functions on a metric space (M, d) , $\Gamma(\mu, \nu)$ is the set of all joint distributions whose marginals are μ and ν . In the present problem, M is the set of indexed phase points, and $d(x, y)$ is the natural distance between two phase points x and y by counting the difference of their indices. In addition, the 1-Wasserstein distance satisfies the three basic axioms for a metric [168]:

- (1) $W_1(\mu, \nu) \geq 0$ and the equality holds only for $\mu = \nu$
- (2) $W_1(\mu, \nu) = W_1(\nu, \mu)$ (7.2)
- (3) $W_1(\mu, \nu) < W_1(\mu, \gamma) + W_1(\gamma, \nu)$

The details about the theory of Wasserstein distance can be found in [168] and the detailed descriptions about the Matlab code used in the present work for calculating the

1-Wasserstein distance (W_1) can be found in [183].

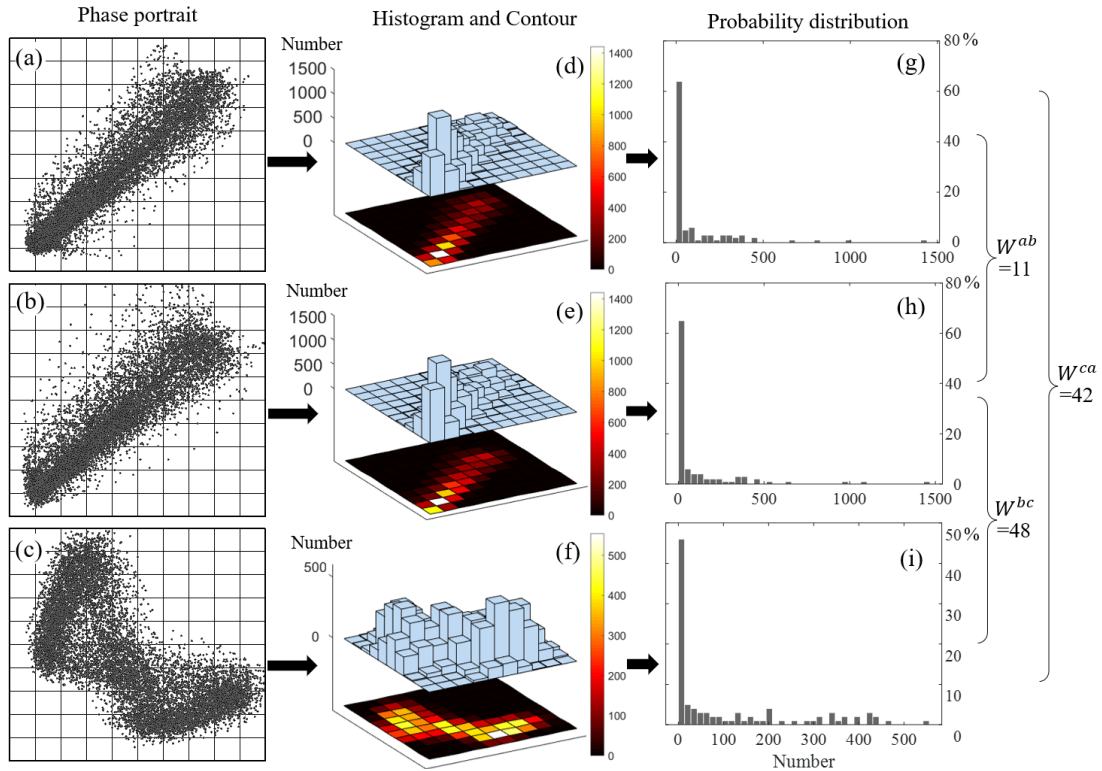


Figure 7.12 Phase portraits of in-phase, in-phase and anti-phase modes of two adjacent flames (a)-(c), the corresponding phase point distributions in 10×10 cells (d)-(f) and the corresponding discrete probability distributions of the number of phase points in each cell (g)-(i). The Wasserstein distance between the two probability distributions of (a) and (b), denoted by W^{ab} , is 11. W^{bc} of (b) and (c) is 48, and W^{ca} of (c) and (a) is 42.

The key procedures for calculating the Wasserstein distance between two probability distributions of phase points are as follows,

1) to obtain the histogram of phase portraits. For example, two different cases are in the in-phase mode and one case is in the anti-phase mode, of which the three different 2D phase portraits are shown in Figure 7.12(a)-(c), respectively. Each phase portrait is embedded into a 10×10 mesh, as shown in Figure 7.12(d)-(f).

2) to count and sort the number of phase points in each mesh cell for the discrete

probability distributions, as shown in Figure 7.12(g)-(i).

3) to calculate the earth mover's distance between the two discrete probability distributions. For example, the Wasserstein distance for the phase portraits in Figure 7.12(a) and Figure 7.12(b), denoted by W^{ab} , is 11; W^{bc} is 48; W^{ca} is 42.

Prior to the Wasserstein calculation, all cases are unified, namely phase points have same number and their physical variable is normalized. As a result, all calculated values are nonnegative, and the Wasserstein distance between similar phase portraits is much smaller than that between unlike phase portraits. For example, $W^{ab} < W^{ac}$, namely the phase portraits in Figure 7.12(a) and Figure 7.12(b) are closer than those in Figure 7.12(a) and Figure 7.12(c). Apparently, the distance between the same phase portraits is zero, such as $W^{aa} = 0$, $W^{bb} = 0$, and $W^{cc} = 0$. The other two axioms of metric are also satisfied, for example the symmetry law $W^{ab} = W^{ba} = 11$ and the triangle inequality $W^{bc} < W^{ab} + W^{ac}$.

Table 7.2 The calculated triplets (W^{12}, W^{13}, W^{23}) and their root mean square (shown in parentheses) of 1-Wasserstein distance between Mode I – Mode VII and the stable cases C1-C7.

Mode	C1	C2	C3	C4	C5	C6	C7
I	17 8 18 (15)	31 15 19 (23)	41 47 60 (50)	44 25 37 (36)	63 43 65 (58)	43 89 76 (72)	108 95 92 (99)
II	15 19 29 (22)	19 13 15 (16)	28 54 45 (44)	28 37 22 (30)	48 53 51 (51)	31 95 63 (68)	92 101 84 (93)
III	27 50 36 (39)	18 56 35 (40)	13 21 22 (19)	24 32 23 (27)	34 14 25 (26)	19 36 37 (32)	78 44 56 (61)
IV	30 46 40 (39)	22 52 31 (37)	28 27 20 (25)	15 27 12 (19)	34 13 28 (27)	29 45 42 (39)	77 53 67 (66)
V	62 41 53 (53)	44 44 51 (46)	36 24 17 (27)	26 23 36 (29)	12 10 9 (10)	38 48 18 (37)	42 55 41 (46)
VI	43 80 70 (66)	24 82 71 (64)	14 39 29 (29)	31 62 56 (51)	22 42 18 (29)	11 7 8 (9)	68 16 22 (42)
VII	105 92 82 (93)	88 93 90 (90)	79 50 52 (62)	67 78 78 (75)	50 58 42 (50)	78 16 31 (49)	6 7 8 (7)

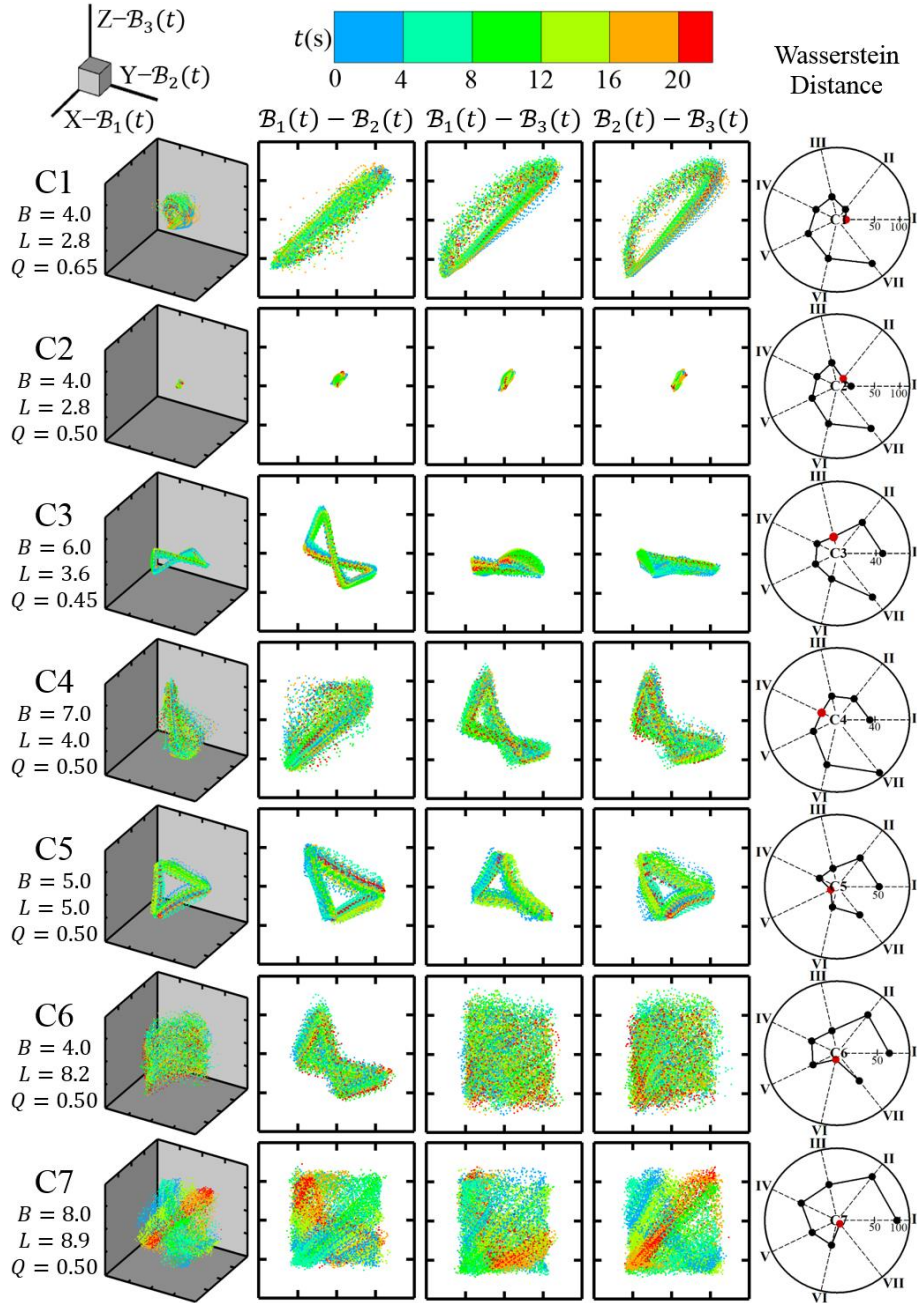


Figure 7.13 Three-dimensional phase portraits, three two-dimensional projections, flame setup parameters (unit of B and L : cm; unit of Q : slpm), and Wasserstein distances of seven experimental cases, C1–C7, which respectively correspond to Mode I – Mode VII but are different from those cases in Figure 7.9. All phase spaces, plotted by the flame brightness, have the same ranges of values in all dimensions. The Wasserstein distance (i.e., the radial distance) is the root mean square of W^{12} , W^{13} and W^{23} .

7.5.3 Dynamical Mode Recognition in Wasserstein Space

To validate the applicability of 1-Wasserstein distance in the present problem, we

selected seven experimental cases, C1–C7, as shown in Figure 7.13, which are different from those cases in Figure 7.9 but can be respectively categorized into Mode I – Mode VII. To facilitate the comparison with the mode recognition based on the shape of phase portraits, we calculated the 1-Wasserstein distance between two corresponding 2D projections of 3D portraits, namely W^{12} for the base flames, W^{13} for the leg flames, and W^{23} for the other leg flames. As a result, for any two sets of three 2D phase portraits from two experimental cases, we obtained a triplet (W^{12}, W^{13}, W^{23}) of 1-Wasserstein distances. Generally, for the two cases which are classified into the same mode, their triplet of 1-Wasserstein distances should be sufficiently small. Therefore, we can calculate the root mean square of W^{12} , W^{13} and W^{23} as a mathematically convenient indicator for the smallness of the triplet of 1-Wasserstein distances.

All the calculation results for the distance between C1–C7 and Mode I – Mode VII are given in Table 7.2. The corresponding results are diagrammatized in Figure 7.13. Although the flame setup parameters (B , L or Q) of C1-C7 are different from those of Mode I – Mode VII, they have very similar topological structures of 2D projections as shown in Figure 7.13. Specifically, the in-phase mode (C1) has all the 2D projections in the shape of a slender ellipse along the direction (1,1), the flickering death mode (C2) has all the 2D projections in the shape of a round or rectangle disk, the partial flickering death mode (C3) has two nearly horizontal rectangle-shaped and one butterfly-shaped 2D projections, the partial in-phase mode (C4) has two butterfly-shaped and a nearly elliptic 2D projections, the rotation mode (C5) has all the 2D projections in the triangle

shape, the partial decoupled mode (C6) has one butterfly-shaped and two square-shaped 2D projections, and the decoupled mode (C7) has all the 2D projections in the shape of a square. It is clearly seen in Figure 7.13 (the rightmost column) that the same categories of modes are consistent with the “closeness” of their phase portraits, measured by the Wasserstein distance.

Two major findings for mode recognition can be concluded: 1) any two cases belonging to the same mode have relatively small distances. It can be clearly seen in Table 7.2 that the diagonal triplet values are significantly smaller than the off-diagonal triplets. This naturally confirms that the recognitions of C1–C7 belong to Mode I – Mode VII, respectively. 2) any two cases belonging to different modes have relatively large distances. It can be clearly seen in Table 7.2 that the off-diagonal triplet values are relatively large. It is reasonably inferred that, if a sufficient number of cases for each mode are available, the “smallness” and “largeness” of distance can be determined by a learning process, in which the Wasserstein distance plays a crucial role in establishing a discriminator.

7.7 Concluding Remarks

The present work was motivated by two hypotheses that made by the authors about the existing experimental studies on multiple flickering buoyant diffusion flames as a nonlinear dynamical system of coupled oscillators. The first hypothesis is that the lack of adequate flame controllability is responsible for the unstable modes reported in the previous candle-flame experiments. The second hypothesis is that the different

dynamical modes can be discriminated by recognizing the different topological structures of phase portraits in phase space. We successfully verified the two hypotheses in the system of triple flickering buoyant diffusion flames in isosceles triangle arrangement and therefore proposed a new methodological framework for studying dynamical systems of multiple flickering flames.

Bunsen burners were used to produce three identical flickering buoyant diffusion flames of methane, which were precisely controlled by each individual flow rate controller. By minimizing all possible external disturbances, we identified seven distinct stable modes: the in-phase mode, the flickering death mode, the partial flickering death mode, the partial in-phase mode, the rotation mode, the partial decoupled mode, and the decoupled mode. These modes can exist within almost the entire time duration (22 seconds) of recorded flame videos and were highly repeatable for any longer duration. These modes unify all the previously discovered modes for triple candle flames in a straight-line and equal-lateral triangle arrangement.

The proposed new methodology for dynamical mode recognition follows the following procedures. First, the coupled triple-flame oscillators constitute an infinite-dimensional dynamical system, which principally should be described by partial differential equations of conservation laws for chemically reacting flows. Second, the infinite-dimensional system can be reduced to a 3D dynamical system by choosing an appropriate characteristic scalar quantity (e.g., the “flame brightness” adopted by the present study) for each flame, Third, the time evolution of the 3D dynamical system

generates phase portraits in a 3D phase space, and each phase portrait generates a distribution function. Fourth, the Wasserstein distance quantifies the “closeness” of two distribution functions as such a small Wasserstein distance indicates the similarity of two-phase portraits and the identification of the same dynamical mode. The present calculation results validate the proposed methodology, whose real potential should be shown in larger dynamical systems of flame and will be verified in future work.

Chapter 8 Future Work

For Part 1 ab initio chemical kinetics of large straight-chain alkanes, we would go further study on high-level rate coefficients calculation of typical combustion reactions of large straight-chain alkanes, such as the hydrogen abstraction reactions of $n\text{-C}_n\text{H}_{2n+2} + \text{R}$ ($n=1-16$, $\text{R}=\text{H}, \text{OH}, \text{HO}_2$), depending on the high-level thermochemical data by ONIOM method, and improved partition function methods, such as the MS-ASB and MS-nNN methods. Besides, we would extend these methods, the ONIOM method for high-level single point energy calculation, the MS-ASB method, and the MS-nNN method for high-level partition function calculation, into other large fuel molecules systems, such as methyl palmitate, methyl oleate, *iso*-cetane, etc., and more types of reactions, such as isomerization reactions, β -scission reactions, hydrogen addition reactions, etc.

For Part 2 the dynamical behaviors of coupled flickering buoyant diffusion flames of n -alkane fuels, and the coupled multiple flickering buoyant diffusion flames as a nonlinear dynamical system have gained increasing attention. Based on our new experimental method for generating reliable experimental results and the Wasserstein-space-based method for dynamical mode recognition, we will aim to establish a nonlinear dynamical model for triple (or multiple) coupled flickering diffusion flames and extend the proposed methods to larger flame systems.

Reference

- [1] W. W. Pulkrabek, *Engineering Fundamentals of the Internal Combustion Engine*, 2nd Ed. New Jersey: Prentice Hall, (2004).
- [2] C. K. Westbrook and F. L. Dryer, Chemical kinetics and modeling of combustion processes, *Proceeding of the Combustion Institute*, 18 (1981) 749-767.
- [3] W. J. Pitz, N. P. Cernansky, F. L. Dryer, F. Egolfopoulos, J. Farrell, D. G. Friend, H. Pitsch, Development of an experimental database and chemical kinetic models for surrogate gasoline fuels. *SAE Paper*, (2007) 2007-01-0175.
- [4] T. Wallington, E. Kaiser, J. Farrell, *Automotive fuels and internal combustion engines: a chemical perspective*, *Chemical Society Reviews*, 35 (4) (2006) 335-347.
- [5] J. Farrell, N. Cernansky, F. Dryer, C. K. Law, D. Friend, C. Hergart, R. McDavid, A. Patel, C. J. Mueller, H. Pitsch, Development of an experimental database and kinetic models for surrogate diesel fuels. *SAE Paper*, (2007) 2007-01-0201.
- [6] A. Violi, S. Yan, E. Eddings, A. Sarofim, S. Granata, T. Faravelli, E. Ranzi, Experimental formulation and kinetic model for JP-8 surrogate mixtures, *Combustion Science and Technology*, 174 (11-12) (2002) 399-417.
- [7] M. Colket, T. Edwards, S. Williams, N. P. Cernansky, D. L. Miller, F. Egolfopoulos, P. Lindstedt, K. Seshadri, F. L. Dryer, C. K. Law, D. Friend, D. B. Lenhert, H. Pitsch, A. Sarofim, M. Smooke, W. Tsang, Development of an experimental database and kinetic models for surrogate jet fuels. 45th AIAA Aerospace Sciences Meeting and Exhibit, (2007) AIAA-2007-0770.
- [8] S. M. Sarathy, A. Farooq, G. T. Kalghatgi, Recent progress in gasoline surrogate fuels, *Progress in Energy and Combustion Science*, 65 (2018) 67-108.
- [9] W. J. Pitz, C. J. Mueller, Recent progress in the development of diesel surrogate fuels, *Progress in Energy and Combustion Science*, 37 (3) (2011) 330-350.

- [10] R. Marchal, S. Penet, F. Solano-Serena, J. Vandecasteele, Gasoline and diesel oil biodegradation, *Oil & Gas Science and Technology*, 58 (4) (2003) 441-448.
- [11] S. Dooley, S. H. Won, M. Chaos, J. Heyne, Y. Ju, F. L. Dryer, K. Kumar, C.-J. Sung, H. Wang, M. A. Oehlschlaeger, A jet fuel surrogate formulated by real fuel properties, *Combustion and flame*, 157 (12) (2010) 2333-2339.
- [12] T. Edwards, L. Q. Maurice, Surrogate mixtures to represent complex aviation and rocket fuels, *Journal of Propulsion and Power*, 17 (2) (2001) 461-466.
- [13] M. Mehl, W. J. Pitz, C. K. Westbrook, H. J. Curran, Kinetic modeling of gasoline surrogate components and mixtures under engine conditions, *Proceedings of the Combustion Institute*, 33 (1) (2011) 193-200.
- [14] S. Jerzembeck, N. Peters, P. Pepiot-Desjardins, H. Pitsch, Laminar burning velocities at high pressure for primary reference fuels and gasoline: Experimental and numerical investigation, *Combustion and Flame*, 156 (2) (2009) 292-301.
- [15] L. Sileghem, V. Alekseev, J. Vancoillie, K. Van Geem, E. Nilsson, S. Verhelst, A. Konnov, Laminar burning velocity of gasoline and the gasoline surrogate components iso-octane, n-heptane and toluene, *Fuel*, 112 (2013) 355-365.
- [16] R. Lemaire, A. Faccinetto, E. Therssen, M. Ziskind, C. Focsa, P. Desgroux, Experimental comparison of soot formation in turbulent flames of diesel and surrogate diesel fuels, *Proceedings of the Combustion Institute*, 32 (1) (2009) 737-744.
- [17] K. Mati, A. Ristori, S. Gail, G. Pengloan, P. Dagaut, The oxidation of a diesel fuel at 1–10 atm: experimental study in a JSR and detailed chemical kinetic modeling, *Proceedings of the Combustion Institute*, 31 (2) (2007) 2939-2946.
- [18] S. Honnet, K. Seshadri, U. Niemann, N. Peters, A surrogate fuel for kerosene, *Proceedings of the Combustion Institute*, 32 (1) (2009) 485-492.
- [19] P. Dagaut, A. El Bakali, A. Ristori, The combustion of kerosene: Experimental

results and kinetic modelling using 1-to 3-component surrogate model fuels, *Fuel*, 85 (7-8) (2006) 944-956.

[20] M. Strelkova, I. Kirillov, B. Potapkin, A. Safonov, L. Sukhanov, S. Y. Umanskiy, M. Deminsky, A. Dean, B. Varatharajan, A. Tentner, Detailed and reduced mechanisms of jet a combustion at high temperatures, *Combustion science and technology*, 180 (10-11) (2008) 1788-1802.

[21] M. Mawid, B. Sekar, Development of a detailed JP-8/Jet-A chemical kinetic mechanism for high pressure conditions in gas turbine combustors. *ASME Turbo Expo 2006: Power for Land, Sea, and Air*, 42363 (2006) 369-388.

[22] K. Dahm, P. Virk, R. Bounaceur, F. Battin-Leclerc, P. Marquaire, R. Fournet, E. Daniau, M. Bouchez, Experimental and modelling investigation of the thermal decomposition of n-dodecane, *Journal of Analytical and Applied Pyrolysis*, 71 (2) (2004) 865-881.

[23] R. A. Friesner, Ab initio quantum chemistry: Methodology and applications, *Proceedings of the National Academy of Sciences*, 102 (19) (2005) 6648-6653.

[24] J. A. Miller, R. Sivaramakrishnan, Y. Tao, C. F. Goldsmith, M. P. Burke, A. W. Jasper, N. Hansen, N. J. Labbe, P. Glarborg, J. Zádor, Combustion chemistry in the twenty-first century: Developing theory-informed chemical kinetics models, *Progress in Energy and Combustion Science*, 83 (2021) 100886.

[25] S. L. Peukert, R. Sivaramakrishnan, J. V. Michael, High temperature rate constants for H/D + *n*-C₄H₁₀ and *i*-C₄H₁₀, *Proceedings of the Combustion Institute*, 35 (1) (2015) 171-179.

[26] R. Sivaramakrishnan, J. Michael, B. Ruscic, High-temperature rate constants for H/D+ C₂H₆ and C₃H₈, *International Journal of Chemical Kinetics*, 44 (3) (2012) 194-205.

- [27] R. Sivaramakrishnan, N. Srinivasan, M.-C. Su, J. Michael, High temperature rate constants for OH+ alkanes, *Proceedings of the Combustion Institute*, 32 (1) (2009) 107-114.
- [28] R. Sivaramakrishnan, J. Michael, Rate constants for OH with selected large alkanes: shock-tube measurements and an improved group scheme, *The Journal of Physical Chemistry A*, 113 (17) (2009) 5047-5060.
- [29] J. Aguilera-Iparraguirre, H. J. Curran, W. Klopper, J. M. Simmie, Accurate Benchmark Calculation of the Reaction Barrier Height for Hydrogen Abstraction by the Hydroperoxyl Radical from Methane. Implications for C_nH_{2n+2} where $n=2 \rightarrow 4$, *The Journal of Physical Chemistry A*, 112 (30) (2008) 7047-7054.
- [30] H.-H. Carstensen, A. M. Dean, O. Deutschmann, Rate constants for the H abstraction from alkanes (R-H) by R'O₂ radicals: A systematic study on the impact of R and R', *Proceedings of the Combustion Institute*, 31 (1) (2007) 149-157.
- [31] E. Papajak, D. G. Truhlar, What are the most efficient basis set strategies for correlated wave function calculations of reaction energies and barrier heights?, *The Journal of Chemical Physics*, 137 (6) (2012) 064110.
- [32] J. Zádor, C. A. Taatjes, R. X. Fernandes, Kinetics of elementary reactions in low-temperature autoignition chemistry, *Progress in Energy and Combustion Science*, 37 (4) (2011) 371-421.
- [33] C. F. Goldsmith, G. R. Magoon, W. H. Green, Database of small molecule thermochemistry for combustion, *The Journal of Physical Chemistry A*, 116 (36) (2012) 9033-9057.
- [34] S. J. Klippenstein, V. S. Pande, D. G. Truhlar, Chemical kinetics and mechanisms of complex systems: a perspective on recent theoretical advances, *Journal of the American Chemical Society*, 136 (2) (2014) 528-546.

- [35] L. Zhang, P. Zhang, Towards high-level theoretical studies of large biodiesel molecules: an ONIOM [QCISD (T)/CBS: DFT] study of hydrogen abstraction reactions of $C_nH_{2n+1}COOC_mH_{2m+1} + H$, *Physical Chemistry Chemical Physics*, 17 (1) (2015) 200-208.
- [36] K. S. Pitzer, W. D. Gwinn, Energy levels and thermodynamic functions for molecules with internal rotation I. Rigid frame with attached tops, *The Journal of Chemical Physics*, 10 (7) (1942) 428-440.
- [37] E. Dzib, G. Merino, The hindered rotor theory: A review, *Wiley Interdisciplinary Reviews: Computational Molecular Science*, (2021) e1583.
- [38] J. Zheng, T. Yu, E. Papajak, I. Alecu, S. L. Mielke, D. G. Truhlar, Practical methods for including torsional anharmonicity in thermochemical calculations on complex molecules: The internal-coordinate multi-structural approximation, *Physical Chemistry Chemical Physics*, 13 (23) (2011) 10885-10907.
- [39] P. Seal, G. Oyedepo, D. G. Truhlar, Kinetics of the hydrogen atom abstraction reactions from 1-butanol by hydroxyl radical: theory matches experiment and more, *The Journal of Physical Chemistry A*, 117 (2) (2013) 275-282.
- [40] I. Alecu, D. G. Truhlar, Computational study of the reactions of methanol with the hydroperoxyl and methyl radicals. 2. Accurate thermal rate constants, *The Journal of Physical Chemistry A*, 115 (51) (2011) 14599-14611.
- [41] J. P. Lowe, K. Peterson, *Quantum chemistry*, Elsevier, (2011).
- [42] E. De Vries, J. Jonker, Non-relativistic approximations of the Dirac Hamiltonian, *Nuclear Physics B*, 6 (3) (1968) 213-225.
- [43] M. Born, R. Oppenheimer, Zur quantentheorie der molekeln, *Annalen der physik*, 389 (20) (1927) 457-484.
- [44] H.-M. McConnell, Molecular orbital approximation to electron coupled interaction

- between nuclear spins, *The Journal of Chemical Physics*, 24 (2) (1956) 460-467.
- [45] A. D. Becke, Basis-set-free density-functional quantum chemistry, *International Journal of Quantum Chemistry*, 36 (S23) (1989) 599-609.
- [46] S. Blinder, Basic concepts of self-consistent-field theory, *American Journal of Physics*, 33 (6) (1965) 431-443.
- [47] P. Stephens, F. Devlin, C. Chabalowski, M. J. Frisch, Ab initio calculation of vibrational absorption and circular dichroism spectra using density functional force fields, *The Journal of Physical Chemistry*, 98 (45) (1994) 11623-11627.
- [48] K. Kim, K. Jordan, Comparison of density functional and MP2 calculations on the water monomer and dimer, *The Journal of Physical Chemistry*, 98 (40) (1994) 10089-10094.
- [49] Y. Zhao, D. G. Truhlar, The M06 suite of density functionals for main group thermochemistry, thermochemical kinetics, noncovalent interactions, excited states, and transition elements: two new functionals and systematic testing of four M06-class functionals and 12 other functionals, *Theoretical Chemistry Accounts*, 120 (1-3) (2008) 215-241.
- [50] Y. Zhao, D. G. Truhlar, Density functional for spectroscopy: no long-range self-interaction error, good performance for Rydberg and charge-transfer states, and better performance on average than B3LYP for ground states, *The Journal of Physical Chemistry A*, 110 (49) (2006) 13126-13130.
- [51] S. F. Boys, Electronic wave functions-I. A general method of calculation for the stationary states of any molecular system, *Proceedings of the Royal Society of London. Series A. Mathematical and Physical Sciences*, 200 (1063) (1950) 542-554.
- [52] D. W. Sciama, The physical significance of the vacuum state of a quantum field, (1991).

- [53] R. S. Grev, C. L. Janssen, H. F. Schaefer III, Concerning zero-point vibrational energy corrections to electronic energies, *The Journal of Chemical Physics*, 95 (7) (1991) 5128-5132.
- [54] P. Dagaut, M. Cathonnet, The ignition, oxidation, and combustion of kerosene: A review of experimental and kinetic modeling, *Progress in Energy and Combustion Science*, 32 (1) (2006) 48-92.
- [55] C. K. Westbrook, F. L. Dryer, Chemical kinetic modeling of hydrocarbon combustion, *Progress in Energy and Combustion Science*, 10 (1) (1984) 1-57.
- [56] J. M. Simmie, Detailed chemical kinetic models for the combustion of hydrocarbon fuels, *Progress in Energy and Combustion Science*, 29 (6) (2003) 599-634.
- [57] E. Ranzi, A. Frassoldati, R. Grana, A. Cuoci, T. Faravelli, A. P. Kelley, C. K. Law, Hierarchical and comparative kinetic modeling of laminar flame speeds of hydrocarbon and oxygenated fuels, *Progress in Energy and Combustion Science*, 38 (4) (2012) 468-501.
- [58] H. J. Curran, P. Gaffuri, W. J. Pitz, C. K. Westbrook, A comprehensive modeling study of n-heptane oxidation, *Combustion and Flame*, 114 (1-2) (1998) 149-177.
- [59] H. J. Curran, P. Gaffuri, W. J. Pitz, C. K. Westbrook, A comprehensive modeling study of iso-octane oxidation, *Combustion and Flame*, 129 (3) (2002) 253-280.
- [60] C. K. Westbrook, W. J. Pitz, O. Herbinet, H. J. Curran, E. J. Silke, A comprehensive detailed chemical kinetic reaction mechanism for combustion of n-alkane hydrocarbons from n-octane to n-hexadecane, *Combustion and Flame*, 156 (1) (2009) 181-199.
- [61] E. R. Ritter, J. W. Bozzelli, THERM: Thermodynamic property estimation for gas phase radicals and molecules, *International Journal of Chemical Kinetics*, 23 (9) (1991) 767-778.
- [62] T. H. Lay, J. W. Bozzelli, A. M. Dean, E. R. Ritter, Hydrogen atom bond increments

for calculation of thermodynamic properties of hydrocarbon radical species, *The Journal of Physical Chemistry*, 99 (39) (1995) 14514-14527.

[63] S. W. Benson, *Thermochemical kinetics*, Wiley, (1976).

[64] A. M. El-Nahas, M. V. Navarro, J. M. Simmie, J. W. Bozzelli, H. J. Curran, S. Dooley, W. Metcalfe, Enthalpies of formation, bond dissociation energies and reaction paths for the decomposition of model biofuels: ethyl propanoate and methyl butanoate, *The Journal of Physical Chemistry A*, 111 (19) (2007) 3727-3739.

[65] A. Osmont, L. Catoire, P. Dagaut, Thermodynamic data for the modeling of the thermal decomposition of biodiesel. 1. Saturated and monounsaturated FAMES, *The Journal of Physical Chemistry A*, 114 (11) (2010) 3788-3795.

[66] T. Vreven, K. S. Byun, I. Komáromi, S. Dapprich S J. A. Montgomery Jr, K. Morokuma, M. J. Frisch, Combining quantum mechanics methods with molecular mechanics methods in ONIOM, *Journal of Chemical Theory and Computation*, 2 (3) (2006) 815-826.

[67] L. Zhang, Q. Meng, Y. Chi, P. Zhang, Toward High-Level Theoretical Studies of Large Biodiesel Molecules: An ONIOM [QCISD(T)/CBS:DFT] Study of the Reactions between Unsaturated Methyl Esters ($C_nH_{2n-1}COOCH_3$) and Hydrogen Radical, *The Journal of Physical Chemistry A*, 122 (21) (2018) 4882-4893.

[68] N. Cohen, The use of transition-state theory to extrapolate rate coefficients for reactions of H atoms with alkanes, *International Journal of Chemical Kinetics*, 23 (8) (1991) 683-700.

[69] N. Cohen, Are reaction rate coefficients additive? Revised transition state theory calculations for OH+ alkane reactions, *International Journal of Chemical Kinetics*, 23 (5) (1991) 397-417.

[70] J. Espinosa-Garcia, New analytical potential energy surface for the $CH_4 + H$

hydrogen abstraction reaction: thermal rate constants and kinetic isotope effects, *The Journal of chemical physics*, 116 (24) (2002) 10664-10673.

[71] A. D. Beck, Density-functional thermochemistry. III. The role of exact exchange, *Journal of Chemical Physics* 98 (7) (1993) 5648-5652.

[72] Y. Zhao, D. G. Truhlar, A new local density functional for main-group thermochemistry, transition metal bonding, thermochemical kinetics, and noncovalent interactions, *The Journal of Chemical Physics*, 125 (19) (2006) 194101.

[73] T. H. Dunning Jr, Gaussian basis sets for use in correlated molecular calculations. I. The atoms boron through neon and hydrogen, *The Journal of Chemical Physics*, 90 (2) (1989) 1007-1023.

[74] R. A. Kendall, T. H. Dunning Jr, R. J. Harrison, Electron affinities of the first-row atoms revisited. Systematic basis sets and wave functions, *The Journal of Chemical Physics*, 96 (9) (1992) 6796-6806.

[75] J. M. Martin, O. Uzan, Basis set convergence in second-row compounds. The importance of core polarization functions, *Chemical Physics Letters*, 282 (1) (1998) 16-24.

[76] P. Zhang, S. J. Klippenstein, C. K. Law, Ab initio kinetics for the decomposition of hydroxybutyl and butoxy radicals of n-butanol, *The Journal of Physical Chemistry A*, 117 (9) (2013) 1890-1906.

[77] Q. Meng, Y. Chi, L. Zhang, P. Zhang, L. Sheng, Towards high-level theoretical studies of large biodiesel molecules: an ONIOM/RRKM/Master-equation approach to the isomerization and dissociation kinetics of methyl decanoate radicals, *Physical Chemistry Chemical Physics*, 21 (9) (2019) 5232-5242.

[78] M. J. T. Frisch, G. W.; Schlegel, H. B.; Scuseria, G. E.; Robb, M. A.; Cheeseman, J. R.; Scalmani, G.; Barone, V.; Mennucci, B.; Petersson, G. A.; Nakatsuji, H.; Caricato,

M.; Li, X.; Hratchian, H. P.; Izmaylov, A. F.; Bloino, J.; Zheng, G.; Sonnenberg, J. L.; Hada, M.; Ehara, M.; Toyota, K.; Fukuda, R.; Hasegawa, J.; Ishida, M.; Nakajima, T.; Honda, Y.; Kitao, O.; Nakai, H.; Vreven, T.; Montgomery, J. A., Jr.; Peralta, J. E.; Ogliaro, F.; Bearpark, M.; Heyd, J. J.; Brothers, E.; Kudin, K. N.; Staroverov, V. N.; Kobayashi, R.; Normand, J.; Raghavachari, K.; Rendell, A.; Burant, J. C.; Iyengar, S. S.; Tomasi, J.; Cossi, M.; Rega, N.; Millam, J. M.; Klene, M.; Knox, J. E.; Cross, J. B.; Bakken, V.; Adamo, C.; Jaramillo, J.; Gomperts, R.; Stratmann, R. E.; Yazyev, O.; Austin, A. J.; Cammi, R.; Pomelli, C.; Ochterski, J. W.; Martin, R. L.; Morokuma, K.; Zakrzewski, V. G.; Voth, G. A.; Salvador, P.; Dannenberg, J. J.; Dapprich, S.; Daniels, A. D.; Farkas, Ö.; Foresman, J. B.; Ortiz, J. V.; Cioslowski, J.; Fox, D. J., Gaussian 09, Revision E.01, Gaussian, Inc., Wallingford, CT, (2009).

[79] F. Battin-Leclerc, E. Blurock, R. Bounaceur, R. Fournet, P.-A. Glaude, O. Herbinet, B. Sirjean, V. Warth, Towards cleaner combustion engines through groundbreaking detailed chemical kinetic models, *Chemical Society Reviews*, 40 (9) (2011) 4762-4782.

[80] M. Nehse, J. Warnat, C. Chevalier, Kinetic modeling of the oxidation of large aliphatic hydrocarbons, *Proceeding of the Combustion Institute*, 26 (1996) 773-780.

[81] M. V. Petrova, F. A. Williams, A small detailed chemical-kinetic mechanism for hydrocarbon combustion, *Combustion and Flame*, 144 (3) (2006) 526-544.

[82] J. Warnatz, Resolution of gas phase and surface combustion chemistry into elementary reactions, *Proceeding of the Combustion Institute*, 24 (1992) 553-579.

[83] N. Cohen, The use of transition-state theory to extrapolate rate coefficients for reactions of OH with alkanes, *International Journal of Chemical Kinetics*, 14 (12) (1982) 1339-1362.

[84] M. Evans, M. Polanyi, Inertia and driving force of chemical reactions, *Transactions of the Faraday Society*, 34 (1938) 11-24.

- [85] Y. Chi, X. You, Kinetics of Hydrogen Abstraction Reactions of Methyl Palmitate and Octadecane by Hydrogen Atoms, *The Journal of Physical Chemistry A*, 123 (14) (2019) 3058-3067.
- [86] I. Rossi, D. G. Truhlar, Improved general scaling factors and systematic tests of the SAC method for estimating correlation energies of molecules, *Chemical Physics Letters*, 234 (1-3) (1995) 64-70.
- [87] A. Fernández-Ramos, J. A. Miller, S. J. Klippenstein, D. G. Truhlar, Modeling the kinetics of bimolecular reactions, *Chemical reviews*, 106 (11) (2006) 4518-4584.
- [88] D. G. Truhlar, B. C. Garrett, S. J. Klippenstein, Current status of transition-state theory, *The Journal of physical chemistry*, 100 (31) (1996) 12771-12800.
- [89] D. G. Truhlar, W. L. Hase, J. T. Hynes, Current status of transition-state theory, *The Journal of Physical Chemistry*, 87 (15) (1983) 2664-2682.
- [90] W. Li, S. Li, Y. Jiang, Generalized energy-based fragmentation approach for computing the ground-state energies and properties of large molecules, *The Journal of Physical Chemistry A*, 111 (11) (2007) 2193-2199.
- [91] J. Wu, H. Ning, L. Ma, P. Zhang, W. Ren, Cascaded group-additivity ONIOM: A new method to approach CCSD(T)/CBS energies of large aliphatic hydrocarbons, *Combustion and Flame*, 201 (2009) 31-43.
- [92] K. S. Pitzer, Energy levels and thermodynamic functions for molecules with internal rotation: II. Unsymmetrical tops attached to a rigid frame, *The Journal of Chemical Physics*, 14 (4) (1946) 239-243.
- [93] J. E. Kilpatrick, K. S. Pitzer, Energy levels and thermodynamic functions for molecules with internal rotation. III. Compound rotation, *The Journal of Chemical Physics*, 17 (11) (1949) 1064-1075.
- [94] D. G. Truhlar, A simple approximation for the vibrational partition function of a

- hindered internal rotation, *Journal of computational chemistry*, 12 (2) (1991) 266-270.
- [95] P. Y. Ayala, H. B. Schlegel, Identification and treatment of internal rotation in normal mode vibrational analysis, *The Journal of Chemical Physics*, 108 (6) (1998) 2314-2325.
- [96] B. A. Ellingson, V. A. Lynch, S. L. Mielke, D. G. Truhlar, Statistical thermodynamics of bond torsional modes: Tests of separable, almost-separable, and improved Pitzer–Gwinn approximations, *The Journal of chemical physics*, 125 (8) (2006) 084305.
- [97] J. Pfaendtner, X. Yu, L. J. Broadbelt, The 1-D hindered rotor approximation, *Theoretical Chemistry Accounts*, 118 (5) (2007) 881-898.
- [98] T. H. Lay, L. N. Krasnoperov, C. A. Venanzi, J. W. Bozzelli, N. V. Shokhirev, Ab initio study of α -chlorinated ethyl hydroperoxides $\text{CH}_3\text{CH}_2\text{OOH}$, $\text{CH}_3\text{CHClOOH}$, and $\text{CH}_3\text{CCl}_2\text{OOH}$: conformational analysis, internal rotation barriers, vibrational frequencies, and thermodynamic properties, *The Journal of Physical Chemistry*, 100 (20) (1996) 8240-8249.
- [99] D. Gruzman, A. Karton, J. M. Martin, Performance of Ab Initio and Density Functional Methods for Conformational Equilibria of $\text{C}_n\text{H}_{2n+2}$ Alkane Isomers ($n= 4-8$), *The Journal of Physical Chemistry A*, 113 (43) (2009) 11974-11983.
- [100] S. Sharma, S. Raman, W. H. Green, Intramolecular hydrogen migration in alkylperoxy and hydroperoxyalkylperoxy radicals: accurate treatment of hindered rotors, *The Journal of Physical Chemistry A*, 114 (18) (2010) 5689-5701.
- [101] Q. Meng, L. Zhang, Q. Chen, Y. Chi, P. Zhang, Influence of torsional anharmonicity on the reactions of methyl butanoate with hydroperoxyl radical, *The Journal of Physical Chemistry A*, 124 (42) (2020) 8643-8652.
- [102] V. Van Speybroeck, D. Van Neck, M. Waroquier, Ab initio study of radical

reactions: role of coupled internal rotations on the reaction kinetics (III), *The Journal of Physical Chemistry A*, 106 (38) (2002) 8945-8950.

[103] V. Van Speybroeck, P. Vansteenkiste, D. Van Neck, M. Waroquier, Why does the uncoupled hindered rotor model work well for the thermodynamics of n-alkanes?, *Chemical Physics Letters*, 402 (4-6) (2005) 479-484.

[104] J. Zheng, D. G. Truhlar, Quantum thermochemistry: Multistructural method with torsional anharmonicity based on a coupled torsional potential, *Journal of Chemical Theory and Computation*, 9 (3) (2013) 1356-1367.

[105] J. Zheng, R. Meana-Pañeda, D. G. Truhlar, MSTor version 2013: A new version of the computer code for the multi-structural torsional anharmonicity, now with a coupled torsional potential, *Computer Physics Communications*, 184 (8) (2013) 2032-2033.

[106] J. Zheng, S. L. Mielke, K. L. Clarkson, D. G. Truhlar, MSTor: A program for calculating partition functions, free energies, enthalpies, entropies, and heat capacities of complex molecules including torsional anharmonicity, *Computer Physics Communications*, 183 (8) (2012) 1803-1812.

[107] P. Seal, E. Papajak, D. G. Truhlar, Kinetics of the hydrogen abstraction from carbon-3 of 1-butanol by hydroperoxyl radical: Multi-structural variational transition-state calculations of a reaction with 262 conformations of the transition state, *The journal of physical chemistry letters*, 3 (2) (2012) 264-271.

[108] F. Aurenhammer, Voronoi diagrams—a survey of a fundamental geometric data structure, *ACM Computing Surveys (CSUR)*, 23 (3) (1991) 345-405.

[109] J. Zheng, G. A. Oyedepo, D. G. Truhlar, Kinetics of the hydrogen abstraction reaction from 2-butanol by OH radical, *The Journal of Physical Chemistry A*, 119 (50) (2015) 12182-12192.

- [110] A. W. Date, *Analytic Combustion*, Springer, (2011).
- [111] J. L. Bao, L. Xing, D. G. Truhlar, Dual-level method for estimating multistructural partition functions with torsional anharmonicity, *Journal of Chemical Theory and Computation*, 13 (6) (2017) 2511-2522.
- [112] J. Wu, H. Ning, X. Xu, W. Ren, Accurate entropy calculation for large flexible hydrocarbons using a multi-structural 2-dimensional torsion method, *Physical Chemistry Chemical Physics*, 21 (19) (2019) 10003-10010.
- [113] J. E. Kilpatrick, K. S. Pitzer, Energy levels and thermodynamic functions for molecules with internal rotation. III. Compound rotation, *J. Chem. Phys.*, 17 (11) (1949) 1064-1075.
- [114] P. R. Halmos, *A Hilbert space problem book*, Springer Science & Business Media, (2012).
- [115] N. Young, *An introduction to Hilbert space*, Cambridge university press, (1988).
- [116] P. E. Black, *Dictionary of algorithms and data structures*, (1998).
- [117] E. F. Krause, *Taxicab geometry: An adventure in non-Euclidean geometry*, Courier Corporation, (1986).
- [118] H. Minkowski, *Geometrie der zahlen*, Teubner, (1910).
- [119] S. Rolewicz, *Functional analysis and control theory: linear systems*, Springer Science & Business Media, (2013).
- [120] J. Väisälä, *Hyperbolic and uniform domains in Banach spaces*, Department of Mathematics, University of Helsinki, (2004).
- [121] C. He, Y. Chi, P. Zhang, Approximate reconstruction of torsional potential energy surface based on voronoi tessellation, *Proceedings of the Combustion Institute*, 38 (1) (2021) 757-766.
- [122] D. W. Scott, *Chemical Thermodynamic Properties of Hydrocarbons and Related*

Substances: Properties of the Alkane Hydrocarbons, C1 through C10, in the Ideal Gas State From 0 to 1500 K, US Department of the Interior, Bureau of Mines, (1974).

[123] C. Jia, C. Wang, L. Zhang, X. Peng, R. Zeng, X. You, Partition function of improved Tietz oscillators, *Chemical Physics Letters*, 676 (2017) 150-153.

[124] A. Beste, One-dimensional anharmonic oscillator: Quantum versus classical vibrational partition functions, *Chemical Physics Letters*, 493 (1-3) (2010) 200-205.

[125] M. Strelakov, An accurate closed-form expression for the partition function of Morse oscillators, *Chemical physics letters*, 439 (1-3) (2007) 209-212.

[126] J. Zheng, R. Meana-Pañeda, D. G. Truhlar, Prediction of experimentally unavailable product branching ratios for biofuel combustion: The role of anharmonicity in the reaction of isobutanol with OH, *Journal of the American Chemical Society*, 136 (13) (2014) 5150-5160.

[127] C. Y. Lin, E. I. Izgorodina, M. L. Coote, How accurate are approximate methods for evaluating partition functions for hindered internal rotations?, *The Journal of Physical Chemistry A*, 112 (9) (2008) 1956-1964.

[128] S. L. Mielke, D. G. Truhlar, Improved methods for Feynman path integral calculations and their application to calculate converged vibrational-rotational partition functions, free energies, enthalpies, entropies, and heat capacities for methane, *The Journal of Chemical Physics*, 142 (4) (2015) 044105.

[129] A. W. Jasper, Z. B. Gruey, L. B. Harding, Y. Georgievskii, S. J. Klippenstein, A. F. Wagner, Anharmonic rovibrational partition functions for fluxional species at high temperatures via Monte Carlo phase space integrals, *The Journal of Physical Chemistry A*, 122 (6) (2018) 1727-1740.

[130] L. Mu, Polygon characterization with the multiplicatively weighted Voronoi diagram, *The Professional Geographer*, 56 (2) (2004) 223-239.

- [131] J. Koput, S. Carter, N. C. Handy, Potential Energy Surface and Vibrational–Rotational Energy Levels of Hydrogen Peroxide, *The Journal of Physical Chemistry A*, 102 (31) (1998) 6325-6330.
- [132] S. Burke, T. Schumann, Diffusion flames, *Industrial & Engineering Chemistry*, 20 (10) (1928) 998-1004.
- [133] A. Linán, M. Vera, A. L. Sánchez, Ignition, liftoff, and extinction of gaseous diffusion flames, *Annual Review of Fluid Mechanics*, 47 (2015) 293-314.
- [134] D. S. Chamberlin, A. Rose, The flicker of luminous flames, *Proceeding of the Combustion Institute*, 1-2 (1948) 27-32.
- [135] J. Barr, Diffusion flames, *Proceeding of the Combustion Institute*, 4 (1) (1953) 765-771.
- [136] S. R. Tieszen, On the fluid mechanics of fires, *Annual Review of Fluid Mechanics*, 33 (1) (2001) 67-92.
- [137] W. Malalasekera, H. K. Versteeg, K. Gilchrist, A review of research and an experimental study on the pulsation of buoyant diffusion flames and pool fires, *Fire and Materials*, 20 (6) (1996) 261-271.
- [138] A. Grant, J. Jones, Low-frequency diffusion flame oscillations, *Combustion and Flame*, 25 (1975) 153-160.
- [139] L. D. Chen, J. Seaba, W. Roquemore, L. Goss, Buoyant diffusion flames, *Proceeding of the Combustion Institute*, 22(1) (1989) 677-684.
- [140] A. Ballantyne, K. Bray, Investigations into the structure of jet diffusion flames using time-resolved optical measuring techniques, *Proceeding of the Combustion Institute*, 16 (1) (1977) 777-787.
- [141] J. Buckmaster, N. Peters, The infinite candle and its stability—a paradigm for flickering diffusion flames, *Proceeding of the Combustion Institute*, 21 (1) (1988) 1829-

1836.

- [142] D. Moreno-Boza, W. Coenen, A. Sevilla, J. Carpio, A. Sánchez, A. Liñán, Diffusion-flame flickering as a hydrodynamic global mode, *Journal of Fluid Mechanics*, 798 (2016) 997-1014.
- [143] G. M. Byram, R. M. Nelson, The modeling of pulsating fires, *Fire Technology*, 6 (2) (1970) 102-110.
- [144] R. PORTSCHT, Studies on characteristic fluctuations of the flame radiation emitted by fires, *Combustion Science and Technology*, 10 (1-2) (1975) 73-84.
- [145] E. Zukoski, B. Cetegen, T. Kubota, Visible structure of buoyant diffusion flames, *Proceeding of the Combustion Institute*, 20 (1) (1985) 361-366.
- [146] A. Hamins, J. Yang, T. Kashiwagi, An experimental investigation of the pulsation frequency of flames, *Proceeding of the Combustion Institute*, 24 (1) (1992) 1695-1702.
- [147] B. M. Cetegen, T. A. Ahmed, Experiments on the periodic instability of buoyant plumes and pool fires, *Combustion and Flame*, 93 (1-2) (1993) 157-184.
- [148] X. Xia, P. Zhang, A vortex-dynamical scaling theory for flickering buoyant diffusion flames, *Journal of Fluid Mechanics*, 855 (2018) 1156-1169.
- [149] H. Kitahata, J. Taguchi, M. Nagayama, T. Sakurai, Y. Ikura, A. Osa, Y. Sumino, M. Tanaka, E. Yokoyama, H. Miike, Oscillation and synchronization in the combustion of candles, *The Journal of Physical Chemistry A*, 113 (29) (2009) 8164-8168.
- [150] D. M. Forrester, Arrays of coupled chemical oscillators, *Scientific reports*, 5 (1) (2015) 1-7.
- [151] K. Manoj, S. A. Pawar, R. Sujith, Experimental evidence of amplitude death and phase-flip bifurcation between in-phase and anti-phase synchronization, *Scientific reports*, 8 (1) (2018) 1-7.
- [152] S. Dange, S. A. Pawar, K. Manoj, R. Sujith, Role of buoyancy-driven vortices in

inducing different modes of coupled behaviour in candle-flame oscillators, *AIP Advances*, 9 (1) (2019) 015119.

[153] T. Yang, X. Xia, P. Zhang, Vortex-dynamical interpretation of anti-phase and in-phase flickering of dual buoyant diffusion flames, *Physical Review Fluids*, 4 (5) (2019) 053202.

[154] N. Fujisawa, K. Imaizumi, T. Yamagata, Synchronization of dual diffusion flame in co-flow, *Experimental Thermal and Fluid Science*, 110 (2020) 109924.

[155] A. Bunkwang, T. Matsuoka, Y. Nakamura, Similarity of dynamic behavior of buoyant single and twin jet-flame (s), *Journal of Thermal Science and Technology*, 15 (3) (2020) 1-14.

[156] A. Bunkwang, T. Matsuoka, Y. Nakamura, Mode transition of interacting buoyant non-premixed flames, *Journal of Thermal Science and Technology*, 15 (1) (2020) 1-11.

[157] T. Tokami, M. Toyoda, T. Miyano, I. T. Tokuda, H. Gotoda, Effect of gravity on synchronization of two coupled buoyancy-induced turbulent flames, *Physical Review E*, 104 (2) (2021) 024218.

[158] K. Okamoto, A. Kijima, Y. Umeno, H. Shima, Synchronization in flickering of three-coupled candle flames, *Scientific Reports*, 6 (1) (2016) 1-10.

[159] D. M. Abrams, S. H. Strogatz, Chimera states for coupled oscillators, *Physical Review Letters*, 93 (17) (2004) 174102.

[160] Y. Kuramoto, D. Battogtokh, Coexistence of coherence and incoherence in nonlocally coupled phase oscillators, *arXiv preprint cond-mat/0210694*, (2002).

[161] K. Manoj, S. A. Pawar, S. Dange, S. Mondal, R. Sujith, E. Surovyatkina, J. Kurths, Synchronization route to weak chimera in four candle-flame oscillators, *Physical Review E*, 100 (6) (2019) 062204.

[162] K. Manoj, S. A. Pawar, R. Sujith, Experimental investigation on the susceptibility

of minimal networks to a change in topology and number of oscillators, *Physical Review E*, 103 (2) (2021) 022207.

[163] T. Chen, X. Guo, J. Jia, J. Xiao, Frequency and phase characteristics of candle flame oscillation, *Scientific Reports*, 9 (1) (2019) 1-13.

[164] A. Gergely, B. Sándor, C. Paizs, R. Tötös, Z. Néda, Flickering candle flames and their collective behavior, *Scientific Reports*, 10 (1) (2020) 1-13.

[165] M. Aravind, I. Tiwari, V. Vasani, J.-M. Cruz, D. A. Vasquez, P. Parmananda, Ethanol lamp: a simple, tunable flame oscillator and its coupled dynamics, *The European Physical Journal Special Topics*, (2021) 1-6.

[166] Y. A. Kuznetsov, I. A. Kuznetsov, Y. Kuznetsov, *Elements of applied bifurcation theory*, Springer, (1998).

[167] J. D. Crawford, Introduction to bifurcation theory, *Reviews of Modern Physics*, 63 (4) (1991) 991.

[168] C. Villani, *Optimal transport: old and new*, Springer, (2009).

[169] N. Lei, D. An, Y. Guo, K. Su, S. Liu, Z. Luo, S.-T. Yau, X. Gu, A geometric understanding of deep learning, *Engineering*, 6 (3) (2020) 361-374.

[170] X. Zhu, R. Li, D. Li, P. Zhang, R. Qian, Experimental study and RANS calculation on velocity and temperature of a kerosene-fueled swirl laboratory combustor with and without centerbody air injection, *International Journal of Heat and Mass Transfer*, 89 (2015) 964-976.

[171] X. Zhu, X. Xia, P. Zhang, Near-field flow stability of buoyant methane/air inverse diffusion flames, *Combustion and Flame*, 191 (2018) 66-75.

[172] X. Zhu, X. Xia, P. Zhang, Stability of buoyant inverse diffusion methane flames with confinement effects, *Combustion Science and Technology*, 20 (9) (2020) 1650-1667.

- [173] V. R. Katta, W. M. Roquemore, A. Menon, S.-Y. Lee, R. J. Santoro, T. A. Litzinger, Impact of soot on flame flicker, *Proceedings of the Combustion Institute*, 32 (1) (2009) 1343-1350.
- [174] D. Moreno-Boza, W. Coenen, J. Carpio, A. L. Sánchez, F. A. Williams, On the critical conditions for pool-fire puffing, *Combustion and Flame*, 192 (2018) 426-438.
- [175] N. Fujisawa, Y. Matsumoto, T. Yamagata, Influence of co-flow on flickering diffusion flame, *Flow, Turbulence and Combustion*, 97 (3) (2016) 931-950.
- [176] H. Zhang, X. Xia, Y. Gao, Instability transition of a jet diffusion flame in quiescent environment, *Proceedings of the Combustion Institute*, 38 (3) (2021) 4971-4978.
- [177] T. Yang, Y. Chi, P. Zhang,. Vortex Interaction in Triple Flickering Buoyant Diffusion Flames. Accepted by The 39th International Symposium on Combustion, arXiv:2201.01585, (2022).
- [178] H. Sato, K. Amagai, M. Arai, Diffusion flames and their flickering motions related with Froude numbers under various gravity levels, *Combustion and Flame*, 123 (1-2) (2000) 107-118.
- [179] A. Gergely, C. Paizs, R. Tötös, Z. Néda, Oscillations and collective behavior in convective flows, *Physics of Fluids*, 33 (12) (2021) 124104.
- [180] J. A. Carrillo, G. Toscani, Wasserstein metric and large-time asymptotics of nonlinear diffusion equations, *New Trends in Mathematical Physics: In Honour of the Salvatore Rionero 70th Birthday*, World Scientific, (2004).
- [181] L. V. Kantorovich, Mathematical methods of organizing and planning production, *Management Science*, 6 (4) (1960) 366-422.
- [182] L. V. Kantorovich, On the translocation of masses, *Journal of Mathematical Sciences*, 133 (4) (2006) 1381-1382.

[183] Wasserstein distance code for Matlab, available at
<<https://github.com/nklb/wasserstein-distance>>.